A Unified 2D Solver for Modeling Carrier and Defect Dynamics in Electronic and Photovoltaic Devices

by

Abdul Rawoof Shaik

A Dissertation Presented in Partial Fulfillment
of the Requirements for the Degree
Doctor of Philosophy

Approved October 2019 by the
Graduate Supervisory Committee:

Dragica Vasileska, Chair
Christian Ringhofer
Igor Sankin
Daniel Brinkman
Stephen Goodnick
Mariana Bertoni

ARIZONA STATE UNIVERSITY

December 2019

ABSTRACT

Semiconductor devices often face reliability issues due to their operational conditions causing performance degradation over time. One of the root causes of such degradation is due to point defect dynamics and time dependent changes in their chemical nature. Previously developed Unified Solver was successful in explaining the copper (Cu) metastability issues in cadmium telluride (CdTe) solar cells. The point defect formalism employed there could not be extended to chlorine or arsenic due to numerical instabilities with the dopant chemical reactions. To overcome these shortcomings, an advanced version of the Unified Solver called PVRD-FASP tool was developed. This dissertation presents details about PVRD-FASP tool, the theoretical framework for point defect chemical formalism, challenges faced with numerical algorithms, improvements for the user interface, application and/or validation of the tool with carefully chosen simulations, and open source availability of the tool for the scientific community.

Treating point defects and charge carriers on an equal footing in the new formalism allows to incorporate chemical reaction rate term as generation-recombination(G-R) term in continuity equation. Due to the stiff differential equations involved, a reaction solver based on forward Euler method with Newton step is proposed in this work. The Jacobian required for Newton step is analytically calculated in an elegant way improving speed, stability and accuracy of the tool. A novel non-linear correction scheme is proposed and implemented to resolve charge conservation issue.

The proposed formalism is validated in 0-D with time evolution of free carriers simulation and with doping limits of Cu in CdTe simulation. Excellent agreement of light JV curves calculated with PVRD-FASP and Silvaco Atlas tool for a 1-D CdTe solar cell validates reaction formalism and tool accuracy. A closer match with the Cu

SIMS profiles of Cu activated CdTe samples at four different anneal recipes to the simulation results show practical applicability. A 1D simulation of full stack CdTe device with Cu activation at 350°C 3min anneal recipe and light JV curve simulation demonstrates the tool capabilities in performing process and device simulations. CdTe device simulation for understanding differences between traps and recombination centers in grain boundaries demonstrate 2D capabilities.

DEDICATION

Dedicated to my parents,

Shri Late Abdul Khadar Basha Shaik,

Smt Nagoor Bee Shaik.

ACKNOWLEDGMENTS

Firstly, I would like to thank Dr. Dragica Vasileska, my mentor and advisor for guiding and supporting me through out my PhD studies here at ASU. She supported me both intellectually and financially during the time of need and always encouraged me to showcase our work in multiple platforms for building collaborative work. I would like to thank Dr. Christian Ringhofer who enlightened me about the numerical techniques and taught me the mathematical thought process for solving the practical issues. I thank Dr. Igor Sankin for guiding and encouraging me to focus on practical issues rather than stuck with the software coding issues. I would like to thank both Dr. Igor Sankin and Dr. Dmitry Krasikov for patiently explaining me about the point defect chemistry and the needs of the industry. Special thanks to Dr. Dmitry Krasikov for the brainstorming email chains regarding the point defect chemistry formalism. I would like to thank Dr. Daniel Brinkman who taught me how to code efficiently improving the speed and efficiency of the numerical algorithms, techniques for reducing the memory footprint of code and helped me to figure out the deep bugs in the coding.

I take this opportunity to thank all my PhD committee members for their time and thoughts. Special thanks to Dr. Goodnick and Dr. Bertoni for taking time out of their busy schedule to be part of my committee.

I thank my research group members and ERC 558/525 occupants for creating a good work place environment to advance my knowledge and gain good insights through brain storming discussions and debates.

TABLE OF CONTENTS

Page

LIST OF TABLES ... viii

LIST OF FIGURES ... x

CHAPTER

1 INTRODUCTION ... 1

1.1 Literature Review ... 3

2 THEORETICAL FRAMEWORK ... 9

2.1 Generation and Recombination Rates ... 11

2.2 Correspondence with Radiative and SRH Recombination ... 14

2.3 Thermodynamic Relationship between Forward and Backward Rate Constants ... 16

2.4 Models ... 19

2.4.1 Reaction Models ... 19

2.4.1.1 Diffusion Limited with Attraction Model ... 20

2.4.1.2 Capture Radius Limited Model ... 20

2.4.1.3 Capture Cross Section Limited Model ... 20

2.4.1.4 Barrier Limited Model ... 21

2.4.1.5 Thermal Generation-Recombination Model ... 21

2.4.2 Diffusion Models ... 22

2.4.2.1 Arrhenius Diffusion Model ... 22

2.4.2.2 Free Carrier Diffusion Model ... 22

2.4.3 Material Models ... 23

2.4.3.1 Band Gap Model ... 23

2.4.3.2 Density of States Model ... 23

CHAPTER Page

2.4.3.3 Free Carrier Mobility Model 24

2.4.3.4 Formation Energy of Species Model 24

3 NUMERICAL ALGORITHMS 25

3.1 Mass and Charge Conservation in Reactions 30

3.2 Mass Conservation in Diffusion 33

3.3 Derivation of Discrete Differential Equations and Matrix Operators used in the Solver 33

3.3.1 Poisson Operator 33

3.3.2 Drift-Diffusion Operator 37

3.3.3 Flux Continuation in Discontinuous Media 40

4 USER INTERFACE 42

4.1 Software Architecture of Numerical Engine Module 45

5 APPLICATION/VALIDATION OF SOLVER 48

5.1 0-D Simulation of Thermally Generated Electrons and Holes 48

5.2 0-D Simulation Study of Copper Defects in CdTe 49

5.3 1D Simulation of Hetero-Junction CdTe Device 51

5.4 1-D Simulation of Cu Diffusion in Single Crystal CdTe 55

5.5 1D Simulation of Cu Diffusion in Full Stack CdTe Device 59

5.6 Efforts on Understanding of Chloride Treatment 64

5.7 Effects of Traps and Recombination Centers in Grain Boundaries . 72

5.8 Effects of Recombination Centers on Different Grain Boundary Structures 82

5.9 Experimental Characterization Emulation 85

5.9.1 CV Emulation and Hysteresis 87

CHAPTER Page

6 CONCLUSIONS AND FUTURE WORK 91

6.1 Future Work 92

6.1.1 Updates on PyCDTS 93

6.2 Acknowledgments and Contributions 94

REFERENCES 96

APPENDIX

A STANDARD SEMICONDUCTOR EQUATIONS FOR CHARGE CARRIERS FROM ELECTROCHEMICAL FORMULATION 100

B RELATIONSHIP BETWEEN TRANSITION LEVEL AND FORMATION ENTHALPY FOR DEFECTS 102

C LINEARIZED POISSON EQUATION 104

D TIME EVOLUTION OF THERMALLY GENERATED CARRIERS 106

E COPPER DOPING LIMITS IN CDTE SIMULATION RESULTS 109

F DFT PARAMETERS USED IN THE SX CDTE SIMULATIONS AS WELL AS FULL STACK CDTE SIMULATION 113

G CONCENTRATION PROFILES OF POINT DEFECTS, BAND DIAGRAMS AND OTHER PLOTS FOR FULL STACK CDTE CU SIMULATION 117

H CAPTURE AND EMISSION RATES 133

LIST OF TABLES

Table Page

1. Numerical Values Used in the Simulation. 50
2. Reactions Considered in the Cu Diffusion in SX CdTe Simulation. 57
3. Full Stack CdTe Device Structure. 60
4. Initial Concentrations Used for the Simulation. 61
5. Full Stack CdTe Device Structure. 65
6. Unbalanced Chemical Reactions Considered for Growth Simulations. 66
7. Dominant Point Defect in CdTe for Different Growth Conditions at 300K. . . . 67
8. Dominant Point Defect in CdTe for Different Growth Conditions at 800K and Rapidly Cool Down to 300K. 68
9. Dominant Point Defect in CdTe for Different Growth Conditions at 1200K and Rapidly Cool Down to 300K. 69
10. Donor Type Point Defect for CdTe Material System Considered in PyCDTS (Cd Rich Conditions). 70
11. Acceptor/Amphoteric Type Point Defect for CdTe Material System Considered in PyCDTS (Cd Rich Conditions). 71
12. Acceptor Type Point Defect from Recombination Nature to Trapping Nature. 75
13. Donor Type Point Defect from Recombination Nature to Trapping Nature. . . 78
14. Comparison of Performance with Different Grain Boundary Strctures with Acceptor Type Point Defect. 84
15. Comparison of Performance with Different Grain Boundary Structures with Donor Type Point Defect.. 84
16. Material Parameters. 114
17. Point Defect Formation Energies and Transition Levels in ZnTe and CdTe. . .115

Table Page

18.Point Defect Diffusion Prefactors and Barriers in ZnTe and CdTe. 115

19.Point Defect Formation Energies and Transition Levels in CdS and TCO. . . . 116

20.Point Defect Diffusion Prefactors and Barriers in CdS and TCO. 116

21.Short Circuit Current Density and Open Circuit Voltage From Simulations Just After 3min Anneal at 623K and at the End of Cool Down at 300K. 127

22.Conditions for Trap or Recombination Centers in the Context of PyCDTS Tool. 135

LIST OF FIGURES

Figure Page

1. Different Elements of TCAD Simulation. . . . 1
2. Finite Volume Mesh (FVM) Used for Discretizing Differential Equations. . . . 26
3. (A) Net Charge (B) Net Mass Without Corrections, (C) Net Charge and (D) Net Mass With Corrections. . . . 31
4. 1D Mesh for Discontinuous Media. . . . 40
5. Software Modules Used in the Coding of the Solver. . . . 43
6. GUI for the User to Setup a Simulation Problem. . . . 44
7. Software Architectural Organization of the Numerical Engine. . . . 47
8. Comparison of Analytical vs Numerical Solution for Time Evolution of Electrons and Holes Generated Thermally. . . . 49
9. Comparison of Hole Concentrations (Fermi Level) vs Total Cu Concentration. 52
10. Comparison of Cu Defect Concentrations vs Total Cu Concentration. . . . 53
11. Comparison of Total Mass and Charge Errors vs Total Cu Concentration. . . . 54
12. Schematics of Heterojunction CdTe Device Simulation. . . . 55
13. Comparison of JV Curves for CdTe Solar Cell Simulation. . . . 56
14. Copper Profile Comparison for 3min 350°C Anneal Recipe. . . . 58
15. Copper Profile Comparison for 6min 350°C Anneal Recipe. . . . 59
16. Copper Profile Comparison for 10min 300°C Anneal Recipe. . . . 60
17. Copper Profile Comparison for 20min 300°C Anneal Recipe. . . . 61
18. Temperature Profile Used for CdTe Full Stack Cu Simulation. . . . 62
19. JV Curve After Cool Down to 300K. . . . 63
20. JV Curves for Sensitivity Analysis. . . . 64
21. CdTe Device Structure with Vertical Grain Boundary. . . . 73

Figure Page

22.Ideal Electron Trapping. 74
23.Ideal Hole Trapping. 74
24.Ideal Recombination. 75
25.Light JV Curve with Acceptor Type Recombination to Acceptor Type Electron Trap. 76
26.Light JV Curve with Acceptor Type Recombination to Acceptor Type Hole Trap. 77
27.Light JV Curve with Donor Type Recombination to Donor Type Electron Trap. 79
28.Light JV Curve with Donor Type Recombination to Donor Type Hole Trap. . 80
29.Downward Band Bending Occurring due to Donor Type Point Defect at CdTe Vertical Grain Boundary. 81
30.Upward Band Bending Occurring due to Acceptor Type Point Defect at CdTe Vertical Grain Boundary. 82
31.CdTe Device Structure with Vertical Grain Boundary. 83
32.Comparison of Light JV Curves for Different GB Structures with Acceptor Type Recombination Center. 85
33.Comparison of Light JV Curves for Different GB Structures with Donor Type Recombination Center. 86
34.Test Structure Schematics for Emulating CV. 87
35.Input Stimulus and Output Response of CV Under Forward Bias Conditions. 88
36.Input Stimulus and Output Response of CV Under Reverse Bias Conditions. 89
37.CV Results and Mott Schottky Plot. 90
38.Hysteresis Occurring in the Structure as Observed with Simulation 90

Figure Page

39. Defect Formation Energy Wrt Valence Band Maxima (VBM). . . . 103
40. Cu Doping Limits in CdTe Under Cd Poor Conditions at 300K. . . . 111
41. Cu Doping Limits in CdTe Under Cd Slightly Poor Conditions at 300K. . . . 112
42. Initial Profile. . . . 118
43. Concentration Profile at the End of Anneal before Cool Down. . . . 119
44. Concentration Profile at the End of Anneal after Cool Down. . . . 120
45. Electrostatic Potential Profile at Initial Time, at 3mins and at End of Anneal. 121
46. Initial Band Diagram Profile. . . . 122
47. Band Diagram Profile at the End of Anneal Before Cool Down. . . . 123
48. Band Diagram Profile at the End of Anneal After Cool Down. . . . 124
49. Net Copper Concentration at Initial Time, at 3mins and at End of Anneal . . 125
50. Net Charge Density Near ZnTe/CdTe Interface at Initial Time, at 3mins and at End of Anneal. . . . 126
51. Net Charge Density Near CdTe/CdS and CdS/TCO Interface at Initial Time, at 3mins and at End of Anneal. . . . 127
52. Electric Field Near ZnTe/CdTe Interface at Initial Time, at 3mins and at End of Anneal. . . . 128
53. Electric Field Near CdTe/CdS and CdS/TCO Interface at Initial Time, at 3mins and at End of Anneal. . . . 129
54. Electric Field Profile in Cu Doped Full Stack CdTe Simulation. . . . 130
55. Electric Field Profile in Generic Dopants Full Stack CdTe Simulation. . . . 131
56. JV Curves Measured with Profiles Just After 3min Anneal at 623K and After Cool Down at 300K. . . . 132

Chapter 1

INTRODUCTION

Technology Computer-Aided Design (TCAD) refers to the use of computers in understanding and designing of new semiconductor processes, new device and developing compact circuit models for large scale simulation of integrated circuits. TCAD plays a vital role in the design cycles of new semiconductor processes and devices. TCAD modeling helps to reduce the research and development (R&D) cost, improves the fast characterization of processes and devices and shortens the design life cycles.

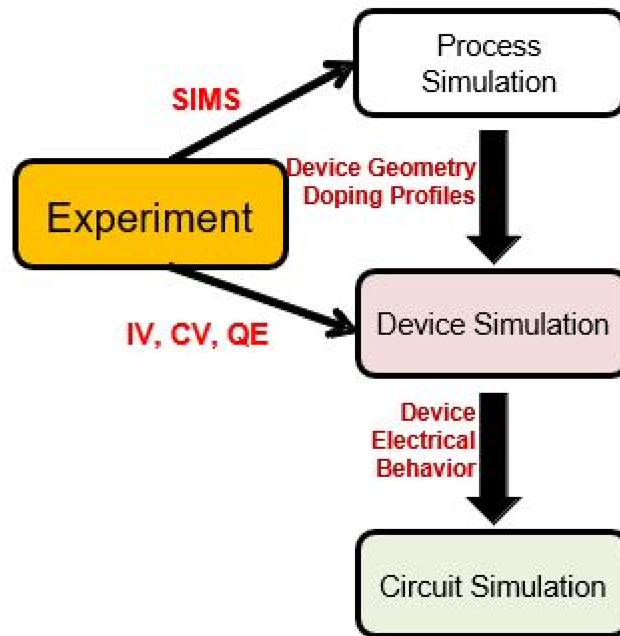

Figure 1. Different Elements of TCAD Simulation.

TCAD consists of three levels of modeling namely process level, device level and circuit level modeling (see Fig. 1). Process level modeling tools are physics based and help in understanding the process steps like ion implantation, diffusion, oxidation etc. They are called Process TCAD tools. Device level modeling tools are also physics based useful to model the device characteristics in terms of IV, CV etc., and are called Device TCAD tools [1]. Circuit level modeling tools are generally not physics based but helpful in compact model generation useful for performing large scale integrated circuit simulations.

TCAD also models issues related to reliability [1]. Commercially available TCAD tools [2, 3] have capabilities to perform reliability simulations. These commercial tools are useful in performing statistical variability of process and their effects in device behavior. The reliability issues are mainly related to the statistical variations (SV) in process and device fabrication and the time dependent variability (TDV) incurring due to the operational conditions of the device [4]. The TDV includes potential induced degradation(PID), light induced degradation (LID), temperature induced degradation (TID), bias temperature instability (BTI), electromigration, hot carrier injection degradation etc. In most of these processes a common underlying mechanism responsible for the degradation is due to the point defect dynamics and their chemical nature. Hence, the study of point defect dynamics along with free carriers plays a vital role in understanding the degradation mechanisms involved in many reliability studies.

The state of the art degradation models available in commercial tools [2, 3] are sufficient to understand the bias temperature instability, hot carrier injection degradation and other aging effects. These models are insufficient to explain the metastable behavior in devices. This was one of our motivations to develop a new

modeling and simulation approach to explain copper (Cu) metastability and reliability issues in cadmium telluride (CdTe) solar cell. The previously developed Unified Solver as part of the PREDICTS project was successful in explaining the Cu diffusion profiles and metastability issues in CdTe. One of the short comings of PREDICTS Unified Solver was the inability to extend the formulation to other dopant defect system like chlorine (Cl) or Arsenic (As). The reason for the short comings is due to the non user friendly incorporation of defect parameters and due to numerical algorithm instabilities and inaccuracies involved with chain reactions.

We resolved these issues in this present work by improving the graphical user interface and implementing advanced numerical algorithms that ensures the numerical accuracy and stability. In doing so we developed a generic framework that can be adapted to any material system and defects. We next present a brief review of similar work present in the literature.

1.1 Literature Review

The device TCAD started with work done by Gummel in 1964 on the one dimensional (1D) simulation of bipolar junction transistors by sequentially solving the partial differential equations (PDE) for the drift diffusion and Poisson equation self consistently [5]. The major breakthrough in the device modeling came through the introduction of Scharfetter-Gummel discretization of the continuity equation [6]. The process TCAD started with the development of SUPREME 1D process tool by Robert Dutton at Stanford University[7]. Statistical variability analysis was intrinsically a part of the process and device TCAD simulations. TCAD calibration for process and device model parameters was done against carefully designed experiments to improve

the predictive nature of TCAD simulations [4]. The time dependent variability or aging effects also occur in devices due to the operational conditions. The leading TCAD models to explain negative-bias temperature instability (NBTI) are reaction diffusion (RD) model and defect-centric (DC) model as given in Ref. [8]. In RD model, NBTI is explained with the de-passivation/passivation of defects present at the oxide/channel interface by hydrogen activated under stress conditions [8]. Hot carrier injection degradation is studied with trap degradation model and hot carrier stress model. The trap degradation model is based on the hydrogen transport in gate oxide using reaction-diffusion model and hot carrier stress model is based on trap formation at oxide/semiconductor interface due to field enhancement thermal interaction with the lattice [8]. Kirchheim and Kaeber explained the cause of electromigration as the annihilation and generation of defect vacancies in metals [9]. Other reliability effects in CMOS are described in Ref. [10]

In photovoltaic devices the main reliability issues are related to PID, LID and TID. The root cause analysis for LID in p-type PERC modules was presented in Ref. [11], where the authors associate the degradation of the cell to the dynamics of deep level donor point defects. Light and elevated temperature induced degradation (LeTID) is one of the main issue affecting the stability of perovskite solar cells (PSC) for long term operation. In Ref. [12], the authors show that gold diffusion into the active layer is one of the reasons for the instability and improved stability by using silver metal contact instead of gold. In that paper, it was suggested that the gold point defects act as recombination centers in the active layer of PSC. In Ref. [13], it was concluded that sodium ion diffusion in high defect density of silicon wafers is the main reason for the PID leading to smaller shunt resistance, open circuit voltage and efficiency.

From the above studies it is evident that the study of point defect dynamics

is important to understand and develop innovative ways to improve reliability of electronic and photovoltaic devices. Point defects are well studied in modeling the diffusion/thermal activation of dopants in silicon [14]. Sentaurus (Synopsys commercial TCAD tool) has ChargedReact model for diffusion [15], while Victory (Silvaco commercial TCAD tool) has five-stream model for diffusion [16]. Both of these models treat dopant diffusion in materials comprehensively by solving the continuity equations for five species namely dopant, two point defects (interstitial and vacancies) and two dopant-defect pairs [15, 16]. As noted in the user manuals, these are the most advanced and accurate models available in the corresponding commercial tools and also computationally expensive as they involve solving large number of equations. For example, to study diffusion of a m dopant in a structure, a system of at least $3m + 2$ non-linear coupled partial differential equations are needed to be solved as suggested in the tool manual. Usually, these models are not coupled self-consistently to Poisson equation to account for the electric fields although there are few flags to change the behavior. Electric fields are, by default, incorporated using the charge neutrality conditions.

The five stream models are not activated in device simulation or degradation simulation[17, 18]. Both tools comprehensively treat the transport of charge carriers in device simulations but not of point defects. Silvaco's Victory Device tool recently (from 2017 release) has added support to incorporate point defects in a limited way through chemical reactions [18], but user has to redefine these reactions again to incorporate the five stream model reactions. For degradation simulations both tools support degradation models with support only for Si-H point defect dynamics [17, 18]. Other degradation models incorporate the trap transients useful for MOS transistor degradation.

With these limitation on the available models in the state of the art tools, we were unable to study the microscopic origin of Cu metastability arising in the CdTe solar cells. Most of the degradation models are developed to handle unary material systems (like Si, Ge etc) but not for binary material system (like CdTe, GaAs etc). Thus, our goal was to develop a Unified Solver that comprehensively addresses the transport of point defects in CdTe by treating the same level of complexity for charge carriers and point defects in process, device and degradation simulations. This resulted in development of our tool called Unified Solver or more precisely PREDICTS1D[19] and PREDICTS2D[20]. With these tools, we were successful in explaining the Cu reliability and metastability in CdTe solar cell[21].

Da Guo et al., first explained the SIMS measurement of Cu profiles from single crystal CdTe measurements[22] using the point defects Cu_i^+,V_{Cd}^{2-},Cu_{Cd}^-,Cd_i^2+ and Cd_{Cd}^0 in CdTe and their respective defect chemical reactions. The theoretical and numerical details about methodology adopted for that simulation is given in Ref. [23]. The simulation used density functional theory(DFT) calculated parameters (namely diffusion barriers, diffusion prefactors, transistion levels, formation energies etc.), and provided a path to integrate the defect chemical reaction formalism into TCAD modeling. Further studies incorporated point defect ionization reactions and were used to explain the light soaking effects in CdTe solar cells [24]. $[Cu_iCu_{Cd}]^0$ point defect complex was needed to explain the mismatch between the DFT calculated diffusion barrier and the numerical simulation assumed diffusion barrier for Cu_i^+ and Cd_i^{2+} [21]. Hence with the PREDICTS Unified Solver it was possible to understand the underlying mechanism contributing the reliability issues in CdTe solar cells.

The main shortcomings of the PREDICTS Unified Solver were :

- Inability to incorporate new defect chemistry for Cl, As dopants in CdTe in a user friendly manner.
- Numerical instabilities arising with As defect chemical reactions, as the reactions involve chain reactions.
- Understanding Cl diffusion alongside with grain boundary (GB) segregation was not clear with the existing modeling assumptions [25].

To address the above shortcomings and improve the numerical algorithms we started to develop a second generation solver called PVRD-FASP Unified Solver. In this solver we created a new graphical user interface (GUI) with the help of the collaborators involved in the research project, improved the stability and accuracy of numerical algorithms and adopted a generalized theoretical formulation for comprehensively treating point defects and charge carriers on equal footing.

In subsequent chapters we describe the details about the theoretical formulation, numerical algorithms, GUI and finally provide simulation test cases for validating the solver and demonstrating the applications of the solver.The organization of this document is as listed below

- Chapter 1 provided introduction about the solver, the literature review about the modeling issues with reliability studies, and the shortcomings of the PREDICTS Unified Solver.
- Chapter 2 provides the theoretical framework details adopted in the PVRD-FASP Unified Solver.
- Chapter 3 presents the details about the numerical algorithms used and issues resulted with the implementation of the new algorithms (and how are they resolved).

- Chapter 4 gives details about the GUI and its flexibility for creating and running projects with the PVRD-FASP Unified Solver.
- Chapter 5 shows nine simulation examples that validate our solver and/or demonstrate the application of our solver in practical examples.
- Chapter 6 concludes our work and presents directions for future work.

In addition, appendices are added wherever there is a need for detailed explanations. Appendices also provide a few complimentary works that are present in the main text for completeness.

Chapter 2

THEORETICAL FRAMEWORK

Our theoretical framework closely follows the formulation given in Ref. [26]. The main equations that have been solved for describing transport of charge carriers are: the continuity equations, drift diffusion equation and the Poisson equation. These are given as

$$\frac{\partial n}{\partial t} = -\nabla \cdot \overrightarrow{J_n} + G_n - R_n, \tag{2.1}$$

$$\overrightarrow{J_n} = -\mu_n n \overrightarrow{E} - D_n \nabla n, \tag{2.2}$$

$$\frac{\partial p}{\partial t} = -\nabla \cdot \overrightarrow{J_p} + G_p - R_p, \tag{2.3}$$

$$\overrightarrow{J_p} = -\mu_p p \overrightarrow{E} - D_p \nabla p, \tag{2.4}$$

$$\nabla \cdot (\varepsilon \nabla \phi) = -p + n - N_D + N_A, \tag{2.5}$$

where $\overrightarrow{J_n}$ and $\overrightarrow{J_p}$ are the flux densities rather than the usual current densities used in semiconductor books, $\overrightarrow{E}$ is the electric field, ϕ is the electrostatic potential, G and R are the generation recombination rates modeled for radiative, Shockley Read Hall (SRH), Auger process etc., N_D and N_A are net donor and acceptor concentrations. The above equations are written for homogeneous structures. For heterostructures, a gradient term should be added to the drift-diffusion equations (2.2) and (2.4) (see Ref. [27]).

One can arrive at the same equations (see Appendix A) by treating diffusion flux as negative gradient of electrochemical potential (μ) defined as

$$\mu = G_f^0 + q\phi + kT \ln\left(\frac{u}{N_s}\right), \tag{2.6}$$

where G_f^0 is the formation energy of the species, ϕ is the electrostatic potential, q is the charge of the species, T is the temperature, k is the Boltzmann constant, u is the concentration of species and N_s is the maximum number of microstates the species can occupy. The above definition defines the chemical potential to be based on the formation energies and configuration entropies in dilute limit approximation [26, 28, 29]. Then, the diffusion flux is

$$\overrightarrow{J} = -\frac{D}{kT} u \nabla \mu \tag{2.7}$$

We note that in writing equations (2.6) and (2.7), we used the Einstein relationship between mobility and diffusivity (valid for non-degenerate statistics). Then, our transport equations for any arbitrary species (both charge carriers and point defects) can be written as

$$\frac{\partial u}{\partial t} = -\nabla \cdot \overrightarrow{J_i} + G_i - R_i, \tag{2.8}$$

$$\overrightarrow{J_i} = -\frac{D_i}{kT} u_i \nabla \left(G_{f,i}^0 + q_0 z_i \phi + kT \ln\left(\frac{u_i}{N_{s,i}}\right)\right), \tag{2.9}$$

$$-\nabla \cdot (\varepsilon \nabla \phi) = q_0 \sum_i z_i u_i, \tag{2.10}$$

where i is the index of the species, q_0 is the charge of an electron, z stands for the ionization number of the charge state with sign.

Next, we describe how to compute generation and recombination rates for both charge carriers and defects using defect chemical reaction kinetic theory.

2.1 Generation and Recombination Rates

The interactions between charge carriers and defect species can be represented as a defect chemical reaction [30]. Thus, one can use reaction kinetics to determine their time evolution. In this work, we consider defect chemical reaction involving at most two reactants and at most two products (i.e., bimolecular reactions). This approximation is always valid in the dilute limit, and most of the higher order interactions can be approximately modeled with bimolecular chemical reaction. The rate equation for a general defect chemical reaction with at most two reactant and two products

$$\mathrm{aA} + \mathrm{bB} \underset{K_b}{\overset{K_f}{\rightleftharpoons}} \mathrm{cC} + \mathrm{dD}, \tag{2.11}$$

is given as

$$-\frac{1}{a}\frac{d[A]}{dt} = -\frac{1}{b}\frac{d[B]}{dt} = \frac{1}{c}\frac{d[C]}{dt} = \frac{1}{d}\frac{d[D]}{dt} = K_f[A]^a[B]^b - K_b[C]^c[D]^d. \tag{2.12}$$

The above rate equation is still complex and we further restrict ourselves to stoichiometric coefficients a,b,c and d of either d=1 or d=0. Although this looks like a strong simplification to the domain of defect chemical reactions, it is still sufficient to cover the defect chemical interaction of interest.

If any of the species are involved in more than one chemical reaction, then the rate equation for that particular species have contribution from both reaction rate

constants of all the involved reactions. For example, if the reaction system is given as

$$\mathrm{A} + \mathrm{B} \underset{K_{b1}}{\overset{K_{f1}}{\rightleftharpoons}} \mathrm{C} + \mathrm{D}, \tag{2.13}$$

$$\mathrm{A} \underset{K_{b2}}{\overset{K_{f2}}{\rightleftharpoons}} \mathrm{E} + \mathrm{F}, \tag{2.14}$$

$$\mathrm{Null} \underset{K_{b3}}{\overset{K_{f3}}{\rightleftharpoons}} \mathrm{A} + \mathrm{G}, \tag{2.15}$$

then the rate equation for the time evolution of species A is given as

$$\frac{d[A]}{dt} = -K_{f1}[A][B] + K_{b1}[C][D] - K_{f2}[A] + K_{b2}[E][F] + K_{f3} - K_{b3}[A][G]. \tag{2.16}$$

The above rate equation can be elegantly represented as

$$\frac{d[A]}{dt} = U^T Q_A U + P_A U + K_A, \tag{2.17}$$

where U is a concentration vector (column) of length 7 given as

$$U = ([A], [B], [C], [D], [E], [F], [G])^T, \tag{2.18}$$

Q_A is a 7×7 matrix with all zero elements except for

$$q^A_{12} = q^A_{21} = -\frac{K_{f1}}{2}, q^A_{34} = q^A_{43} = \frac{K_{b1}}{2}, q^A_{56} = q^A_{65} = \frac{K_{b2}}{2}, q^A_{17} = q^A_{71} = -\frac{K_{b3}}{2}, \tag{2.19}$$

P_A is a row vector of length 7 with all elements zero except

$$p^A_1 = -K_{f2}, \tag{2.20}$$

and K_A is the constant term given as K_{f3}.

The representation of rate as (2.17) can be extended to any species and we can write the corresponding Q, P, K as functions of reaction rate constants. Consider a general reaction rate equation

$$\frac{du_i}{dt} = \sum_{k=1}^{M} \sum_{j=1}^{M} a^i_{jk} u_j u_k + \sum_{j=1}^{M} b^i_j u_j + c^i, \tag{2.21}$$

for $i = 1, 2, ..., M$ where M is the total number of species and a,b,c are the reaction rate constants in which the species i is involved.

Then the variable Q^i, P^i, K^i can be calculated as

$$q^i_{jk} = q^i_{kj} = \begin{cases} \frac{1}{2}a^i_{jk}, & \text{if } j \neq k \\ a^i_{jk}, & \text{if } j = k \\ 0, & \text{otherwise} \end{cases} \tag{2.22}$$

$$p^i_j = b^i_j, K = c^i. \tag{2.23}$$

Thus, the generation recombination rate can be expressed as

$$G_i - R_i = \left.\frac{du_i}{dt}\right|_{reactions} = U^T Q^i U + P^i U + K^i. \tag{2.24}$$

With this form we can write the net rate as reaction operator $R(U)$ as

$$R(U) = U^T QU + PU + K, \tag{2.25}$$

where Q is M×M×M array, P is M×M array and K is M×1 array. The major advantage of writing $R(U)$ in this form is with the calculation of the Jacobian of the reaction operator with the formula

$$J_R(U) = (Q + Q^T)U + P \tag{2.26}$$

With this, we complete the formulation of generation recombination rates using the defect chemical reaction kinetics. Next, we show that we can recover the standard expressions for radiative and SRH generation recombination rates for charge carriers using this formulation.

2.2 Correspondence with Radiative and SRH Recombination

For a radiative process, the generation-recombination rates in the continuity equation of charge carriers can be expressed as

$$G - R = b\left(n_i^2 - np\right). \tag{2.27}$$

Considering the radiative process as a chemical reaction, we can write the equivalent reaction as

$$\text{Null} \underset{K_b}{\overset{K_f}{\rightleftharpoons}} \mathrm{e}_c{}^- + \mathrm{h}_v{}^+, \tag{2.28}$$

where e_c^- and h_v^+ denote free electron and hole in conduction and valence band of the material. Hence, the rate equation is given as

$$\begin{aligned} \frac{d[e_c^-]}{dt} = \frac{d[h_v^+]}{dt} &= K_f - K_b[e_c^-][h_v^+] \\ &= K_b\left(\frac{K_f}{K_b} - [e_c^-][h_v^+]\right). \end{aligned} \tag{2.29}$$

Thus, if the ratio of forward to backward rate constant is n_i^2 we can easily see that (2.27) and (2.29) are equivalent. The thermodynamics of reactants and products results in such condition in the ratio (see Section 2.3).

For SRH processes, the generation and recombination rate on a single defect in steady-state is given as in Ref. [31]

$$G - R = \frac{(n_1 p_1 - np)}{\dfrac{n + n_1}{C_p} + \dfrac{p + p_1}{C_n}}. \tag{2.30}$$

The equivalent reaction representing the SRH process in case of acceptor type species can be written as

$$\mathrm{A}^0 \underset{K_{b1}}{\overset{K_{f1}}{\rightleftharpoons}} \mathrm{A}^- + \mathrm{h}_v{}^+,$$
$$\mathrm{A}^- \underset{K_{b2}}{\overset{K_{f2}}{\rightleftharpoons}} \mathrm{A}^0 + \mathrm{e}_c{}^-. \tag{2.31}$$

The rate equations can be written as

$$\frac{d[A^0]}{dt} = -\frac{d[A^-]}{dt} = -K_{f1}[A^0] + K_{b1}[A^-][h_v^+] + K_{f2}[A^-] - K_{b2}[A^0][e_c^-], \tag{2.32}$$
$$\frac{d[e_c^-]}{dt} = K_{f2}[A^-] - K_{b2}[A^0][e_c^-], \tag{2.33}$$
$$\frac{d[h_v^+]}{dt} = K_{f1}[A^0] - K_{b1}[A^-][h_v^+]. \tag{2.34}$$

From (2.32) we note that $[A^0] + [A^-]$ is constant in time (say $[A]^{tot}$). Hence in steady state equilibrium for $[A^0]$ and $[A^-]$ we have

$$[A^0] = \frac{K_{f2} + K_{b1}p}{K_{f1} + K_{f2} + K_{b1}p + K_{b2}n}[A]^{tot}, \tag{2.35}$$
$$[A^-] = \frac{K_{f1} + K_{b2}n}{K_{f1} + K_{f2} + K_{b1}p + K_{b2}n}[A]^{tot},$$

where $[h_v^+] = p$ and $[e_c^-] = n$ is used for notational simplicity. Using (2.35) in (2.33) and (2.34) with few algebraic simplifications we can write

$$\frac{dn}{dt} = \frac{dp}{dt} = \frac{K_{f1}K_{f2} - K_{b1}K_{b2}np}{K_{f1} + K_{f2} + K_{b1}p + K_{b2}n}[A]^{tot}. \tag{2.36}$$

Now if the ratio of the reaction rate constants is restricted as

$$\frac{K_{f1}}{K_{b1}} = p_1 = N_v e^{\frac{E_v - E_T}{kT}}, \frac{K_{f2}}{K_{b2}} = n_1 = N_c e^{-\frac{E_c - E_T}{kT}}, \tag{2.37}$$

then (2.36) can be simplified further as

$$G - R = \frac{(n_1 p_1 - np)}{\dfrac{n + n_1}{K_{b1}} + \dfrac{p + p_1}{K_{b2}}} [A]^{tot}, \tag{2.38}$$

which is equivalent to (2.30). Equation (2.37) will hold based on the thermodynamics of reactants and products as shown in the next section (see Section 2.3). A similar equivalence can be shown for donor type centers as well. Similar analysis can be performed for the case of Auger generation recombination as well.

2.3 Thermodynamic Relationship between Forward and Backward Rate Constants

Consider a generation reaction

$$\sum_{i=1}^{N} x_i X_i \underset{K_b}{\overset{K_f}{\rightleftharpoons}} \sum_{j=1}^{M} y_j Y_j, \tag{2.39}$$

with N reactants and M products. At thermodynamic equilibrium the difference in the chemical potential of reactants and products should be zero. Thus, we have

$$\Delta_r G = \sum_{i=1}^{N} x_i \mu_{X_i} - \sum_{j=1}^{M} y_j \mu_{Y_j}, \tag{2.40}$$

where $\Delta_r G$ is the Gibb's free energy change of reaction, μ is the chemical potential of the species which can written from (2.6) neglecting the electrostatic potential as

$$\mu_{X_i} = G^0_{f,X_i} + kT \ln \left(\frac{[X_i]}{N_{s,X_i}} \right). \tag{2.41}$$

Note that the chemical potential here is defined as the sum of species formation energy and its configurational entropy in the dilute limit as expressed in Ref. [26, 28, 29]. Thus, at equilibrium we have

$$\sum_{i=1}^{N} \left(x_i G^0_{f,X_i} + kT \ln \left(\frac{[X_i]^{x_i}_{eq}}{N^{x_i}_{s,X_i}} \right) \right) = \sum_{j=1}^{M} \left(y_j G^0_{f,Y_j} + kT \ln \left(\frac{[Y_j]^{y_j}_{eq}}{N^{y_j}_{s,Y_j}} \right) \right) \tag{2.42}$$

Upon simplification we obtain

$$\frac{\prod_{j=1}^{M}[Y_j]_{eq}^{y_j}}{\prod_{i=1}^{N}[X_i]_{eq}^{x_i}} = \frac{\prod_{j=1}^{M} N_{s,Y_j}^{y_j}}{\prod_{i=1}^{N} N_{s,X_i}^{x_i}} \exp\left(-\frac{\Delta_r G^0}{kT}\right), \tag{2.43}$$

where $\Delta_r G^0$ is the standard enthalpy change of reaction or standard reaction Gibb's energy defined as

$$\Delta_r G^0 = \sum_{j=1}^{M} y_j G^0_{f,Y_j} - \sum_{i=1}^{N} x_i G^0_{f,X_i}. \tag{2.44}$$

We also know that at equilibrium we have

$$K_f \prod_{i=1}^{N}[X_i]_{i,eq}^{x_i} - K_b \prod_{j=1}^{M}[Y_j]_{j,eq}^{y_j} = 0. \tag{2.45}$$

Hence using (2.43) and (2.45) we can write the equilibrium constant as

$$K_{eq} = \frac{K_f}{K_b} = \frac{\prod_{j=1}^{M} N_{s,Y_j}^{y_j}}{\prod_{i=1}^{N} N_{s,X_i}^{x_i}} \exp\left(-\frac{\Delta_r G^0}{kT}\right) \tag{2.46}$$

Therefore, the reaction rate constants follow a fixed ratio. Applying this for the reaction (2.28) we have

$$\frac{K_f}{K_b} = N_{s,e_c^-} N_{s,h_v^+} \exp\left(-\frac{G^0_{f,e_c^-} + G^0_{f,h_v^+}}{kT}\right) \tag{2.47}$$

The number of microstates for electrons in conduction band and hole in valence band are N_C and N_V respectively. The formation energies of electrons in conduction band and holes in valence band referenced from vacuum level is

$$G^0_{f,e_c^-} = -\chi, G^0_{f,h_v^+} = \chi + E_g, \tag{2.48}$$

where χ is the electron affinity of the material and E_g is the band gap of the material. Thus, we have the ratio as

$$\frac{K_f}{K_b} = N_C N_V \exp\left(-\frac{E_g}{kT}\right) = n_i^2. \tag{2.49}$$

Considering the reactions in (2.31), we have

$$\frac{K_{f1}}{K_{b1}} = \frac{N_{s,A^-}N_{s,h_v^+}}{N_{s,A^0}} \exp\left(-\frac{G^0_{f,A^-} + G^0_{f,h_v^+} - G^0_{f,A^0}}{kT}\right), \tag{2.50}$$

$$\frac{K_{f2}}{K_{b2}} = \frac{N_{s,A^0}N_{s,e_c^-}}{N_{s,A^-}} \exp\left(-\frac{G^0_{f,A^0} + G^0_{f,e_c^-} - G^-_{f,A^-}}{kT}\right) \tag{2.51}$$

where the formation energies are given as

$$\begin{aligned} G^0_{f,A^0} &= E_{f,A^0} - \chi - E_g, \\ G^0_{f,A^-} &= E_{f,A^0} - sign(A^-)E_T - \chi - E_g, \\ G^0_{f,e_c^-} &= -\chi, G^0_{f,h_v^+} = \chi + E_g. \end{aligned} \tag{2.52}$$

Here $sign(A^-)$ is the sign of the charge on the species, E_T is the trap level (transition level from 0/- see Ref. [32]) with respect to vacuum and E_{f,A^0} is the defect formation energy of neutral species calculated through Density Functional Theory (DFT) (see Appendix B for details on how transistion levels of species are related to the formation energies of its corresponding neutral species). Assuming that the microstates for neutral and charged species are nearly same, we arrive at

$$\begin{aligned} \frac{K_{f1}}{K_{b1}} &= N_V \exp\left(-\frac{\chi + E_g + E_T}{kT}\right) = N_V \exp\left(\frac{E_V - E_T}{kT}\right), \\ \frac{K_{f2}}{K_{b2}} &= N_C \exp\left(-\frac{-\chi - E_T}{kT}\right) = N_C \exp\left(-\frac{E_C - E_T}{kT}\right) \end{aligned} \tag{2.53}$$

where we have used the relations

$$E_C = -\chi, E_V = -\chi - E_g \tag{2.54}$$

Hence, the thermodynamics guarantees that the SRH process is recovered from our reaction formulation. Thus, the thermodynamics guarantees the equivalence as a defect chemical reaction.

2.4 Models

We have described the theory behind our approach and the differential equations involved in the transport of charge carriers and point defects. In this section we describe the models we have employed in our solver.

2.4.1 Reaction Models

Although thermodynamics provides the ratio of forward and backward rate constants, we still have to find either one of the rate constants. For this, we use reaction models that provide the rate constant of the reaction either forward rate or backward rate. Consider a general reaction

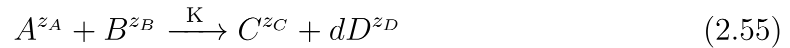

$$A^{z_A} + B^{z_B} \xrightarrow{\text{K}} C^{z_C} + dD^{z_D} \tag{2.55}$$

where d can be either 0 or 1 with 0 being single product reaction and 1 being two product reaction, z_X is the ionization of species X. The diffusion-controlled reaction rate constant [26, 33] is given as

$$K = 4\pi R_{capt} \left(D_A + D_B\right) \exp\left(-\frac{E_A}{kT}\right), \tag{2.56}$$

where R_{capt} is the capture radius, D_X is the diffusivity of the species X, E_A is the activation energy of reaction ($E_A \geq 0$) representing the probability of a collision resulting in the formation of product. The various type of reaction models used in the solver [34] are as given below.

2.4.1.1 Diffusion Limited with Attraction Model

This model is used when the two reactants or products have opposite charges i.e., $z_A \times z_B < 0$. In such a case, there is Coulombic force of attraction between the species and hence activation barrier is zero. Also, the capture radius is given by the Onsager radius, which is the radius at which the Coulombic energy is equal to the thermal energy. The Onsager radius can be calcuated as

$$R_{Onsager} = q^2 \frac{|z_A z_B|}{4\pi\varepsilon kT}. \tag{2.57}$$

Hence the rate constant is given as

$$K = q^2 \frac{|z_A z_B|}{\varepsilon kT} (D_A + D_B) \tag{2.58}$$

2.4.1.2 Capture Radius Limited Model

This model is used for reaction when $z_A \times z_B \geq 0$ and assumes the activation energy of the reaction to be zero. Thus, the rate constant is given as

$$K = 4\pi R_{capt} (D_A + D_B) \tag{2.59}$$

For this model, the user has to specify the capture radius R_{capt} as an input.

2.4.1.3 Capture Cross Section Limited Model

If one of the reactant of (2.55) is charge carrier, then the sum of diffusivities can be approximated as

$$D_A + D_B \approx D_{e/h} \tag{2.60}$$

Also, it is common to represent charge carrier capture reaction rate constant as product of capture cross section and thermal velocities. Thus, the rate constant is given as

$$K = \sigma_{e/h} v_{th,e/h} \tag{2.61}$$

In case of diffusion limited with attraction model with charge carrier, the capture cross section of carrier is given as

$$\sigma_{e/h} = \frac{4\pi R_{Onsager} D_{e/h}}{v_{th,e/h}} \tag{2.62}$$

For capture radius limited model, with charge carrier as reactant, the user has to input the capture cross section as a parameter.

2.4.1.4 Barrier Limited Model

This model is used for reactions with single reactant and single product. The rate constant is given as

$$K = \nu \exp\left(-\frac{E_b}{kT}\right) \tag{2.63}$$

where ν is the attempt frequency of reaction (pre-factor), and E_b is the activation barrier height of reaction.

2.4.1.5 Thermal Generation-Recombination Model

This model is used when the reaction is given by (2.28). The backward rate is equated to the band-to-band recombination rate coefficient B of the material. Currently, we assume that the coefficient B is independent of temperature, although Refs. [35, 36] show it as being temperature dependent.

2.4.2 Diffusion Models

2.4.2.1 Arrhenius Diffusion Model

The diffusion coefficient of species is assumed to have Arrhenius relationship with temperature given as

$$D(T) = D_0 \exp\left(-\frac{E_D}{kT}\right) \tag{2.64}$$

where D_0 is the diffusion pre-factor, E_D is the diffusion barrier. For this model, the user should specify the pre-factors and barriers for the species.

2.4.2.2 Free Carrier Diffusion Model

The diffusion coefficient of free carriers are assumed to follow Einstein relationship given as

$$D_{e/h} = \mu_{e/h} \frac{kT}{q} \tag{2.65}$$

Mobility of the free carriers is a material parameter. Hence, the diffusivities of free carriers are dependent on the mobility models of the material being studied.

2.4.3 Material Models

2.4.3.1 Band Gap Model

The temperature dependence of the bandgap of a material is assumed to follow the Varshni model [37], given as

$$E_g(T) = E_0 - \alpha \frac{T^2}{T+\beta}, \tag{2.66}$$

where E_0 is the band gap at 0K, α and β are fitting parameters.

2.4.3.2 Density of States Model

The density of states for free carriers are computed through

$$N_{s,e/h} = 2\left(\frac{2\pi m_{eff,e/h} m_0 kT}{h^2}\right)^{\frac{3}{2}} \tag{2.67}$$

For defect species the density of microstates are given as

$$N_s = g_{atom} \times g_{elec} \times N_0 \tag{2.68}$$

where g_{atom}, g_{elec} are the atomic and electronic degeneracy factor of the defect species and N_0 is the lattice site density of the site the defect is occupying in the host material [34]. The sites available to the point defects in the host material depends on the host crystal structure, size of the point defect, etc. For example interstitial defects can be stable in a hexagonal site or tetrahedral site in a zinc-blende crystal structure.

2.4.3.3 Free Carrier Mobility Model

The free carrier mobility is assumed to follow the relationship

$$\mu_{e/h} = \mu_{e/h,300K} \left(\frac{T}{300} \right)^{-\frac{3}{2}} \tag{2.69}$$

2.4.3.4 Formation Energy of Species Model

For charge carriers the formation energy is given as

$$\Delta H_f(e) = -\chi, \quad \Delta H_f(h) = \chi + E_g(T) \tag{2.70}$$

For point defect species the formation energy [34] is given as

$$\Delta H_f(X^{z_X}) = \Delta H_f(X^0) - sign(z_X) \times \left(\frac{T}{300} \Delta E_T - \chi - E_g(T) \right) \tag{2.71}$$

where ΔE_T is the transition level with respect to the valence band of the material. This information is generally available with DFT calculations.

Chapter 3

NUMERICAL ALGORITHMS

The equations (2.8)-(2.10) are solved numerically by discretizing them in space and time. The equation (2.9) can be rewritten as

$$\overrightarrow{J_i} = -D_i e^{-\Psi_i} \nabla \left(u_i e^{\Psi_i} \right) \tag{3.1}$$

where

$$\Psi_i = \frac{G^0_{f,i} + q_0 z_i \phi - kT \ln N_{s,i}}{kT} \tag{3.2}$$

Thus, the differential equations to be solved are given as

$$\begin{aligned} \frac{\partial u_i}{dt} &= \nabla \cdot \left(D_i e^{-\Psi_i} \nabla \left(u_i e^{\Psi_i} \right) \right) + G_i - R_i, \\ -\nabla \cdot (\varepsilon \nabla \phi) &= q_0 \sum_i z_i u_i. \end{aligned} \tag{3.3}$$

for $i = 1, 2, ..., M$(total number of species) and subjected to the defined boundary conditions given by the user. We consider our simulation domain to be always rectangular, and the boundaries on the left and right to have zero flux and zero field as shown in Figure 2.

We define our mixed (Robin) boundary condition as

$$A_i u_i + B_i J_i^x = C_i, \tag{3.4}$$

specified on the top and the bottom boundaries of the simulation domain. Here A, B can only take values either 0 or 1. If A is zero then the boundary condition is Neumann and if B is zero then it is Dirichlet.

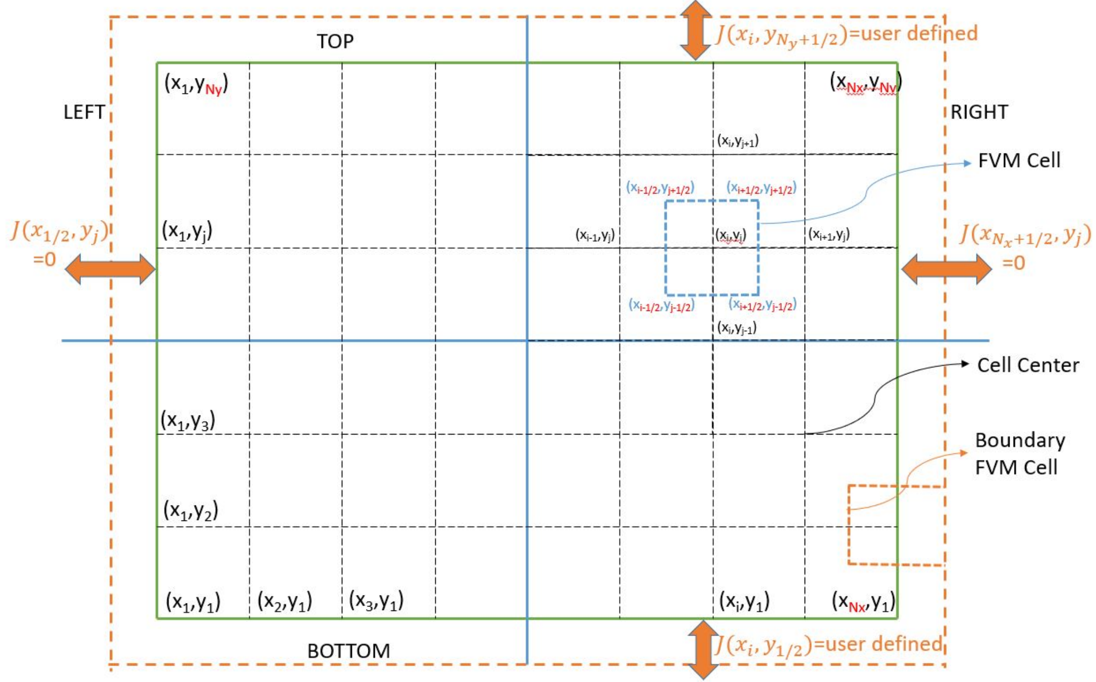

Figure 2. Finite Volume Mesh (FVM) Used for Discretizing Differential Equations.

We express (3.3) in terms of operators as

$$\frac{\partial U}{\partial t} = (T_\phi U + R_U)\,,$$
$$\hat{P}\phi = Q^T U, \tag{3.5}$$

where T_ϕ is the transport operator which depends on the potential with inclusion of the boundary conditions, R_U is the reaction operator, $\hat{P}$ is the Poisson operator (that includes the boundary conditions) and Q^T is the transpose of charge vector. The transport and Poisson operators are space dependent and reaction operator is space independent but dependent on the concentrations. Based on the choice of the discretization scheme and the numerical method, we can express the operators as matrices as follows

$$T_\phi = \mathcal{T}_\phi, \quad \hat{P} = \mathcal{P}, \quad R_U = \mathcal{R}_\mathcal{U} \tag{3.6}$$

The size of the matrices are $(N_xN_yM)\times(N_xN_yM)$ where N_x is the total number of discretized steps in the X-direction, N_y is the total number of discretized steps in Y-direction and M is the total number of species. In this work, we use Scharfetter-Gummel discretization scheme [6] and finite volume method to write the discrete differential equation and form operator matrices (see Appendix 3.3 for details).

We use backward time or implicit Euler scheme and hence we have

$$\begin{aligned}\frac{U^{t+\Delta t}-U^t}{\Delta t} &= \left(\mathcal{T}_{\phi^{t+\Delta t}}U^{t+\Delta t}+\mathcal{R}_{U^{t+\Delta t}}\right),\\ \mathcal{P}\phi^{t+\Delta t} &= Q^TU^{t+\Delta t}.\end{aligned} \tag{3.7}$$

For a two-dimensional problem the complete operator matrix $\mathcal{T}_\phi+\mathcal{R}$ has large bandwidth with relatively small sparsity. To efficiently solve the problem we split the operators (called time operator splitting) and rearrange the concentration vector such that the bandwidth of the matrices $\mathcal{R}$, $\mathcal{T}_\phi$ is less than the maximum value between N_x, N_y, M. We first solve the equation

$$\frac{U^{t+\Delta t}-U^t}{\Delta t}=\mathcal{R}_{U^{t+\Delta t}}, \tag{3.8}$$

for $U^{t+\Delta t}$ with Newton method. The solution is achieved iteratively by solving the equation

$$\begin{aligned}(I-\Delta t\mathbb{J}_{U^k})\,\delta U^k &= -\left(U^k-R_{U^k}-U^t\right),\\ U^{k+1}-U^k &= \delta U^k,\end{aligned} \tag{3.9}$$

until the convergence criteria is achieved, which is given as

$$\frac{||\delta U^k||_2}{||U^k||_2}\leq Tol. \tag{3.10}$$

We use this solution (say $\tilde{U}$) as initial condition and solve the coupled equations

$$\frac{U^{t+\Delta t}-\tilde{U}}{\Delta t}=\mathcal{T}_{\phi^{t+\Delta t}}U^{t+\Delta t},\quad \mathcal{P}\phi^{t+\Delta t}=Q^TU^{t+\Delta t}, \tag{3.11}$$

for $U^{t+\Delta t}$ and $\phi^{t+\Delta t}$ through Gummel iteration [38]. We also use linearization for the Poisson equation to improve the solver stability. The linearized Poisson equation is iteratively solved inside each Gummel iteration. We can represent the linearized Poisson equation as

$$\mathcal{P}\phi + \mathcal{L}\phi = Q^T \mathcal{L}_1 U + \mathcal{L}\phi^{old}, \tag{3.12}$$

where $\mathcal{L}$ is a diagonal matrix dependent on previous Gummel iteration solution of ϕ, U, ϕ^{old} and $\mathcal{L}_1$ is also a diagonal matrix that depends only on the previous Gummel iteration solution of ϕ and ϕ^{old}. Here ϕ^{old} is the current Gummel iteration's previous solution of linearized Poisson solver iteration. See the Appendix C for details on $\mathcal{L}$ and $\mathcal{L}_1$.

In the mth Gummel iteration we first update the concentrations with the equation

$$\left(I - \Delta t \mathcal{T}_{\phi^{m-1}}\right) U^m = \tilde{U}. \tag{3.13}$$

We then use this updated solution U^m in the linearized Poisson equation. In the mth Gummel iteration with kth linearized Poisson iteration we update the potential as

$$\left(\mathcal{P} + \mathcal{L}(U^m, \phi^m_{k-1}, \phi^{m-1})\right) \phi^m_k = Q^T \mathcal{L}_1(\phi^m_{k-1}, \phi^{m-1}) U^m + \mathcal{L}(U^m, \phi^m_{k-1}, \phi^{m-1}) \phi^m_{k-1}. \tag{3.14}$$

The Poisson iteration is run until convergence is achieved within a fixed number of iterations (say k_{max}) and Gummel iteration potential is updated as

$$\phi^m = \begin{cases} \phi^m_k, & \text{if } k < k_{max} \\ \phi^m_{k_max}, & \text{otherwise} \end{cases} \tag{3.15}$$

Then convergence condition to stop the Gummel iteration is given as:

$$\frac{||U^{m+1} - U^m||_2}{||U^m||_2} \leq Tol_{Gum,Conc}, \text{ and } |\phi^{m+1} - \phi^m| \leq Tol_{Gum,pot}. \tag{3.16}$$

The concentrations and the potential after the convergence of Gummel iteration will be the solution of the differential equations at time $t + \Delta t$ computed from solution at t. If the convergence is not achieved in either reaction iteration or Gummel iteration, i.e., (3.10) or (3.16) conditions are not met in fixed number of iterations, then we reduced the time step Δt by half and rerun the time loop. If the convergence is achieved continuously for 16 steps, then we increase the time step Δt by a factor of 2. The value of 16 steps is chosen arbitrarily after we tested our code with simple simulations.

With such numerical algorithm scheme, we can simulate problems not only in 2D, but also in 1D and 0D. The 0D problem refers to solving only reactions which are a system of first order non-linear stiff differential equations.

Because of the choice of implicit scheme, the algorithm is numerically stable. Also, because of the Newton step in the reactions and solving reactions in simultaneous fashion as compared to sequential fashion in our previous generation solver [23, 39], we get improvements in the numerical accuracy and speed. For a 0D test case with 16 species and 20 reactions we compared the speeds of our new solver with that of our previous generation solver and we achieved a speed improvement of about $17\times$ [40]. Chain reactions with intermediate species and very fast reactions are handled extremely efficiently by the L-stable reaction scheme.

Although the numerical algorithms imporved speed, stability and accuracy, we still faced few challenges in the numerical methods. Some of them arise because of finite precision arithmetic involved in the computational machine, others are related to the conditioning of the matrices. We next describe the challenges we have solved and comment on few unsolved challenges.

3.1 Mass and Charge Conservation in Reactions

The total mass and charge in any chemical reaction has to be a conserved quantity of the reaction. In our numerical simulations, we observed that the net mass and charge are not conserved to a required accuracy in the reaction solver. This is shown in Figure 3 (a) and (b) subplots. We verified that this issue occurs mainly because of the finite precision arithmetic involved in the numerical algorithm. We first show that the analytical equations do not have this issue. For simplicity we illustrate this problem for the case of 0D (and the same can be extended to 1D and 2D problem with operators).

Consider the equation given in (2.25), which can be written as

$$\frac{dU}{dt} = R(U) = U^T QU + PU + K. \tag{3.17}$$

We know that there exist conservation vectors such that

$$C^T U = const. \tag{3.18}$$

Thus, we have

$$\begin{aligned} \frac{d}{dt} C^T U &= 0 \\ \implies C^T \frac{d}{dt} U &= 0 \\ \implies C^T R(U) &= 0 \\ \implies C^T \frac{d}{dU} R(U) &= 0 \\ \implies C^T \mathbb{J}_R(U) &= 0 \end{aligned} \tag{3.19}$$

Applying this to (3.9), it can be shown that in exact arithmetic

$$C^T U^{t+\Delta t} = C^T U^t. \tag{3.20}$$

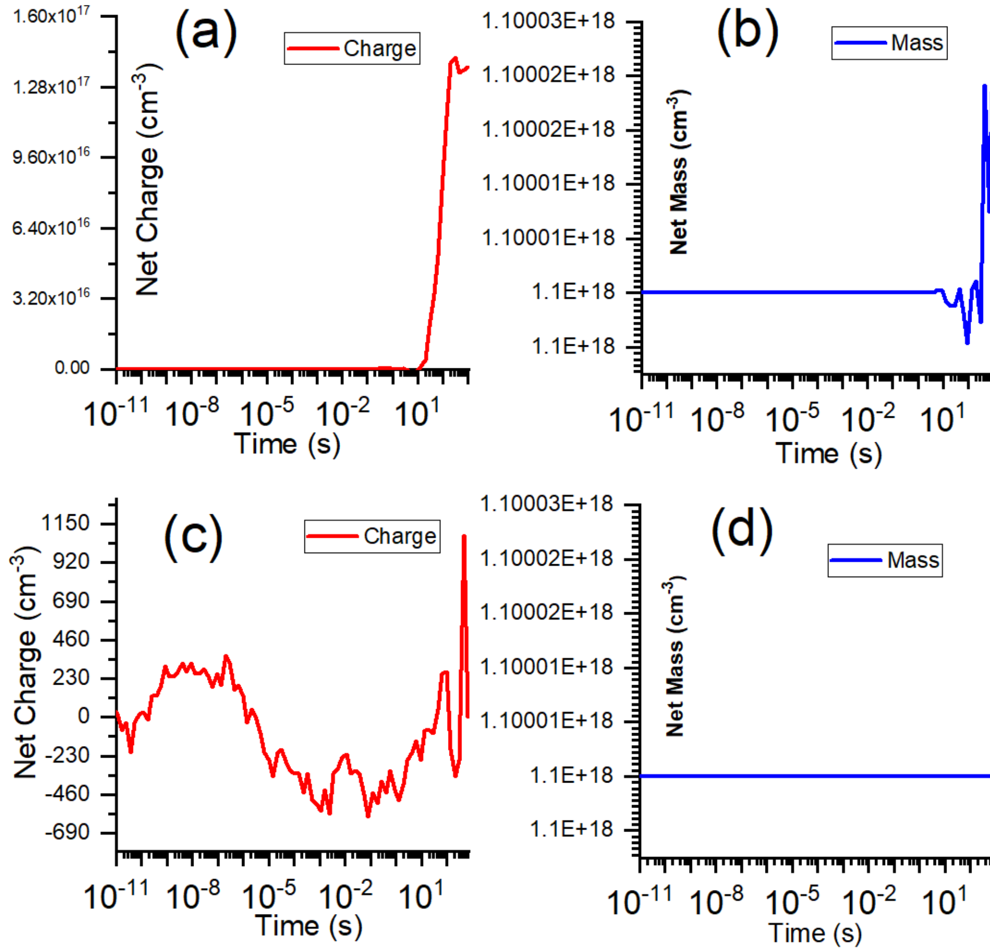

Figure 3. (a) Net Charge (b) Net Mass Without Corrections, (c) Net Charge and (d) Net Mass With Corrections.

But in finite arithmetic we are seeing

$$C^T R(U) \neq 0, \quad C^T \mathbb{J}_R(U) \neq 0. \tag{3.21}$$

In some simulations even when both equations are satisfied, we still find conservation issue. In that case we observed that

$$\begin{aligned} C^T \left(I - \Delta t \mathbb{J}_R(U)\right)^{-1} &\neq C^T, \\ C^T \left(I - \Delta t \mathbb{J}_R(U)\right) &= C^T. \end{aligned} \tag{3.22}$$

This clearly shows that the matrix $(I - \Delta t \mathbb{J}_R(U))$ is ill conditioned. Based on these observations we propose a non linear projection scheme to correct this problem. This scheme is described next.

Suppose that we have $U_{numerical}$ and U_{exact} as the numerical solution and the exact solution. Let the difference between them be projected in the direction of unit normal concentration vector $P = \frac{U}{||U||_2}$ with a weight α. Then we can write

$$
\begin{aligned}
C^T \left(U_{numerical} - \alpha P\right) = C^T U_{exact} = C^T U^t, \\
\implies \alpha C^T P = C^T (U_{numerical} - U^t), \\
\implies U_{exact} = U_{numerical} - \frac{C^T (U_{numerical} - U^t}{C^T P} P, \\
\implies U_{exact} = \left(I - \frac{PC^T}{C^T P}\right) U_{numerical} + \frac{PC^T}{C^T P} U^t.
\end{aligned}
\tag{3.23}
$$

Thus, one can correct the solution using the above expression. One issue with this approach is that it cannot be applied whenever we have $C^T P = 0$. To avoid such conditions, we perturb the direction P with a random number between 1 and 2. This makes P vector close to unit normal vector in the direction of concentrations but $C^T P \neq 0$. Even with this, there are some initial conditions that still give $C^T P = 0$. This happens with zero initial conditions whenever elements of C are non-zero. To avoid those cases as well, we restrict the initial conditions to non-zero values of negligible concentrations around 1cm^{-3} or 1e-16 cm^{-3}. With these corrections we get the net charge and mass conservation in reactions to an accuracy we expected. This is illustrated in Figure 3 (c) and (d) subplots. Note that without corrections the net charge conservation differs by 1e17 cm^{-3} whereas after corrections it differs by 1e3 cm^{-3} order of magnitude. In case of net mass conservation, it differs by 1e13 cm-3 and after correction it is 1e3 cm^{-3}.

3.2 Mass Conservation in Diffusion

Another issues we resolved in the PVRD-FASP solver is related to the diffusion operator. Under insulating boundary conditions (i.e., zero field and zero flux conditions), a long time simulation (in decades time scale) was not conserving the total mass of the species. We observed that this was happening only at large time steps (Δt). We concluded that with large time steps the diffusion/transport matrix was becoming ill conditioned. We resolved this issues by using an augmented system with conservation equations. This scheme was inspired from the method of pseudo inverses whenever the matrix becomes ill conditioned.

3.3 Derivation of Discrete Differential Equations and Matrix Operators used in the Solver

As mentioned in the previous section, (3.5) has space dependent operators namely transport and Poisson operator. Thus, based on the choice of the numerical scheme the differential equations have to be discretized. We use finite volume numerical discretization method (FVM) in our solver. The discretized equations for transport and Poisson operators in FVM scheme are derived in the following subsections.

3.3.1 Poisson Operator

From (3.3) and (3.5), the Poisson operator is given as

$$\hat{P} \equiv -\nabla \cdot (\varepsilon \nabla) \tag{3.24}$$

Since ε is material dependent, the discretized equations should ensure the continuity of the displacement electric vector. The displacement vector is given as

$$\overrightarrow{\mathcal{D}} = -\varepsilon \nabla \phi \tag{3.25}$$

The condition guaranteeing the continuity (see 3.3.3) is given as

$$\mathcal{D}^x_{i+1/2,j} = -\frac{1}{h^x_{i,j}} \frac{2}{\frac{1}{\varepsilon_{i,j}} + \frac{1}{\varepsilon_{i+1,j}}} (\phi_{i+1,j} - \phi_{i,j}) \tag{3.26}$$

$$\mathcal{D}^x_{i-1/2,j} = -\frac{1}{h^x_{i-1,j}} \frac{2}{\frac{1}{\varepsilon_{i-1,j}} + \frac{1}{\varepsilon_{i,j}}} (\phi_{i,j} - \phi_{i-1,j}) \tag{3.27}$$

$$\mathcal{D}^y_{i,j+1/2} = -\frac{1}{h^y_{i,j}} \frac{2}{\frac{1}{\varepsilon_{i,j}} + \frac{1}{\varepsilon_{i,j+1}}} (\phi_{i,j+1} - \phi_{i,j}) \tag{3.28}$$

$$\mathcal{D}^y_{i,j-1/2} = -\frac{1}{h^y_{i,j-1}} \frac{2}{\frac{1}{\varepsilon_{i,j-1}} + \frac{1}{\varepsilon_{i,j}}} (\phi_{i,j} - \phi_{i,j-1}) \tag{3.29}$$

where

$$h^x_{i,j} = x_{i+1,j} - x_{i,j} \tag{3.30}$$

The Poisson equation can be written as

$$\nabla \cdot \overrightarrow{\mathcal{D}} = \rho \tag{3.31}$$

Thus using the finite volume method we can write the above as

$$\int \nabla \cdot \overrightarrow{\mathcal{D}}\, dx\, dy = \int \rho\, dx\, dy \tag{3.32}$$

$$\Longrightarrow \oint \overrightarrow{\mathcal{D}} \cdot \hat{n}\, dl = \int \rho\, dx\, dy \tag{3.33}$$

where $\hat{n}$ is unit normal vector in the direction normal to the circle.Thus, at node (i, j) we have

$$\oint_{rect\{(x_{i-1/2},y_{j-1/2}),(x_{i+1/2},y_{j+1/2})\}} \overrightarrow{\mathcal{D}} \cdot \hat{n}\, dl = \int_{x_{i-1/2}}^{x_{i+1/2}} \int_{y_{j-1/2}}^{y_{j+1/2}} \rho_{i,j}\, dx\, dy \tag{3.34}$$

The circular integral on the lhs can be simplified as

$$\oint_{rect\{(x_{i-1/2},y_{j-1/2}),(x_{i+1/2},y_{j+1/2})\}} \overrightarrow{\mathcal{D}} \cdot \hat{n}\, dl$$
$$= \int_{x_{i-1/2}}^{x_{i+1/2}} \left(\mathcal{D}^y_{i,j+1/2} - \mathcal{D}^y_{i,j-1/2}\right) dx + \int_{y_{j-1/2}}^{y_{j+1/2}} \left(\mathcal{D}^x_{i+1/2,j} - \mathcal{D}^x_{i-1/2,j}\right) dy$$
$$= \frac{h^x_{i-1,j} + h^x_{i,j}}{2} \left(\mathcal{D}^y_{i,j+1/2} - \mathcal{D}^y_{i,j-1/2}\right) + \frac{h^y_{i,j-1} + h^y_{i,j}}{2} \left(\mathcal{D}^x_{i+1/2,j} - \mathcal{D}^x_{i-1/2,j}\right) \quad (3.35)$$

To simplify the notation complexity we denote

$$H^x_{i,j} = \frac{h^x_{i-1,j} + h^x_{i,j}}{2} \quad H^y_{i,j} = \frac{h^y_{i,j-1} + h^y_{i,j}}{2} \quad (3.36)$$

Thus, at node (i, j) we have the discretized differential equation as

$$-\frac{H^x_{i,j}}{h^y_{i,j}} \frac{2}{\dfrac{1}{\varepsilon_{i,j}} + \dfrac{1}{\varepsilon_{i,j+1}}} (\phi_{i,j+1} - \phi_{i,j}) + \frac{H^x_{i,j}}{h^y_{i,j-1}} \frac{2}{\dfrac{1}{\varepsilon_{i,j-1}} + \dfrac{1}{\varepsilon_{i,j}}} (\phi_{i,j} - \phi_{i,j-1})$$
$$-\frac{H^y_{i,j}}{h^x_{i,j}} \frac{2}{\dfrac{1}{\varepsilon_{i,j}} + \dfrac{1}{\varepsilon_{i+1,j}}} (\phi_{i+1,j} - \phi_{i,j}) + \frac{H^y_{i,j}}{h^x_{i-1,j}} \frac{2}{\dfrac{1}{\varepsilon_{i-1,j}} + \dfrac{1}{\varepsilon_{i,j}}} (\phi_{i,j} - \phi_{i-1,j})$$
$$= H^x_{i,j} H^y_{i,j} \rho_{i,j} \quad (3.37)$$

for all interior nodes (i, j). At boundaries the above equations differs. At top boundary we have

$$\mathcal{D}^{top}_i + \frac{H^x_{i,j}}{h^y_{i,j-1}} \frac{2}{\dfrac{1}{\varepsilon_{i,j-1}} + \dfrac{1}{\varepsilon_{i,j}}} (\phi_{i,j} - \phi_{i,j-1})$$
$$-\frac{H^y_{i,j}}{h^x_{i,j}} \frac{2}{\dfrac{1}{\varepsilon_{i,j}} + \dfrac{1}{\varepsilon_{i+1,j}}} (\phi_{i+1,j} - \phi_{i,j}) + \frac{H^y_{i,j}}{h^x_{i-1,j}} \frac{2}{\dfrac{1}{\varepsilon_{i-1,j}} + \dfrac{1}{\varepsilon_{i,j}}} (\phi_{i,j} - \phi_{i-1,j})$$
$$= H^x_{i,j} H^y_{i,j} \rho_{i,j} \quad (3.38)$$

where $\mathcal{D}^{top}_i$ can be found from boundary condition equation

$$A^{top}_i \phi_{i,j} + B^{top}_i \mathcal{D}^{top}_i = C^{top}_i \quad (3.39)$$

Using 2D 5-point stencil the above equations can be written as

$$sN_{i,j}\phi_{i,j+1} + sS_{i,j}\phi_{i,j-1} + sE_{i,j}\phi_{i+1,j} + sW_{i,j}\phi_{i-1,j} + sC_{i,j}\phi_{i,j} = sF_{i,j} \tag{3.40}$$

where the coefficients are given as

$$sN_{i,j} = -\frac{H^x_{i,j}}{h^y_{i,j}} \frac{2}{\dfrac{1}{\varepsilon_{i,j}} + \dfrac{1}{\varepsilon_{i,j+1}}} \tag{3.41}$$

$$sS_{i,j} = -\frac{H^x_{i,j}}{h^y_{i,j-1}} \frac{2}{\dfrac{1}{\varepsilon_{i,j-1}} + \dfrac{1}{\varepsilon_{i,j}}} \tag{3.42}$$

$$sE_{i,j} = -\frac{H^y_{i,j}}{h^x_{i,j}} \frac{2}{\dfrac{1}{\varepsilon_{i,j}} + \dfrac{1}{\varepsilon_{i+1,j}}} \tag{3.43}$$

$$sW_{i,j} = -\frac{H^y_{i,j}}{h^x_{i-1,j}} \frac{2}{\dfrac{1}{\varepsilon_{i-1,j}} + \dfrac{1}{\varepsilon_{i,j}}} \tag{3.44}$$

$$sC_{i,j} = \frac{H^x_{i,j}}{h^y_{i,j}} \frac{2}{\dfrac{1}{\varepsilon_{i,j}} + \dfrac{1}{\varepsilon_{i,j+1}}} + \frac{H^x_{i,j}}{h^y_{i,j-1}} \frac{2}{\dfrac{1}{\varepsilon_{i,j-1}} + \dfrac{1}{\varepsilon_{i,j}}} \tag{3.45}$$

$$+ \frac{H^y_{i,j}}{h^x_{i,j}} \frac{2}{\dfrac{1}{\varepsilon_{i,j}} + \dfrac{1}{\varepsilon_{i+1,j}}} + \frac{H^y_{i,j}}{h^x_{i-1,j}} \frac{2}{\dfrac{1}{\varepsilon_{i-1,j}} + \dfrac{1}{\varepsilon_{i,j}}} \tag{3.46}$$

$$sF = H^x_{i,j} H^y_{i,j} \rho_{i,j} \tag{3.47}$$

At boundaries the changes are given as

$$sC_{i,j}\Big|_{j=1} = sC_{i,j}\Big|_{j=1} + H^x_{i,1}\frac{A^{bottom}_i}{B^{bottom}_i} \quad sF_{i,j}\Big|_{j=1} = sF_{i,j}\Big|_{j=1} + H^x_{i,1}\frac{C^{bottom}_i}{B^{bottom}_i} \tag{3.48}$$

$$sC_{i,j}\Big|_{j=N_y} = sC_{i,j}\Big|_{j=N_y} - H^x_{i,1}\frac{A^{top}_i}{B^{top}_i} \quad sF_{i,j}\Big|_{j=N_y} = sF_{i,j}\Big|_{j=N_y} - H^x_{i,1}\frac{C^{top}_i}{B^{top}_i} \tag{3.49}$$

The matrix in FVM for the Poisson operator is thus given as

$$[\mathcal{P}]\begin{bmatrix}\phi_{1,1}\\ \phi_{1,2}\\ \vdots\\ \phi_{2,1}\\ \phi_{2,2}\\ \vdots\\ \phi_{i,j}\\ \vdots\end{bmatrix}=\begin{bmatrix}sF_{1,1}\\ sF_{1,2}\\ \vdots\\ sF_{2,1}\\ sF_{2,2}\\ \vdots\\ sF_{i,j}\\ \vdots\end{bmatrix} \tag{3.50}$$

where

$$\mathcal{P}=\begin{bmatrix}
sC_{1,1} & sN_{1,1} & \dots & sE_{1,1} & \dots & \dots & \dots & \dots & \dots & \dots\\
sS_{1,2} & sC_{1,2} & sN_{1,2} & \dots & sE_{1,2} & \dots & \dots & \dots & \dots & \dots\\
\vdots & \ddots & \ddots & \ddots & \vdots & \vdots & \dots & \dots & \dots & \dots\\
sW_{2,1} & \dots & sS_{2,1} & sC_{2,1} & sN_{2,1} & \dots & sE_{2,1} & \dots & \dots & \dots\\
0 & sW_{2,2} & \dots & sS_{2,2} & sC_{2,2} & sN_{2,2} & \dots & sE_{2,2} & \dots & \dots\\
\vdots & \vdots & \ddots & \vdots & \ddots & \ddots & \ddots & \vdots & \ddots & \vdots\\
\vdots & \vdots & \vdots & sW_{i,j} & \vdots & sS_{i,j} & sC_{i,j} & sN_{i,j} & \vdots & sE_{i,j}\\
\vdots & \vdots & \vdots & \vdots & \vdots & \vdots & \vdots & \vdots & \vdots & \vdots
\end{bmatrix} \tag{3.51}$$

3.3.2 Drift-Diffusion Operator

The transport (drift-diffusion) equation is given as

$$\frac{\partial u}{dt}=-\nabla\cdot\overrightarrow{J}\quad\text{where}\quad\overrightarrow{J}=-De^{-\Psi}\nabla\left(ue^{\Psi}\right) \tag{3.52}$$

Using Scharfetter-Gummel discretization and applying similar analysis as above we can write

$$J^x_{i+1/2,j} = -\frac{1}{h^x_{i,j}} \frac{2}{\dfrac{1}{D_{i,j}} + \dfrac{1}{D_{i+1,j}}} \left(Ber(-\Delta\Psi^x_{i,j})u_{i+1,j} - Ber(\Delta\Psi^x_{i,j}u_{i,j} \right) \tag{3.53}$$

$$J^x_{i-1/2,j} = -\frac{1}{h^x_{i,j}} \frac{2}{\dfrac{1}{D_{i-1,j}} + \dfrac{1}{D_{i,j}}} \left(Ber(-\Delta\Psi^x_{i-1,j})u_{i,j} - Ber(\Delta\Psi^x_{i-1,j}u_{i-1,j} \right) \tag{3.54}$$

$$J^y_{i,j+1/2} = -\frac{1}{h^y_{i,j}} \frac{2}{\dfrac{1}{D_{i,j}} + \dfrac{1}{D_{i,j+1}}} \left(Ber(-\Delta\Psi^y_{i,j})u_{i,j+1} - Ber(\Delta\Psi^y_{i,j}u_{i,j} \right) \tag{3.55}$$

$$J^y_{i,j-1/2} = -\frac{1}{h^y_{i,j}} \frac{2}{\dfrac{1}{D_{i,j-1}} + \dfrac{1}{D_{i,j}}} \left(Ber(-\Delta\Psi^y_{i,j-1})u_{i,j} - Ber(\Delta\Psi^y_{i,j-1}u_{i,j-1} \right) \tag{3.56}$$

Thus the discretized transport differential equations are given as

$$H^x_{i,j} H^y_{i,j} \frac{u_{i,j} - u^t_{i,j}}{\Delta t} = \frac{H^x_{i,j}}{h^y_{i,j}} \frac{2}{\dfrac{1}{D_{i,j}} + \dfrac{1}{D_{i,j+1}}} \left[Ber(-\Delta\Psi^y_{i,j})u_{i,j+1} - Ber(\Delta\Psi^y_{i,j})u_{i,j} \right] \tag{3.57}$$

$$- \frac{H^x_{i,j}}{h^y_{i,j-1}} \frac{2}{\dfrac{1}{D_{i,j-1}} + \dfrac{1}{D_{i,j}}} \left[Ber(-\Delta\Psi^y_{i,j-1})u_{i,j} - Ber(\Delta\Psi^y_{i,j-1})u_{i,j-1} \right] \tag{3.58}$$

$$+ \frac{H^y_{i,j}}{h^x_{i,j}} \frac{2}{\dfrac{1}{D_{i,j}} + \dfrac{1}{D_{i+1,j}}} \left[Ber(-\Delta\Psi^x_{i,j})u_{i+1,j} - Ber(\Delta\Psi^x_{i,j})u_{i,j} \right] \tag{3.59}$$

$$- \frac{H^y_{i,j}}{h^x_{i-1,j}} \frac{2}{\dfrac{1}{D_{i-1,j}} + \dfrac{1}{D_{i,j}}} \left[Ber(-\Delta\Psi^x_{i-1,j})u_{i,j} - Ber(\Delta\Psi^x_{i-1,j})u_{i-1,j} \right] \tag{3.60}$$

Using the same 2D 5-point stencil we can express the coefficients as

$$sN = -\frac{H^x_{i,j}}{h^y_{i,j}} \frac{2}{\dfrac{1}{D_{i,j}} + \dfrac{1}{D_{i,j+1}}} Ber(-\Delta\Psi^y_{i,j}) \tag{3.61}$$

$$sS = -\frac{H^x_{i,j}}{h^y_{i,j-1}} \frac{2}{\dfrac{1}{D_{i,j-1}} + \dfrac{1}{D_{i,j}}} Ber(\Delta\Psi^y_{i,j-1}) \tag{3.62}$$

$$sE = -\frac{H^y_{i,j}}{h^y_{i,j}} \frac{2}{\dfrac{1}{D_{i,j}} + \dfrac{1}{D_{i+1,j}}} Ber(-\Delta\Psi^x_{i,j}) \tag{3.63}$$

$$sW = -\frac{H^y_{i,j}}{h^x_{i-1,j}} \frac{2}{\dfrac{1}{D_{i-1,j}} + \dfrac{1}{D_{i,j}}} Ber(\Delta\Psi^x_{i-1,j}) \tag{3.64}$$

$$sC = \frac{H^x_{i,j} H^y_{i,j}}{\Delta t} + \frac{H^x_{i,j}}{h^y_{i,j}} \frac{2}{\dfrac{1}{D_{i,j}} + \dfrac{1}{D_{i,j+1}}} Ber(\Delta\Psi^y_{i,j}) \tag{3.65}$$

$$+ \frac{H^x_{i,j}}{h^y_{i,j-1}} \frac{2}{\dfrac{1}{D_{i,j-1}} + \dfrac{1}{D_{i,j}}} Ber(-\Delta\Psi^y_{i,j-1}) \tag{3.66}$$

$$+ \frac{H^y_{i,j}}{h^y_{i,j}} \frac{2}{\dfrac{1}{D_{i,j}} + \dfrac{1}{D_{i+1,j}}} Ber(\Delta\Psi^x_{i,j}) \tag{3.67}$$

$$+ \frac{H^y_{i,j}}{h^x_{i-1,j}} \frac{2}{\dfrac{1}{D_{i-1,j}} + \dfrac{1}{D_{i,j}}} Ber(-\Delta\Psi^x_{i-1,j}) \tag{3.68}$$

$$sF = H^x_{i,j} H^y_{i,j} \frac{u^t_{i,j}}{\Delta t} \tag{3.69}$$

As usual one has to modify the equations at the top and bottom boundaries as

$$sC_{i,j}\Big|_{j=1} = sC_{i,j}\Big|_{j=1} + H^x_{i,1} \frac{A^{bottom}_i}{B^{bottom}_i}, \quad sF_{i,j}\Big|_{j=1} = sF_{i,j}\Big|_{j=1} + H^x_{i,1} \frac{C^{bottom}_i}{B^{bottom}_i} \tag{3.70}$$

$$sC_{i,j}\Big|_{j=N_y} = sC_{i,j}\Big|_{j=N_y} - H^x_{i,1} \frac{A^{top}_i}{B^{top}_i}, \quad sF_{i,j}\Big|_{j=N_y} = sF_{i,j}\Big|_{j=N_y} - H^x_{i,1} \frac{C^{top}_i}{B^{top}_i} \tag{3.71}$$

The matrix $\mathcal{T}_\phi$ for the transport operator can be similarly obtained.

3.3.3 Flux Continuation in Discontinuous Media

Consider a general flux equation given as

$$\vec{J} = -D\nabla u \tag{3.72}$$

For simplicity we consider a 1D case with the discretized mesh as given in Fig. 4.

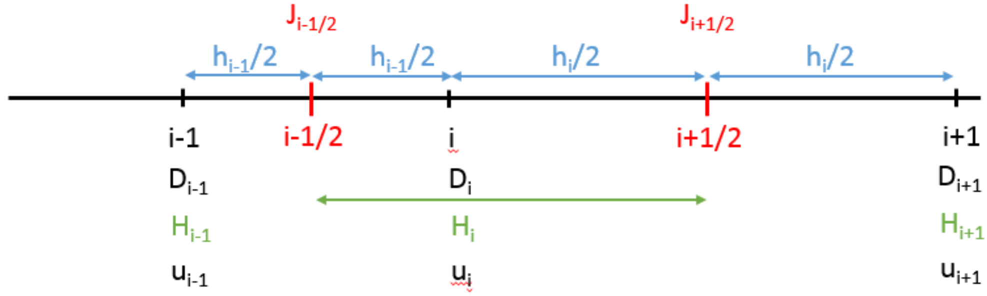

Figure 4. 1D Mesh for Discontinuous Media.

For this the flux evaluated from the lhs of point $i+1/2$ is given as

$$J^-_{i+1/2} = -D^-_{i+1/2}\frac{du}{dx}\Big|^-_{i+1/2} \tag{3.73}$$

$$= -D_i\frac{u_{i+1/2}-u_i}{h_i/2} \tag{3.74}$$

The same flux evaluated from the rhs is given as

$$J^+_{i+1/2} = -D^+_{i+1/2}\frac{du}{dx}\Big|^+_{i+1/2} \tag{3.75}$$

$$= -D_{i+1}\frac{u_{i+1}-u_{i+1/2}}{h_i/2} \tag{3.76}$$

Thus we should have

$$D_i \frac{u_{i+1/2} - u_i}{h_i/2} = D_{i+1} \frac{u_{i+1} - u_{i+1/2}}{h_i/2} \tag{3.77}$$

$$\implies u_{i+1/2} \left(\frac{D_i + D_{i+1}}{h_i} \right) = u_{i+1} \left(\frac{D_{i+1}}{h_i} \right) + u_i \left(\frac{D_i}{h_i} \right) \tag{3.78}$$

$$\implies u_{i+1/2} = u_{i+1} \frac{D_{i+1}}{D_i + D_{i+1}} + u_i \frac{D_i}{D_i + D_{i+1}} \tag{3.79}$$

Substituting this back in (3.73) we get

$$J^-_{i+1/2} = -\frac{2D_i}{h_i} \left(u_{i+1} \frac{D_{i+1}}{D_i + D_{i+1}} + u_i \frac{D_i}{D_i + D_{i+1}} - u_i \right) \tag{3.80}$$

$$= -\frac{2D_i}{h_i} \left(\frac{D_{i+1}}{D_i + D_{i+1}} u_{i+1} + \left(\frac{D_i}{D_i + D_{i+1}} - 1 \right) u_i \right) \tag{3.81}$$

$$= -\frac{2D_i D_{i+1}}{h_i (D_i + D_{i+1})} (u_{i+1} - u_i) \tag{3.82}$$

$$= -\frac{2}{h_i} \frac{1}{\frac{1}{D_i} + \frac{1}{D_{i+1}}} (u_{i+1} - u_i) \tag{3.83}$$

We also note that

$$J^+_{i+1/2} = J^-_{i+1/2} = -\frac{2}{h_i} \frac{1}{\frac{1}{D_i} + \frac{1}{D_{i+1}}} (u_{i+1} - u_i) \tag{3.84}$$

$$= -\frac{D_{eq}}{h_i} (u_{i+1} - u_i) \tag{3.85}$$

where

$$D_{eq} = \frac{2}{\frac{1}{D_i} + \frac{1}{D_{i+1}}} \tag{3.86}$$

With this we conclude the discussion of numerical algorithms used in our solver.

Chapter 4

USER INTERFACE

The user interface of the solver allows one to properly and easily setup the simulation problem of interest and correctly input the required parameters to the species and reactions. Because of the complexity of the intended problems for the solver, we classify the entire program flow into eight software modules as shown in Fig. 5. The user interaction is mainly with Graphical User Interface (GUI) module of the program. The numerical algorithms and schemes used in the solver are coded and comprise the Numerical Engine module of the program. The Physical Model Library provides the required code for implementing the physical models from Section 2.4. The Stress Measurement Library is responsible for setting up the process recipes, stress recipes, measurement recipes etc. The Reporting Engine module implements code for plotting the results like concentration distribution profiles, potential profiles, performance characteristics, like current-voltage plots, etc. The Database module stores all of the parameter values used in the physical models for materials, species, reactions etc., in dictionaries and projects. The Task Manager module manages all the operations requested by the user and acts as a central hub to communicate with other modules. The Documentation Package module documents the programming structure of the implemented code, user manuals, developer manuals, technical notes about models, etc.

The GUI interface as seen by the user is shown in Fig. 6. On the left panel of the interface we have complete database (named as APL_111_poor in the Fig. 6) to hold dictionaries and projects. Inside the dictionaries we have collection of

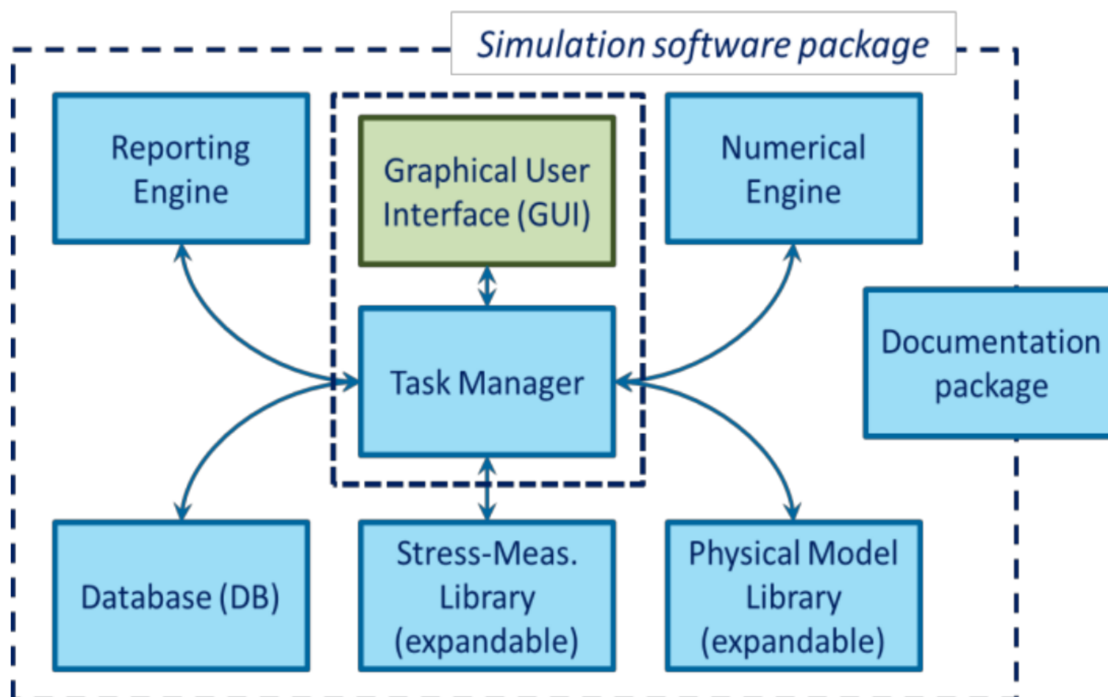

Figure 5. Software Modules Used in the Coding of the Solver.

Elements, Lattice Sites, Species, Reactions, Materials and Mechanisms. Projects hold the collection of user's created projects that define the simulation structure, reactions in the structure and process recipe/device measurement recipe to be applied for structure. The complete database can be saved and shared with other users. Dictionaries are intended to hold a read only data so that users while creating a project can avoid accidentally editing the first principle parameters. They can be edited in projects locally, but those edits will not be reflected in dictionaries.

In the right-hand panel, the user can edit and modify the project. In the General panel group user can set the name of the project, and the description about the project. In Project properties panel group, the user can set or modify the type of the structure and define new structure. Currently, 0D, 1D and 2D are supported.

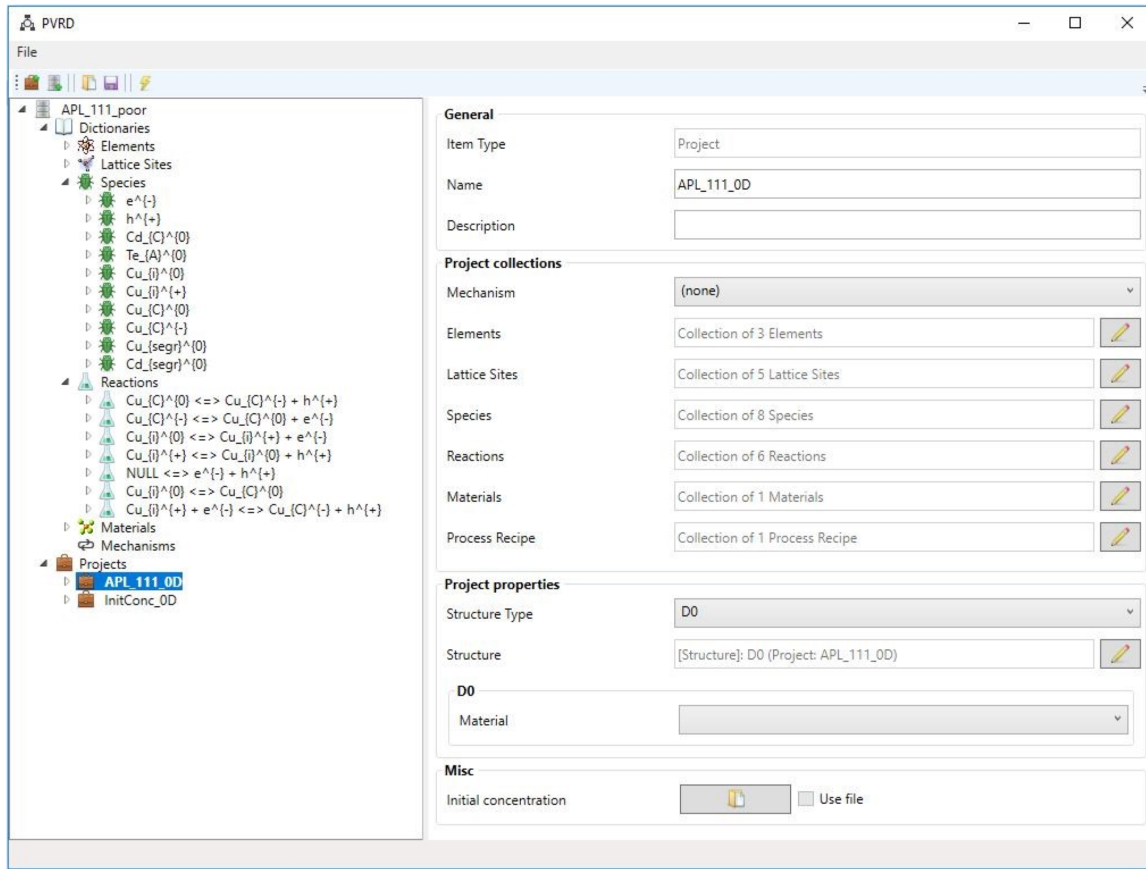

Figure 6. GUI for the User to Setup a Simulation Problem.

In the project collection group panel user can define or modify the process recipes, reactions, species to the user's simulation task. The Lattice Sites and Elements option in the project collection group panel are for verification purposes. Mechanisms option is mainly used to set the collection of reactions useful for a simulation of interested processes involving specific dopant. For example, to study Cu doping/activation in CdTe the user does not need to know reactions responsible for Cu doping/activation. Mechanisms helps user to pick up reactions applicable to a specific dopant of interest. The Misc panel group is useful to set non-uniform initial concentration profiles through initial conditions files.

4.1 Software Architecture of Numerical Engine Module

We follow object-oriented programming paradigm of MATLAB to code the Numerical Engine Module. The entire numerical engine is implemented in a top level class named as Numerical_Engine. The solvers used in the numerical engine class are classified as reaction, diffusion and Poisson solvers. Each solver has an abstract class with the required initialization method and declaration for the common method called 'solver(dt)'. This method takes time step as input and returns the solution of the solver after the time step. With these abstract classes, a developer can implement solver classes for different numerical schemes and can easily integrated with numerical engine class. Also, we have a class implementing the numerical algorithm of the engine. With these class based programming, we were able to implement many variations of solvers and algorithms. They are

- Diffusion Solvers (DS)
  - Slotboom discretization based DS (unstable)
  - Scharfetter Gummel (SG) discretization based DS (stable and default)
  - SG discretization and pseudo inverses based DS (diffusion mass corrections)
- Reaction Solver (RS)
  - Serialized block matrix operation based RS
  - Vectorized block matrix operation based RS (improved speed and default)
- Poisson Solver (PS)
  - Simple PS without linearization (unstable)
  - Linearized PS (stable and default)
  - Linearized PS neglecting Gummel iteration feedback (unstable)

  - Damped PS (stable but damping factor is unknown and simulation dependent)
  - Differential Algebraic Equation (DAE) based PS (slower)

- Solver Algorithm
  - Operator splitting scheme (faster but suffers numerical issues)
  - Full operator scheme (slower but does not suffer numerical issues and default)

To develop the numerical algorithms and solvers in parallel, without affecting the development of the other software modules in the simulation software package (see Fig. 5) we defined the interface between the Numerical Engine module and other modules. The interface provides the variables in and out of the Numerical Engine module and these variables have a specific dimensions (for examples variables can be constants or vectors or matrices or 3D arrays, etc). With the interface and class structure the architecture of the numerical engine class is well defined as shown in Fig. 7. This architecture gives flexibility to easily incorporate new solver classes and algorithms into numerical engine without affecting the parts of global software code. Such architecture provided the defect chemistry model development, GUI development and numerical algorithm development in a concurrent way improving the overall productivity of the software. Also it acts as a testing hub to run numerical algorithm experiments on realistic test cases providing ways to identify and propose new solution schemes. This methodology helped to identify the mass and charge conservation issues in particular part of the numerical engine code, which otherwise would be harder to debug.

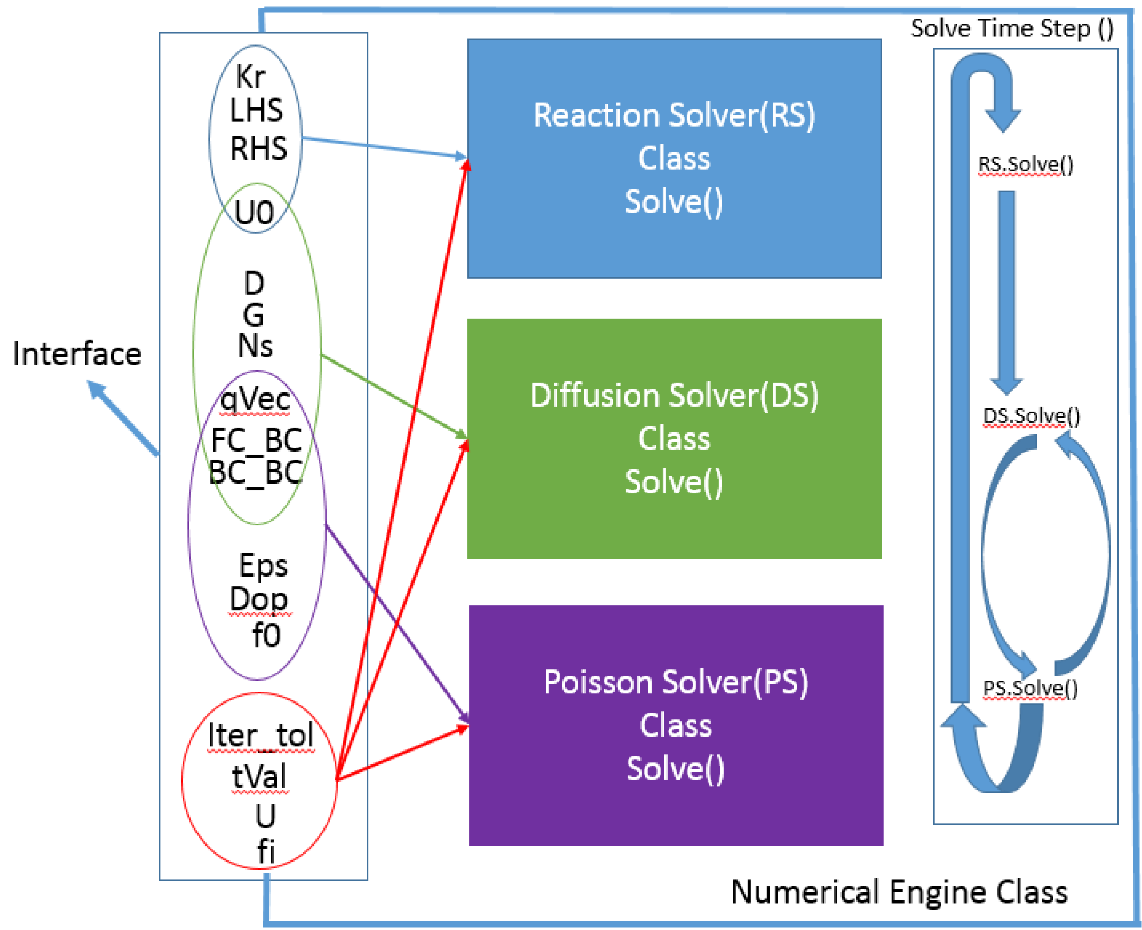

Figure 7. Software Architectural Organization of the Numerical Engine.

Chapter 5

APPLICATION/VALIDATION OF SOLVER

In this section we present 9 simulations which illustrate the validation and application of the developed solver.

5.1 0-D Simulation of Thermally Generated Electrons and Holes

In this simulation, we take reaction (2.28) in CdTe material and run a 0D simulation with initial concentration of electrons and holes as 0, for a total time of 1e25 sec. This simulation shows how fast thermal generation and recombination processes drive the system towards equilibrium. For this simulation we can write the exact analytical expression for the time evolution of the concentrations (see Appendix D):

$$p(t) = n(t) = n_i + \frac{2}{\left(\frac{1}{n_i} + \frac{2}{n(0) - n_i}\right) exp(2K_b n_i t) - \frac{1}{n_i}} \tag{5.1}$$

Here $n_i^2 = \frac{K_f}{K_b}$, K_f, K_b are the forward and backward rates of the reaction (2.28), $n(0) = p(0)$ is the initial electron and hole concentration, and t is the time. The numerical values are given in Table 1. We can compare the numerical solution and analytical solution and this validates the numerical algorithm for the 0D solver. The comparison results are as shown in Fig. 8.

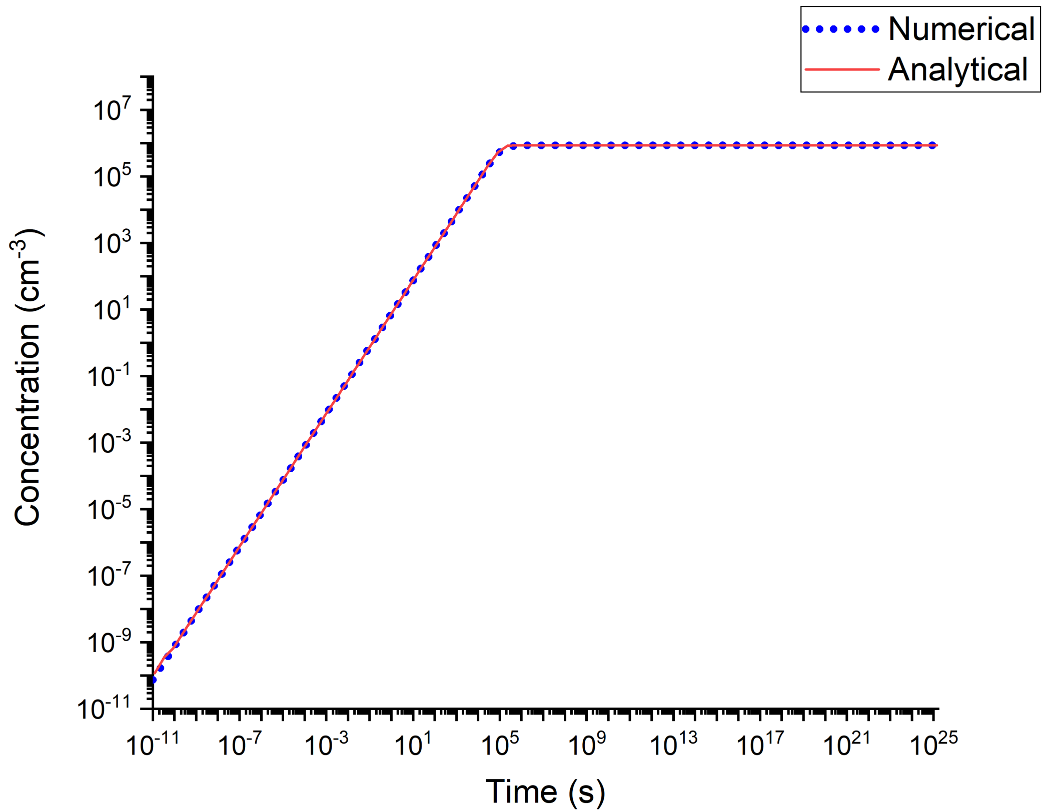

Figure 8. Comparison of Analytical vs Numerical Solution for Time Evolution of Electrons and Holes Generated Thermally.

5.2 0-D Simulation Study of Copper Defects in CdTe

In this study we use the solver to study the thermodynamic limits of Copper defect concentrations in CdTe. The simulation follows the work from Ref. [41] (APL). The authors Yang *et al.*, calculate the formation energies, defect transition levels under different conditions for Cu_i^0, Cu_C^0 and their charge states, and by finding the solution of a constrained equilibrium problem together with charge neutrality condition, they compute the thermodynamic limits of doping concentration of copper defects using

Table 1. Numerical Values Used in the Simulation.

Parameter	**Value**	**Units**
K_f	7.5576	$cm^{-3}s^{-1}$
K_b	1e-11	$cm^{-3}s^{-1}$
n_i^2	7.5576e11	cm^{-6}
$n(0)$	0	cm^{-3}
$p(0)$	0	cm^{-3}

analytical expression. The equations applied in Ref. [41] are

$$\begin{aligned}
[Cu_C^0] &= N_{Cu_C} \times \frac{g_0 e^{-\Delta H_f(Cu_C^0)/kT}}{g_0 e^{-\Delta H_f(Cu_C^0)/kT} + g_{-1} e^{-\Delta H_f(Cu_C^-)/kT}} \\
[Cu_C^-] &= N_{Cu_C} \times \frac{g_{-1} e^{-\Delta H_f(Cu_C^-)/kT}}{g_0 e^{-\Delta H_f(Cu_C^0)/kT} + g_{-1} e^{-\Delta H_f(Cu_C^-)/kT}} \\
[Cu_i^0] &= N_{Cu_i} \times \frac{g_0 e^{-\Delta H_f(Cu_i^0)/kT}}{g_0 e^{-\Delta H_f(Cu_i^0)/kT} + g_{+1} e^{-\Delta H_f(Cu_i^+)/kT}} \\
[Cu_i^+] &= N_{Cu_i} \times \frac{g_{+1} e^{-\Delta H_f(Cu_i^+)/kT}}{g_0 e^{-\Delta H_f(Cu_i^0)/kT} + g_{+1} e^{-\Delta H_f(Cu_i^+)/kT}} \\
[Cu_C^0] &+ [Cu_C^-] + [Cu_i^0] + [Cu_i^+] = N_{Cu_C} + N_{Cu_i} = N_{Cu} \\
[Cu_C^-] &+ [e^-] = [Cu_i^+] + [h^+]
\end{aligned} \tag{5.2}$$

where N_{Cu} is the total copper concentration, N_{Cu_C} is the total copper at cation defect concentration, N_{Cu_i} is the total interstitial copper defect concentration, $[X]$ and $\Delta H_f(X)$ are the concentration and formation enthalpy of the defect species X and g's are the degeneracy factors. With the calculated enthalpies for defects and self consistently solving (5.2), the authors were able to compute the thermodynamic doping limits for the Cu defects in CdTe.

We applied our solver to do the same computation but with the reaction formalism.

The reactions employed to reproduce the results are:

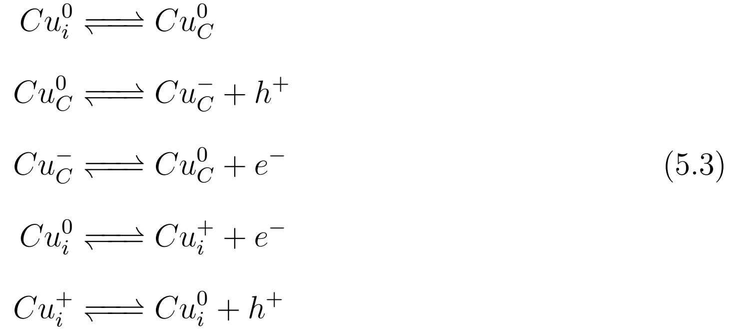

$$
\begin{aligned}
Cu_i^0 &\rightleftharpoons Cu_C^0 \\
Cu_C^0 &\rightleftharpoons Cu_C^- + h^+ \\
Cu_C^- &\rightleftharpoons Cu_C^0 + e^- \\
Cu_i^0 &\rightleftharpoons Cu_i^+ + e^- \\
Cu_i^+ &\rightleftharpoons Cu_i^0 + h^+
\end{aligned}
\tag{5.3}
$$

The formation energies, degeneracies, capture rates are all the same as that of Ref. [41] for the Cd-poor case and we ran a simulation varying total copper concentration from 1e15 to 1e19 cm^{-3}. We got the comparison results as shown in Fig. 9 and Fig. 10.

The slight differences can be accounted for the finite precision arithmetic errors as evident from Fig. 11. Thus, this comparison results show that the reaction formalism assumed in our solver is valid and can reproduce relevant defect chemistry results from the literature. Further discussion of the results can be found in Appendix E

5.3 1D Simulation of Hetero-Junction CdTe Device

In this study we use the solver to study a CdTe based solar cell and compare the results with Silavo simulations. The device structure is shown in Fig. 12. The structure consists of four layer: 0.2um of zinc telluride (ZnTe), 1um of CdTe, 0.4um of cadmium sulphide (CdS), and 0.4um of transparent conducting oxide (TCO). The doping of each layer is as shown in Fig. 12. The ZnTe layer has p-type doping of 1.7e18 cm^{-3}, CdTe has p-type doping of 1e14 cm^{-3}, CdS has n-type doping of 1e16

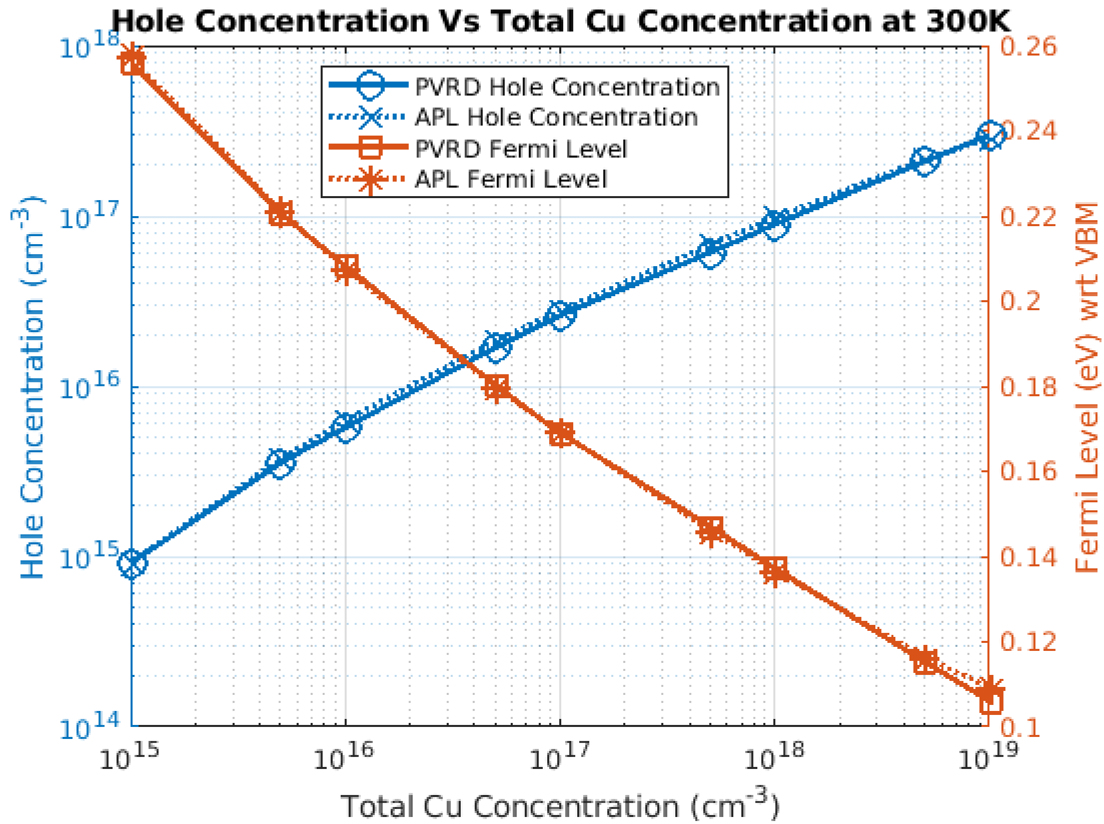

Figure 9. Comparison of Hole Concentrations (Fermi Level) vs Total Cu Concentration.

cm^{-3} and TCO has n-type doping of 1.2e17 cm^{-3}. The bias applied is with respect to TCO at ZnTe. The light is AM1.5G and is illuminated from TCO side.

We built the same structure in Silvaco and our solver using the same material parameters. In our solver we specify the SRH processes and radiative processes through the reactions as given below:

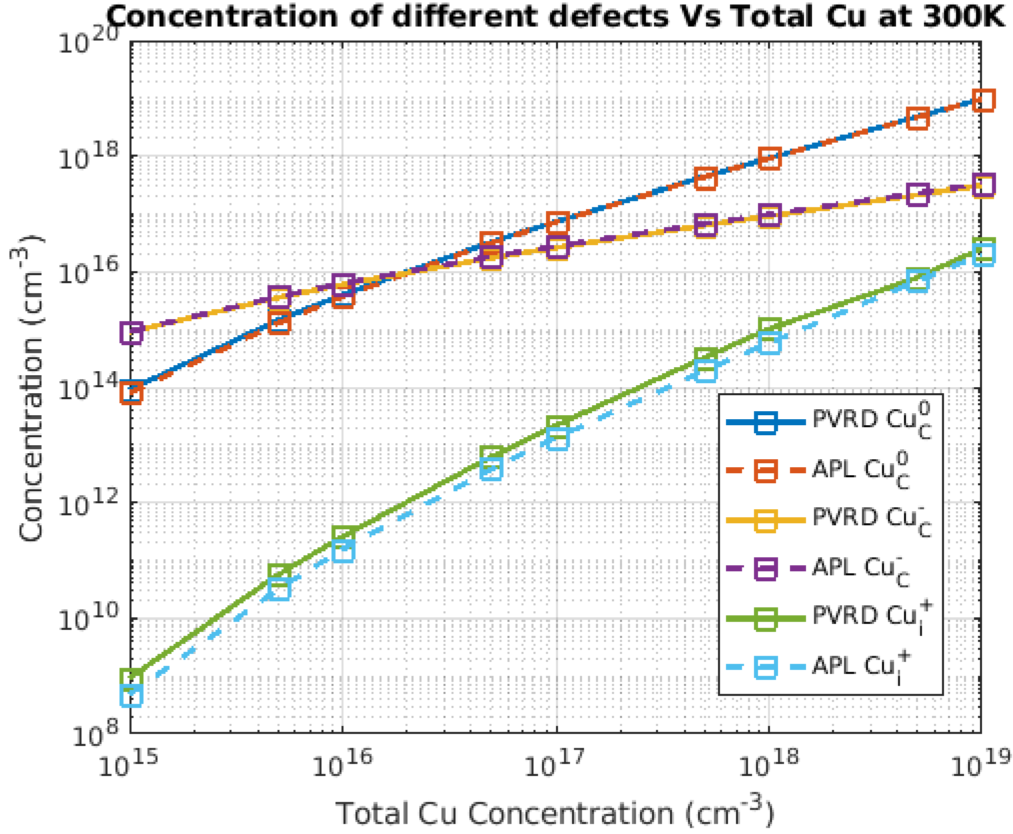

Figure 10. Comparison of Cu Defect Concentrations vs Total Cu Concentration.

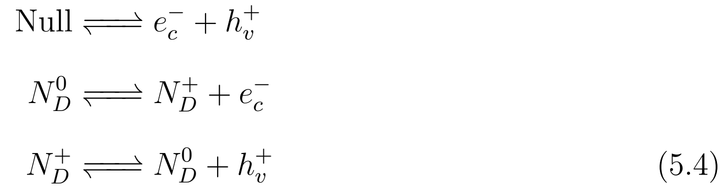

$$\text{Null} \rightleftharpoons e_c^- + h_v^+$$

$$N_D^0 \rightleftharpoons N_D^+ + e_c^-$$

$$N_D^+ \rightleftharpoons N_D^0 + h_v^+ \tag{5.4}$$

$$N_A^0 \rightleftharpoons N_A^- + h_v^+$$

$$N_A^- \rightleftharpoons N_A^0 + e_c^-$$

(5.5)

The donor dopant (N_D) are in CdS and TCO and acceptor dopant (N_A) are present in ZnTe and CdTe layers with the concentration described.

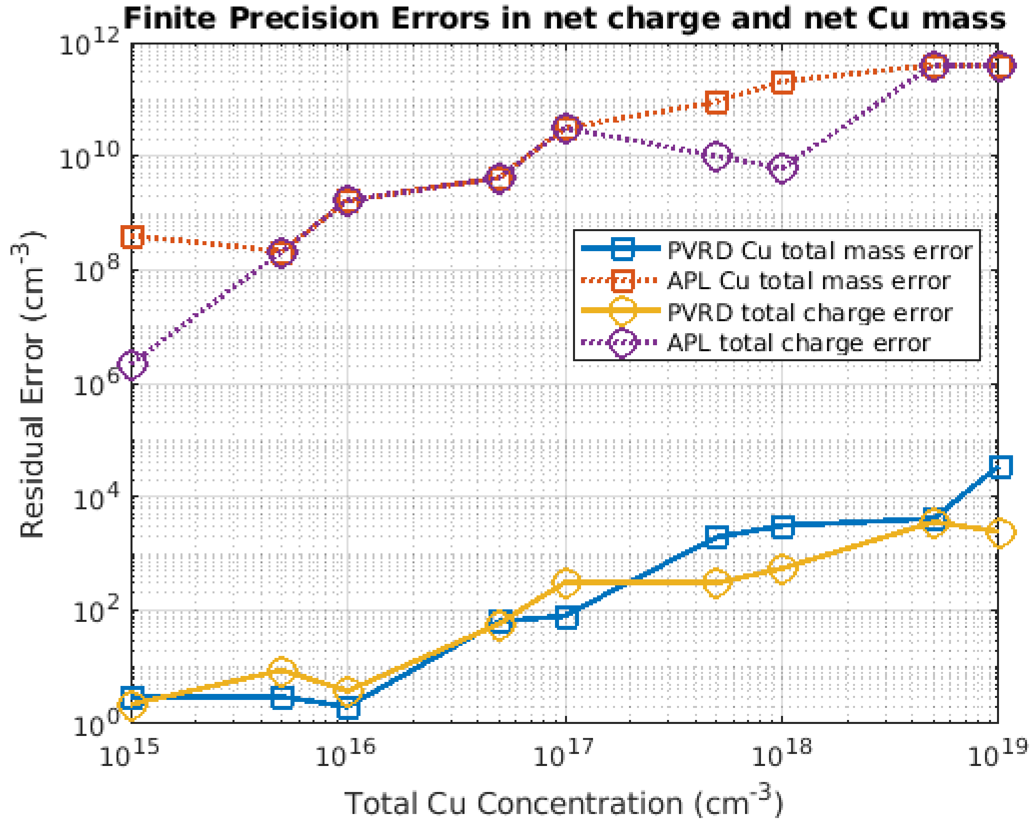

Figure 11. Comparison of Total Mass and Charge Errors vs Total Cu Concentration.

The capture rates and all material parameters are kept same for both our simulation and Silvaco simulation. We computed the JV curves and compared them, as shown in Fig. 13, with Silvaco simulations of an identical structure. We see that we have achieved very close match in short circuit current between our simulation (27.26 mA/cm^2) and that of Silvaco simulation (27.01 mA/cm^2). The open circuit voltage in our simulation is very close to 0.86V where as that of Silvaco simulation is around 0.86V. This comparison further validates our formalism and methodology to study point defects and charge carriers on equal footing and the treatment of SRH process as a defect chemical reaction.

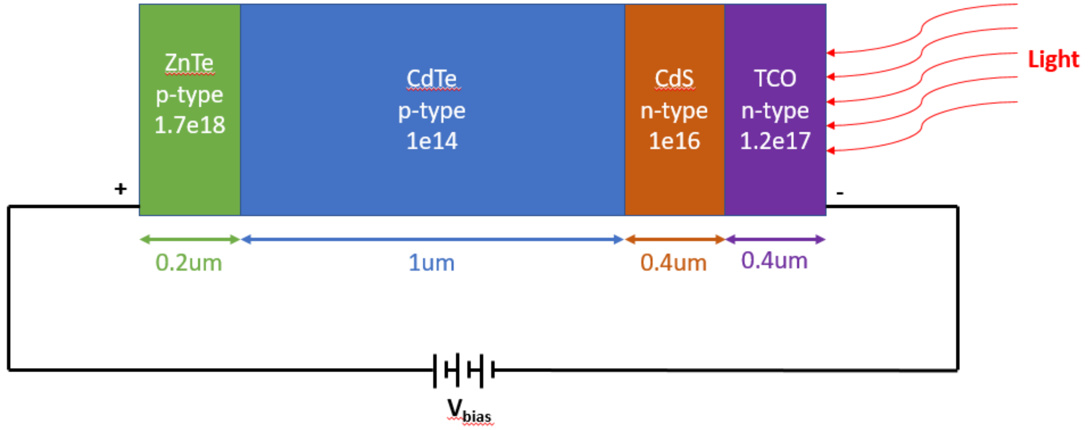

Figure 12. Schematics of Heterojunction CdTe Device Simulation.

5.4 1-D Simulation of Cu Diffusion in Single Crystal CdTe

In this study we perform copper diffusion simulation in single crystal CdTe and compare it with the experimentally measured Cu SIMS data as given in Ref. [39]. We perform the numerical simulation with four different annealing recipes namely 3min anneal at 350°C, 6min anneal at 350°C, 10min anneal at 300°C and 20min anneal at 300°C. The simulation structure consists of a 0.5um ZnTe layer doped with Cu and an acceptor concentration of 1e19 cm^{-3} and 19.5um of sX-CdTe layer. The Cu species present in ZnTe are assumed to form a neutral complex $[Cu_C - Cu_i]^0$ with concentration of 2.5e20 cm^{-3}. Previous simulations done by Da Guo *et al.* [39], assumed an effective model in the ZnTe layer that maintains an acceptor doping of 1e19 cm^{-3}. The current solver does not need the effective model and the Cu complex is close to the real structure of the Cu:ZnTe layer. The reactions considered for this study are given in Table 2.

The reaction 1 in ZnTe layer is the complex dissociation of $[Cu_iCu_C]^0$, reaction

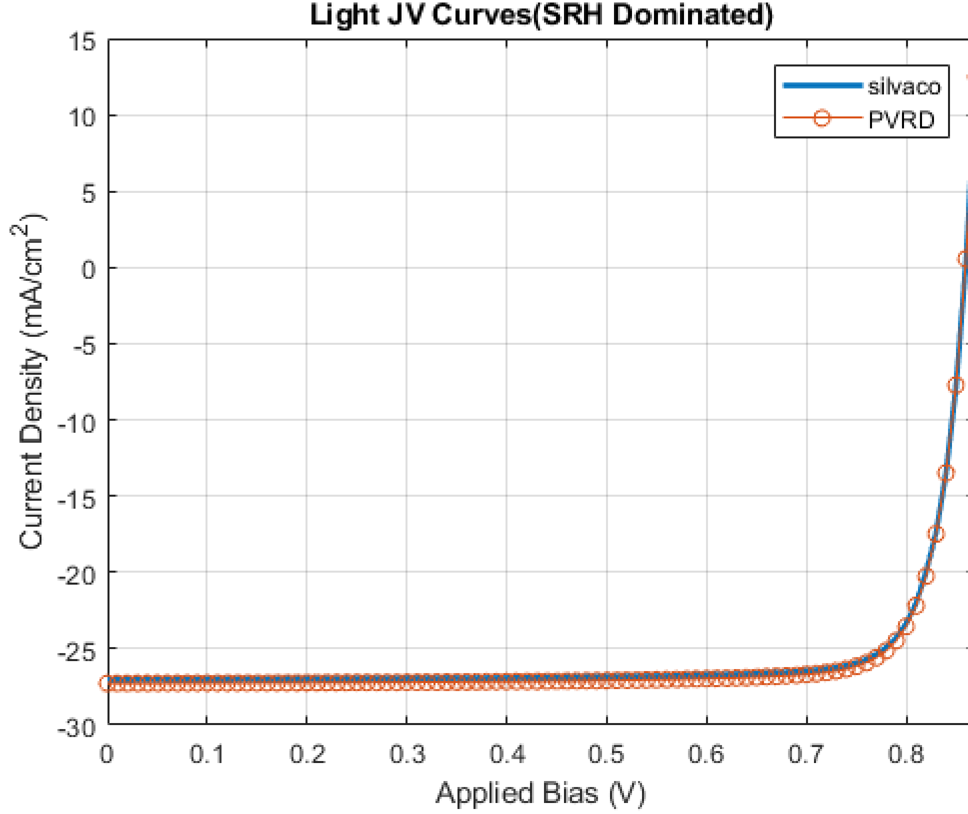

Figure 13. Comparison of JV Curves for CdTe Solar Cell Simulation.

2 is the radiative generation recombination and reaction 3 and 4 are the hole and electron capture reactions by the acceptor defect. Similarly in CdTe we have reaction 1 as complex dissociation of $[Cu_iCu_C]^0$, reaction 2 as radiative generation and recombination of free carriers, reaction 3, 4 represent the copper knock-off reaction which is the main reaction involved in the Cu acceptor formation in CdTe and other reactions are the electron and hole capture reactions of the invovled defects resulting form the knock-off reaction and dissociation reaction. The first principle numbers are taken from Ref. [32, 42, 43]. Since first principle parameters are not available in ZnTe, we assumed similar numbers as that of CdTe. We varied the formation energies in ZnTe and CdTe for Cd_i defect and $[Cu_iCu_C]^0$ complex formation energies in ZnTe

Table 2. Reactions Considered in the Cu Diffusion in sX CdTe Simulation.

Rx No.	**Rx in ZnTe Layer**	**Rx in CdTe Layer**
1	$[Cu_iCu_C]^0 \rightleftharpoons Cu_i^+ + Cu_C^-$	$[Cu_iCu_C]^0 \rightleftharpoons Cu_i^+ + Cu_C^-$
2	Null $\rightleftharpoons e^- + h^+$	Null $\rightleftharpoons e^- + h^+$
3	$N_A^0 \rightleftharpoons N_A^- + h^+$	$Cu_i^+ + Cd_C^0 \rightleftharpoons [Cu_iCd_C]^+$
4	$N_A^- \rightleftharpoons N_A^0 + e^-$	$[Cu_iCd_C]^+ \rightleftharpoons Cu_C^- + Cd_i^{2+}$
5		$Cu_i^+ \rightleftharpoons Cu_i^0 + h^+$
6		$Cu_i^0 \rightleftharpoons Cu_i^+ + e^-$
7		$Cu_C^0 \rightleftharpoons Cu_C^- + h^+$
8		$Cu_C^- \rightleftharpoons Cu_C^0 + e^-$
9		$Cd_i^{2+} \rightleftharpoons Cd_i^+ + h^+$
10		$Cd_i^+ \rightleftharpoons Cd_i^{2+} + e^-$
11		$Cd_i^+ \rightleftharpoons Cd_i^0 + h^+$
12		$Cd_i^0 \rightleftharpoons Cd_i^+ + e^-$

to match the experimental SIMS data. Our simulation shows that we need not vary the diffusion barriers from DFT calculation as was done in Ref [39].

Comparison of measured copper profiles and numerical simulations for samples prepared by 350°C 3min anneal recipe, 350°C 6min anneal recipe, 300°C 10min anneal recipe and 300°C 20min anneal recipe are shown in Fig. 14, Fig. 15, Fig. 16 and Fig. 17 respectively. We see that our simulation result closely matches the experimentally

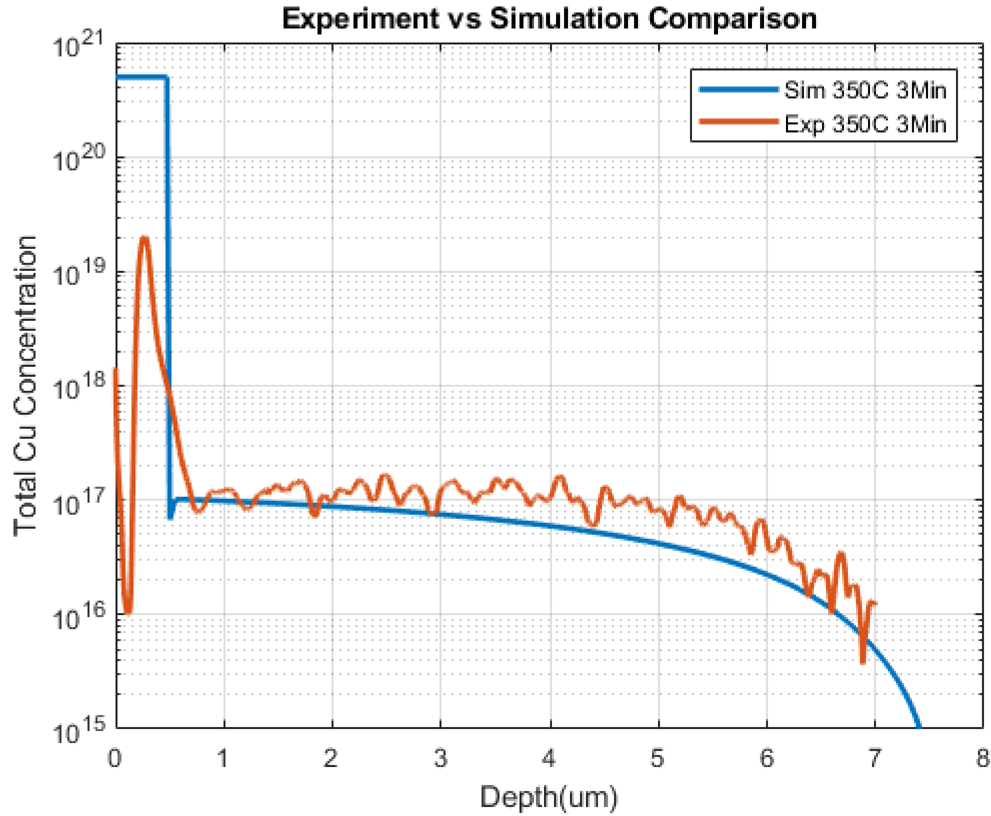

Figure 14. Copper Profile Comparison for 3min 350°C Anneal Recipe.

measured profiles in the CdTe layer. The measurements near the start of ZnTe layer show a decrease in Cu concnetration which can be attributed as an artifact of SIMS measurement. The numerical simulation results are not taken after the cool down to room temperature although the measurements are taken at room temperature. Simulations of cool down process is still in progress, however we do not expect the resulting Cu profiles to change significantly from those presentd in Fig. 14 to Fig. 17. The DFT parameters used for this simulation are documented in Appendix F

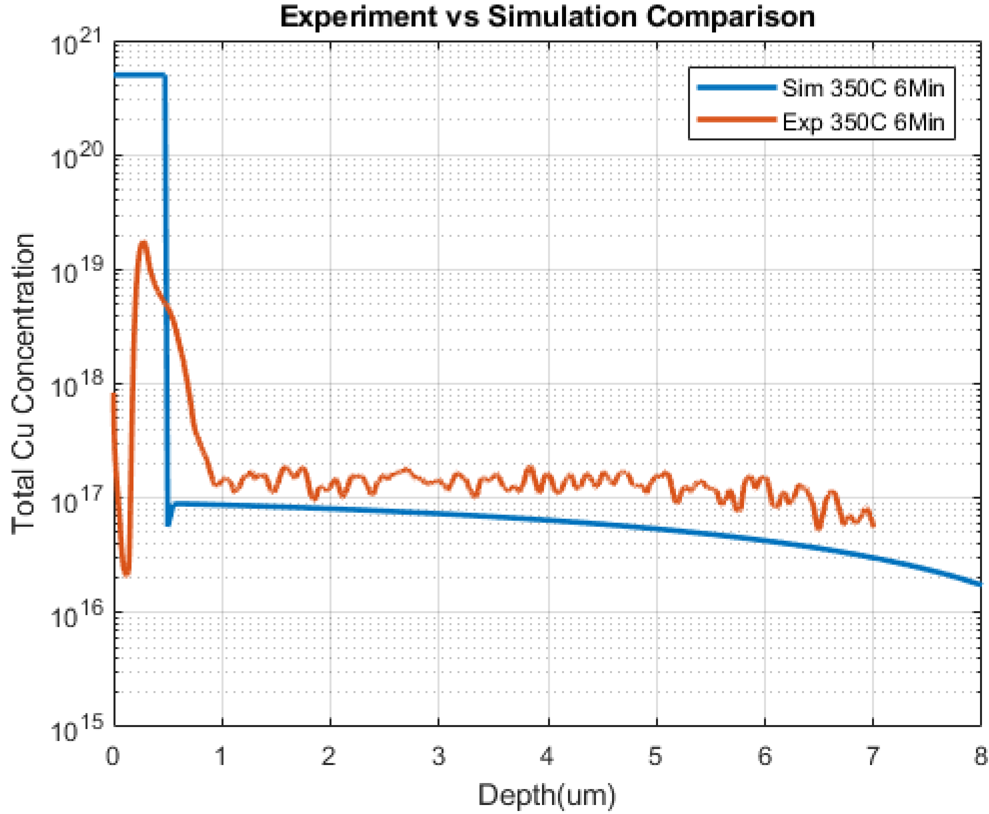

Figure 15. Copper Profile Comparison for 6min 350°C Anneal Recipe.

5.5 1D Simulation of Cu Diffusion in Full Stack CdTe Device

In this simulation, we build a full stack CdTe device structure similar to the structure shown in Fig. 12, introduce Cu complexes in ZnTe layer, perform thermal annealing at 350°C for 3min and cool down to room temperature numerical simulation and finally extract the device characteristics in terms of light JV curves. The full stack CdTe device structure dimensions are given in Table 3

The defect chemical reactions considered in ZnTe and CdTe are exactly the same as the reactions considered in Table 2. The reactions considered in CdS and TCO are the donor ionization reactions and radiative recombination reactions (i.e., sub

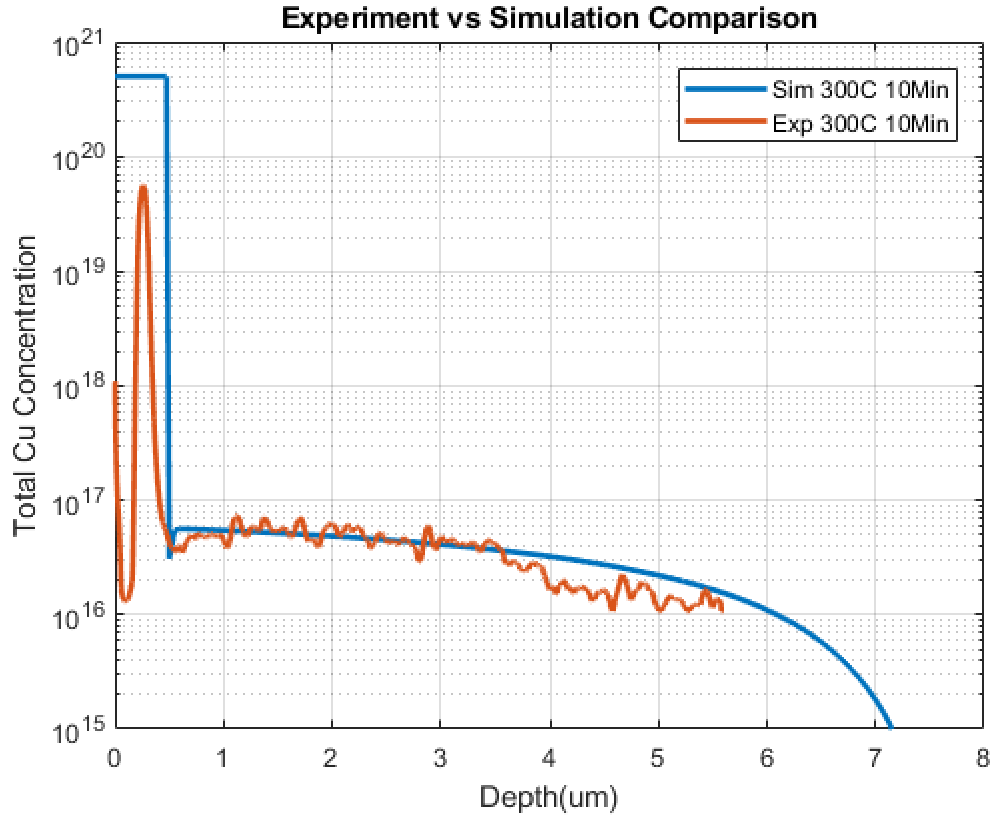

Figure 16. Copper Profile Comparison for 10min 300^oC Anneal Recipe.

Table 3. Full Stack CdTe Device Structure.

Layer Name	**Width (um)**
ZnTe	0.5
CdTe	3
CdS	0.04
TCO	0.46
Total	**4**

reactions 1,2,3 from reactions (5.4)). The point defects considered in this simulation are the ones given in the reactions in each layer. The initial conditions of point defects are all set to one except for the point defect initial concentration listed in Table 21. The DFT parameters used in this simulation is as given in Appendix F.

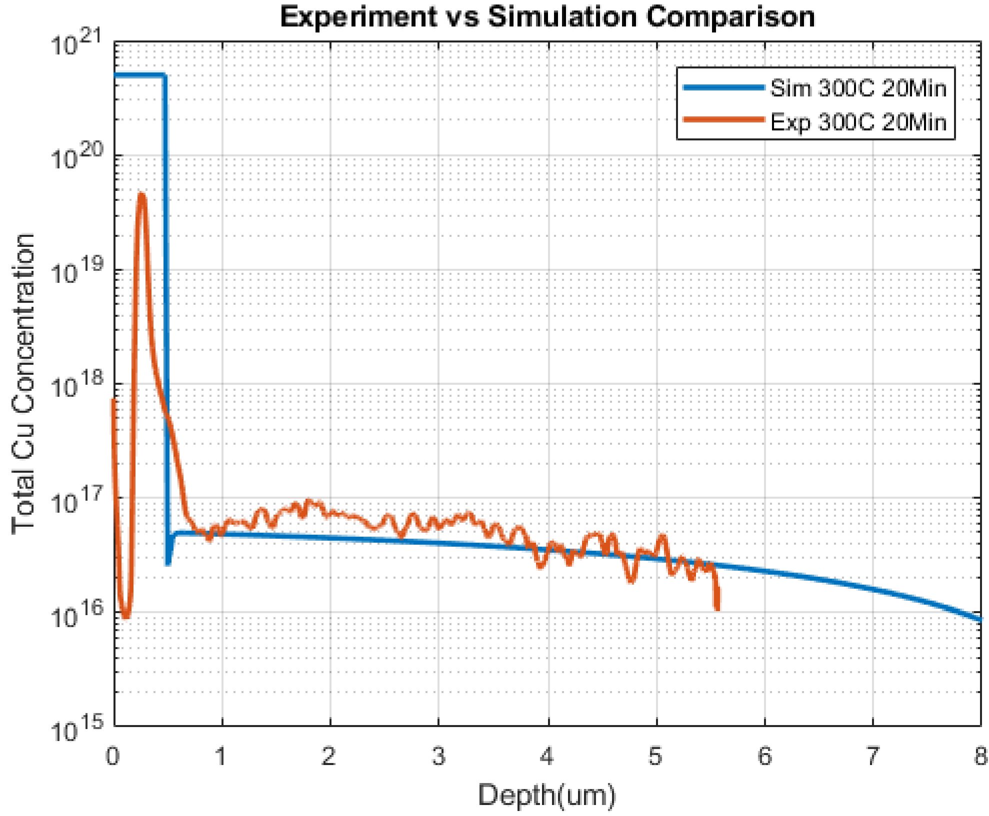

Figure 17. Copper Profile Comparison for 20min 300^oC Anneal Recipe.

Table 4. Initial Concentrations Used for the Simulation.

Species	**ZnTe** (cm^{-3})	**CdTe** (cm^{-3})	**CdS** (cm^{-3})	**TCO** (cm^{-3})
N_A^0	1e19	1	1	1
$[Cu_iCu_C]^0$	2.5e20	1	1	1
N_D^0	1	1	1e16	1e18

The temperature profile for the thermal activation process is as shown in Fig. 18. This profile mimics a general temperature profile of thermal annealing and the cooling is modeled with Newton cooling with cooling rate of 0.01 per sec.

The boundary conditions for this simulation until cool down were set to zero

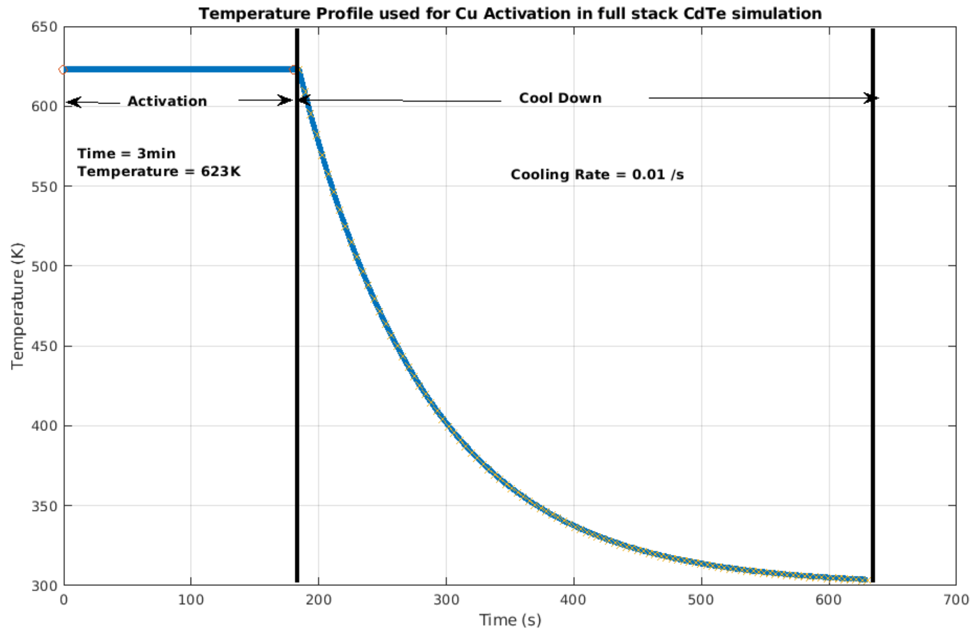

Figure 18. Temperature Profile Used for CdTe Full Stack Cu Simulation.

field and zero flux conditions (insulating boundary condition). The details about the distribution of point defect concentration profiles, band diagrams etc are given in Appendix G. After that a bias was applied under AM1.5G light illumination to characterize the structure for JV curves. Note that the simulation is performed as a transient simulation and thus the applied voltage is ramping up in time under light illumination. The resulting light JV curve is as shown in Fig. 19

We next performed a numerical experiment characterizing JV curves to analyze the sensitivity of free carrier capture reactions in the CdTe layer. We decreased the capture cross section by a factor of 100 (i.e., increasing life time of the carrier by a factor of 100) and performed JV light characterization. It was found that the reaction 5 of Table 2 (hole capture reaction of Cu_i point defect in CdTe is limiting

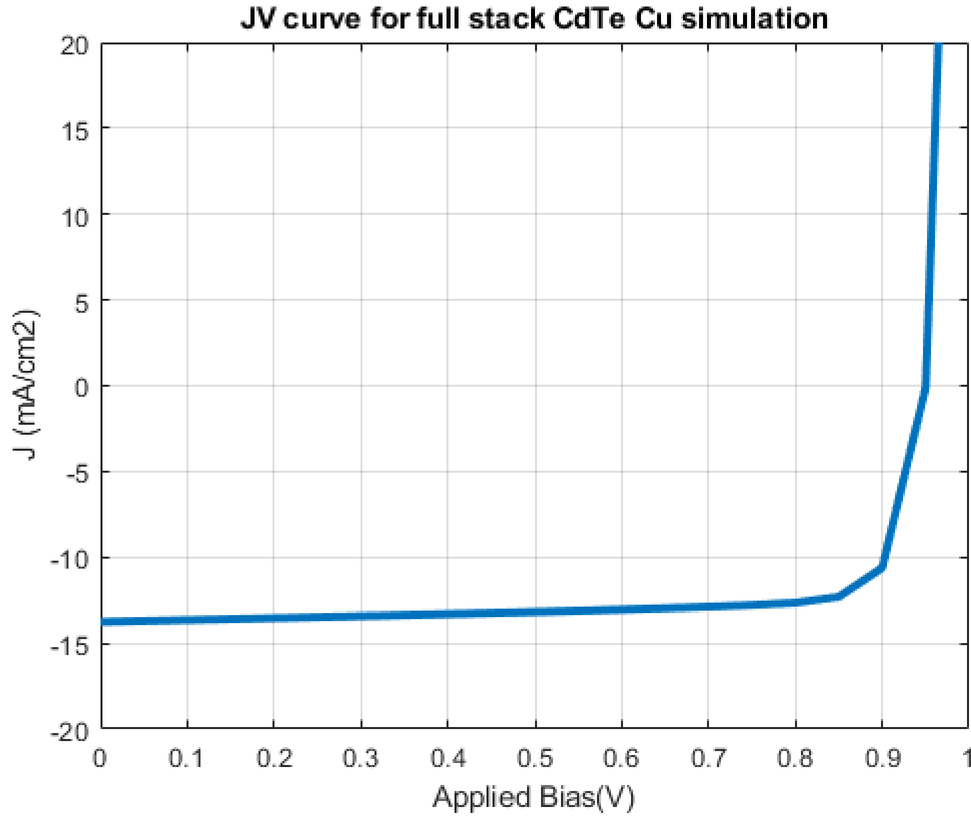

Figure 19. JV Curve After Cool Down to 300K.

the performance of the CdTe solar considered in our simulation. The J_{sc} and V_{oc} for this sensitivity analysis is as shown in Table 5 and Fig. 20.

In this simulation, we clearly demonstrate the application of the PVRD-FASP tool. We were able to do a process simulation mimicking the thermal annealing and perform device characterization using the same complex level of modeling for point defects and charge carrier. This level of complex analysis for point defects as well as charge carriers is not available in any of the state of the art TCAD tools available in the scientific community. This is the main contribution of our work that differentiates from the rest of the available TCAD tools. We also note that we can perform accelerated life test

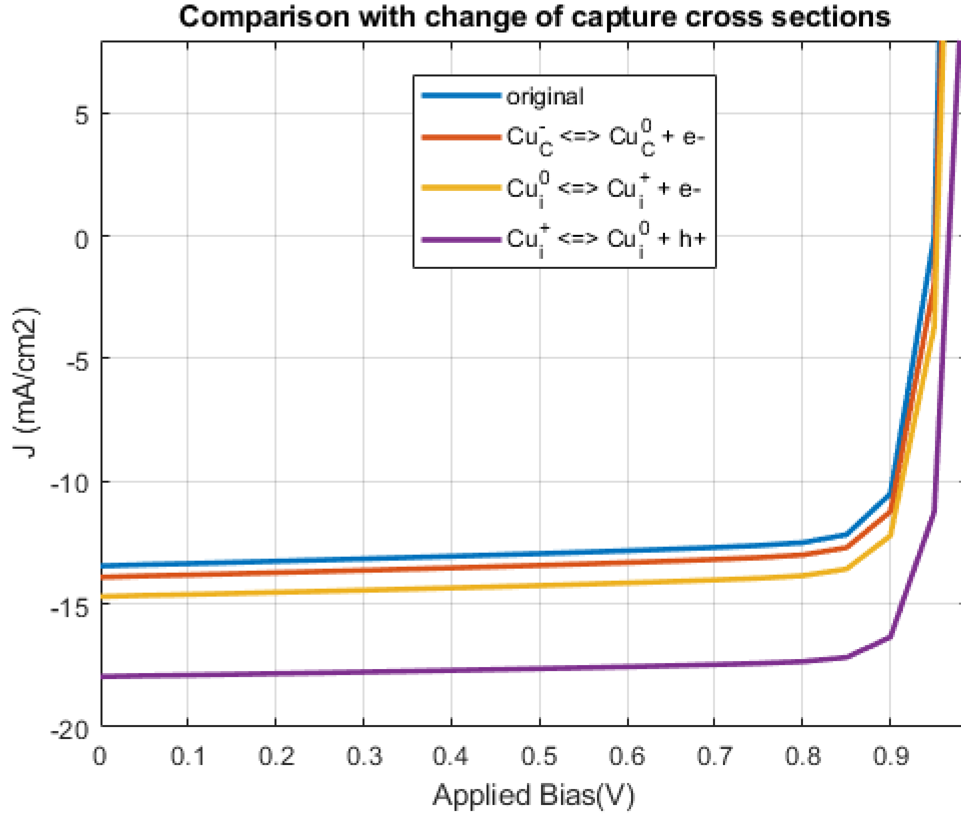

Figure 20. JV Curves for Sensitivity Analysis.

simulations as well with the solver or long term simulation in decades scale although there is a limitation present because of the finite precision arithmetic and conditioning of the involved matrix. We are still actively trying to understand these limitations and proposing new algorithms to avoid these issues.

5.6 Efforts on Understanding of Chloride Treatment

In this section we provide our efforts on understanding the effects of chloride treatment using our developed tool. To understand the nature of chlorine point defects in the CdTe system first we need to understand how chlorine point defects evolve from

Table 5. Full Stack CdTe Device Structure.

Reaction Name	J_{sc} $(\text{mA/cm})^2$	V_{oc} (V)
$Cu_i^+ \rightleftharpoons Cu_i^0 + h^+$	17.96	0.97
$Cu_i^0 \rightleftharpoons Cu_i^+ + e^-$	14.71	0.95
$Cu_C^0 \rightleftharpoons Cu_C^- + h^+$	13.47	0.95
$Cu_C^- \rightleftharpoons Cu_C^0 + e^-$	13.93	0.95
$Cd_i^{2+} \rightleftharpoons Cd_i^+ + h^+$	13.47	0.95
$Cd_i^+ \rightleftharpoons Cd_i^{2+} + e^-$	13.47	0.95
$Cd_i^+ \rightleftharpoons Cd_i^0 + h^+$	13.47	0.95
$Cd_i^0 \rightleftharpoons Cd_i^+ + e^-$	13.47	0.95

start of its incorporation, its interaction with the intrisic point defects and the defect chemistry in the grain boundaries. We first tried to address how initial conditions should be chosen for the intrinsic point defects.

Suppose we grow intrinsic CdTe under Cd rich condition or Te rich condition. Then, what should be the concentration of intrinsic point defects in CdTe? Our formulation gives same thermodynamic Gibb's free energy for balanced point defect chemical reactions independent of growth conditions even though the formation energy of each point defect gets shifted with growth conditions. Also, we are setting the same reaction model with same capture cross sections for different growth conditions. Hence the equilibrium ratios of the concentration should be the same independent of the growth conditions, thus leading to paradoxical conclusion that, if the initial concentrations of point defects in CdTe is same under different growth condition, then

the final concentration of point defects should be same. This is due to the fact that we are writing the same stiff ode equations under different growth conditions and thus should lead to the same final conditions if the initial conditions are same.

Table 6. Unbalanced Chemical Reactions Considered for Growth Simulations.

Null $\rightleftharpoons V_C^0$	Null $\rightleftharpoons Te_i^0$	Null $\rightleftharpoons Cd_i^0$
Null $\rightleftharpoons V_A^0$	Null $\rightleftharpoons Te_C^0$	Null $\rightleftharpoons Te_A^0$
Null $\rightleftharpoons Cd_C^0$	Null $\rightleftharpoons Cd_A^0$	Null $\rightleftharpoons [Te_i - Te_i]^0$
Null $\rightleftharpoons [Te_i - Te_C]^0$	Null $\rightleftharpoons [Te_C - Te_C]^0$	Null $\rightleftharpoons [V_C - Te_C]^0$

But in actual experiments we see different final conditions under different growth conditions. To mimic the growth conditions leading to different final conditions we introduce unbalanced point defect chemical reactions as given in Table. 6 and these reactions model the kinetics between the chemical reservoir and the CdTe growth substrate. This is similar to the approach used in [41]. We write the unbalanced point defect chemical reactions only for neutral point defects as charged point defect will involve charge imbalance for the growth substrate thus leading to numerical instability. Using this theory we calculated the thermodynamic equilibrium concentrations of intrinsic point defects grown at 300K, 800K and 1200K including defect complexes under 3 different growth conditions namely $\mu_{Cd} = 0$, $\mu_{Cd} = -0.75$ and $\mu_{Cd} = -1.17$. The higher temperature growth is quenched down to room temperature rapidly. During quenching the unbalanced chemical reactions are removed from the simulation. Also, we considered all the ionization reactions of the considered point defects.

The documented values after cooling down to room temperature with concentra-

Table 7. Dominant Point Defect in CdTe for Different Growth Conditions at 300K.

Defect Name	$\mu_{Cd} = 0$ cm^{-3}	$\mu_{Cd} = -0.75$ cm^{-3}	$\mu_{Cd} = -1.17$ cm^{-3}
e_c^-	1.26e8	8.70e5	-
h_v^+	-	8.78e5	1.25e6
V_A^{2+}	6.14e7	-	-
Cd_A^{2+}	1.96e6	-	-
V_C^{2-}	-	-	3.33e5

tions of the point defects above 1e6 cm^{-3} (intrinsic concentration at 300K) are given in Table 7-9. From the table it is evident that at higher temperature growths, the concentration and the types of intrinsic point defects both increase.

Also after quenching from high temperature to room temperature, the formation of defect complexes is evident. Cd-rich ($\mu_{Cd} = 0$) conditions under any temperature growth has resulted in n-type nature, moderately Cd-poor ($\mu_{Cd} = -0.75$) and Cd-poor resulted in intrinsic behavior at 300K and p-type nature at higher temperatures. At 300K growth V_A^{2+} is the dominant donor defect under Cd-rich conditions whereas V_C^{2-} is the dominant acceptor defect under Cd-poor (Te-rich) conditions. For moderately Cd-poor conditions at 300K we observe intrinsic behavior. For 800K temperature growth, under Cd-rich conditions Cd_A^{2+}, V_A^{2+} are the dominant donor defects. V_C^{2-} is dominant acceptor defect under moderately Cd-rich conditions and Cd-poor conditions. We also observe the formation of complex defects under Cd-poor conditions during the cool down from 800K to 300K.

When the growth temperature is further increased to 1200K we note an increase in point defects. In Cd-rich conditions we have Cd_A^{2+} as dominant donor. For moderately Cd-poor condition V_C^{2-} acceptor and V_A^{2+} donor are dominant. In Cd-poor

Table 8. Dominant Point Defect in CdTe for Different Growth Conditions at 800K and Rapidly Cool Down to 300K.

Defect Name	$\mu_{Cd} = 0$ cm^{-3}	$\mu_{Cd} = -0.75$ cm^{-3}	$\mu_{Cd} = -1.17$ cm^{-3}
e_c^-	2.01e14	-	-
h_v^+	-	5.10e12	4.49e13
V_C^{2-}	-	2.94e13	2.88e14
V_C^-	-	1.74e11	1.50e13
V_C^0	-	2.37e12	1.79e15
Cd_A^{2+}	1.51e14	-	-
Cd_i^0	1.98e12	-	-
Cd_i^+	3.82e10	-	-
Cd_i^{2+}	1.69e12	-	-
V_A^-	1.23e12	-	-
V_A^0	2.60e15	-	-
V_A^+	1.54e12	-	-
V_A^{2+}	1.00e14	6.39e11	-
Te_i^{2+}	-	-	4.84e10
Te_C^{2+}	-	-	2.28e13
$[Te_i - Te_C]^0$	-	-	2.18e12
$[Te_i - Te_C]^+$	-	-	8.03e10
$[Te_i - Te_C]^{2+}$	-	-	6.77e12
$[Te_i - Te_C]^{3+}$	-	-	3.60e10

conditions V_C^{2-} is the dominant acceptor and Te_C^{2+} is the dominant donor followed by $[Te_i - Te_C]^{2+}$. Here we see a strong compensation lowering the hole concentration.

From the concentrations we observe that mass and charge conservation is obeyed for 300K but not at 800K and 1200K temperatures. We note that we implemented this unbalanced chemical reactions feature in our PyCDTS code rather in PVRD-FASP code. PyCDTS codes does not support mass and charge conservation correction

Table 9. Dominant Point Defect in CdTe for Different Growth Conditions at 1200K and Rapidly Cool Down to 300K.

Defect Name	$\mu_{Cd} = 0$ cm^{-3}	$\mu_{Cd} = -0.75$ cm^{-3}	$\mu_{Cd} = -1.17$ cm^{-3}
e_c^-	8.07e15	-	-
h_v^+	-	1.25e14	4.43e13
V_C^{2-}	5.65e13	4.33e14	2.92e16
V_C^-	-	6.30e13	1.50e15
V_C^0	-	2.10e16	1.77e17
Cd_A^+	2.91e10	-	-
Cd_A^{2+}	5.17e15	-	-
Cd_i^0	1.08e15	-	-
Cd_i^+	5.19e11	-	-
Cd_i^{2+}	5.71e11	2.64e12	2.65e11
V_A^{2-}	2.39e13	-	-
V_A^-	1.86e15	-	-
V_A^0	9.77e16	-	-
V_A^+	1.44e12	-	-
V_A^{2+}	2.34e12	2.38e14	2.38e13
Te_i^+	-	-	2.21e10
Te_i^{2+}	-	5.69e12	3.41e14
Te_C^0	-	-	1.02e11
Te_C^+	-	-	9.76e11
Te_C^{2+}	-	6.46e12	2.13e16
$[Te_i - Te_C]^0$	-	-	2.65e15
$[Te_i - Te_C]^+$	-	-	9.62e13
$[Te_i - Te_C]^{2+}$	-	5.16e10	8.01e15
$[Te_i - Te_C]^{3+}$	-	-	4.21e13
$[Te_C - Te_C]^{2+}$	-	-	1.22e10
$[V_C - Te_C]^0$	-	-	8.23e11

scheme as of 0.2.0 release version and thus we could not show an accurate simulation results. This will be corrected in future versions of PyCDTS and we will redo the above simulation experiment.

The formation energies of the defects we have considered in our CdTe material database is as given in the Table 10 and Table 11.

Table 10. Donor Type Point Defect for CdTe Material System Considered in PyCDTS (Cd Rich Conditions).

Name	**G0** eV	$\mathbf{E}_{0/+}$ eV	$\mathbf{E}_{+/2+}$ eV	$\mathbf{E}_{2+/3+}$ eV	$\mathbf{E}_{3+/4+}$ eV	Ref Paper
Cd_A	2.299	1.500	1.700	-	-	[32]
Cd_i	2.032	1.190	1.390	-	-	[32]
Te_i	2.993	0.385	1.390	-	-	[32]
$[Te_i - Te_i]$	6.426	1.520	1.360	0.200	0.150	[43]
$[Te_i - Te_C]$	4.972	0.250	0.450	0.200	0.080	[43]
$[Te_C - Te_C]$	8.018	1.059	1.259	0.014	0.214	[43]
Cl_A	1.438	1.285	-	-	-	[32]
$[Te_C - Cl_A]$	3.952	1.500	0.094	0.294	-	[43]
$[Cd_i - Cl_i]$	4.852	1.500	1.230	1.430	-	[43]
Cu_i	1.936	1.336	-	-	-	[32]
$[Cu_i - Cu_C]$	2.116	0.184	-	-	-	[43]
$[Cu_i - Te_C]$	5.269	1.500	0.084	0.284	-	[43]
$[Cu_i - Te_i]$	4.623	1.500	0.205	0.405	-	[43]
$[Cd_i - Cu_C]$	3.954	1.600	1.500	-	-	[43]
$[Cu_i - Cl_i]$	3.380	0.764	0.964	-	-	[43]

All the formation energies and transition levels are extracted from the reference papers given in their respective last columns. In some point defect cases only $E_{0/2+}$ are provided. We extrapolate the transition levels of $E_{0/+}$ and $E_{+/2+}$ to 0.1 eV from $E_{0/2+}$.

Table 11. Acceptor/Amphoteric Type Point Defect for CdTe Material System Considered in PyCDTS (Cd Rich Conditions).

Name	**G0** eV	$\mathbf{E}_{2-/-}$ eV	$\mathbf{E}_{-/0}$ eV	$\mathbf{E}_{0/+}$ eV	$\mathbf{E}_{+/2+}$ eV	$\mathbf{E}_{2+/3+}$ eV	Ref Paper
V_C	3.013	0.259	0.459	-	-	-	[32]
V_A	1.510	1.500	1.490	1.100	1.400	-	[44]
Te_C	3.739	1.151	1.351	0.394	0.594	-	[45]
$[V_C - Te_C]$	6.013	0.794	0.994	-	-	-	[43]
$Cl_i]$	2.658	-	0.162	1.277	-	-	[32]
$[Cl_i - Cl_i]$	3.381	1.010	1.210	0.569	0.769	-	[43]
$[Cl_i - Te_C]$	5.052	-	1.300	1.500	0.170	0.130	[43]
$[Cl_i - Cl_A]$	1.953	-	1.260	0.110	-	-	[43]
$[V_C - Cl_A]$	3.145	-	0.000	-	-	-	[43]
$[Te_i - Cl_i]$	5.403	-	-0.170	0.07	1.095	1.295	[43]
$Cu_C]$	1.732	-	0.154	-	-	-	[32]
$[Cl_i - Cu_C]$	2.617	-	1.300	0.485	0.685	-	[43]
$[Te_i - Cu_C]$	3.679	-	0.880	1.080	0.100	0.300	[43]
$[Cl_A - Cu_C]$	1.519	-	1.230	0.130	-	-	[43]
$[Cu_C - Te_C]$	4.751	-	0.834	0.854	0.094	-	[43]
$[Cu_C - Cu_C]$	3.234	0.304	0.164	-	-	-	[43]

For example, in Ref. [32] Cd_i defect has $E_{0/2+}$ given as 1.290 eV. The respective $E_{0/+}$ level is taken as $E_{0/2+} - 0.1 = 1.190eV$ and $E_{0/2+} + 0.1 = 1.390eV$ for $E_{+/2+}$. We note that $E_{0/2+}$ should be a mid value of $E_{0/+}$ and $E_{+/2+}$ and these transition states form unstable point defect structures resulting in higher energy configuration. In a similar way we can extrapolate the transition levels for acceptor type point defects as well. We note that the choice of 0.1eV extrapolation is arbitrary and it should be avoided if the transition level information for the point defect is available.

We next introduced this as initial conditions for performing chlorine incorporation simulation. For this we started with vertical grain boundary structure as discussed

in section 5.7. Since we do not know much about the grain boundary chemistry and chemical nature of chlorine at the surface of the CdTe we are limited with adding many diligent assumptions about defect chemistry and this still requires considerable effort to complete the simulation. Thus, we stopped our efforts here and proceeded to understand a generic CdTe test case without diving into the origins of the chloride treatment formation.

5.7 Effects of Traps and Recombination Centers in Grain Boundaries

In this section we analyze the effects of traps and recombination centers in grain boundary of a test CdTe structure with vertical grain boundary as shown in Fig. 21. We first describe phenomena of trapping and recombination at point defects and what we call as ideal trapping centers and ideal recombination centers.

Consider the electronic processes occurring at a point defect as shown in Fig. 22. The point defect can capture an electron and remit the electron back to its original state. This kind of processes are called ideal electron trapping. The same thing can be shown for ideal hole trapping as Fig. 23. The ideal recombination center behavior occurs when an electron (or hole) is first captured and then the process is followed by a capture of opposite polarity carrier i.e. hole (or electron) as shown in Fig. 24. Hence, a capture of carrier involves a change in the charge state of point defect. If the charge state is positive we say the point defect behaves as a donor type and if it is negative then it is an acceptor type. Thus an ideal acceptor type electron trap can be written as

$$T_{g,a}^{-} \rightleftharpoons T_{g,a}^{0} + e^{-} \tag{5.6}$$

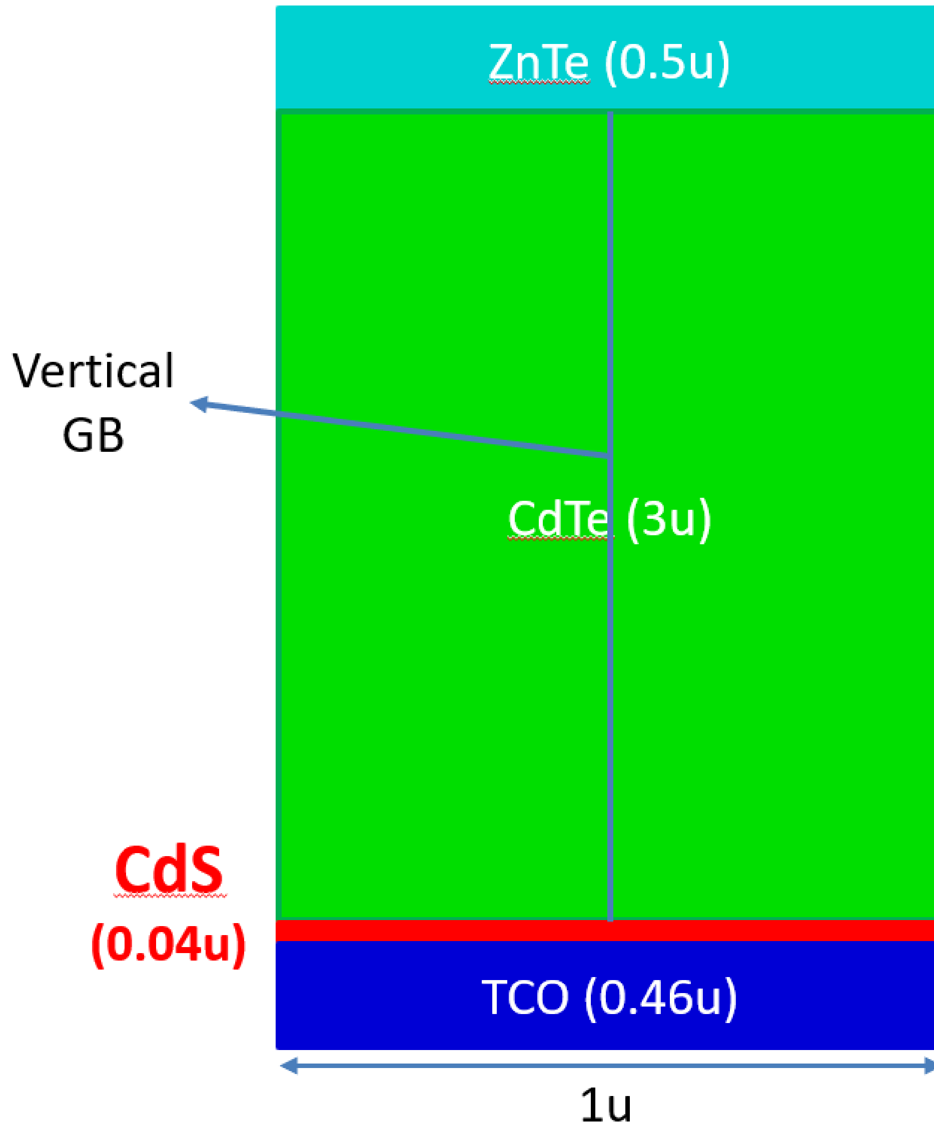

Figure 21. CdTe Device Structure with Vertical Grain Boundary.

Similarly an ideal acceptor type hole trap can be written as

$$T^0_{g,a} \rightleftharpoons T^-_{g,a} + h^+ \tag{5.7}$$

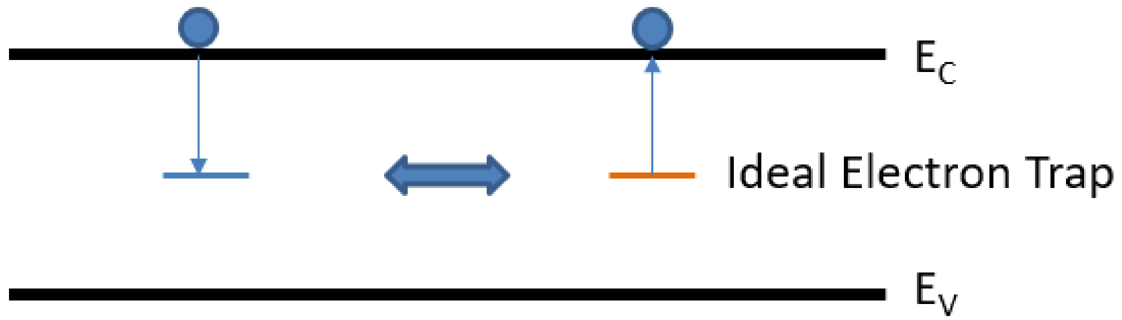

Figure 22. Ideal Electron Trapping.

And an ideal acceptor type recombination center as

$$R^0_{g,a} + e^- \longrightarrow R^-_{g,a} \tag{5.8}$$

$$R^-_{g,a} + h^+ \longrightarrow R^0_{g,a} \tag{5.9}$$

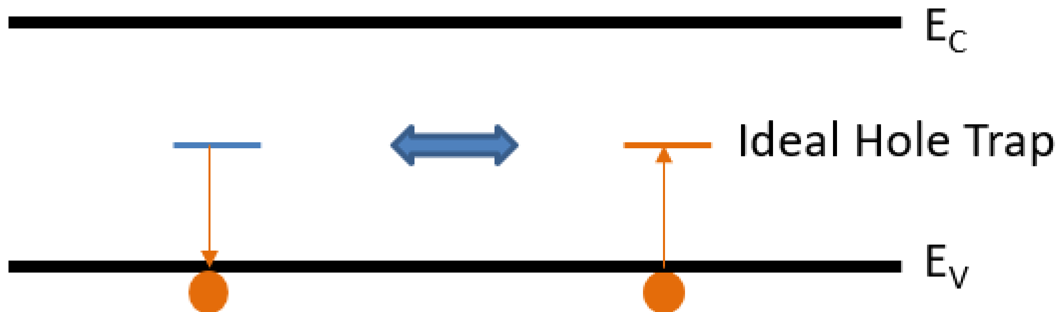

Figure 23. Ideal Hole Trapping.

Non idealities always occur in practical defects and both capture and emission of charge carriers occur in general. Based on the emission (e_n, e_p) and capture rates of carriers (c_n, c_p) we can classify the nature of point defect as trap or recombination center. The expression relating the capture rates to the trap levels and associated conditions for the trapping or recombination nature are given in Appendix H.

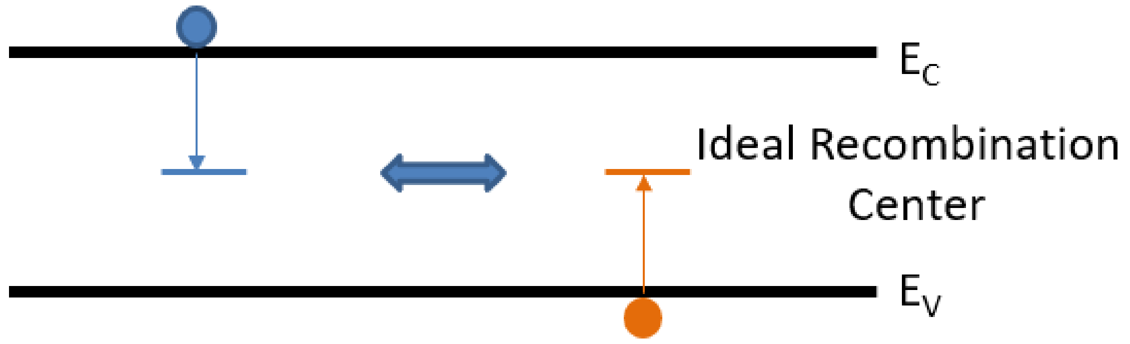

Figure 24. Ideal Recombination.

Table 12. Acceptor Type Point Defect from Recombination Nature to Trapping Nature.

σ_n cm^{-2}	σ_p cm^{-2}	V_{oc} V	J_{sc} $(\mathrm{mA/cm})^2$	FF Nil	Eff %
1e-10	1e-10	0.680	19.912	0.562	7.610
1e-15	1e-10	0.862	25.666	0.695	15.390
1e-20	1e-10	1.183	28.050	0.896	29.728
1e-25	1e-10	1.183	28.051	0.897	29.750
0	1e-10	1.183	28.051	0.897	29.750
1e-10	1e-10	0.680	19.912	0.562	7.610
1e-10	1e-15	0.854	26.557	0.776	17.579
1e-10	1e-20	0.965	27.668	0.838	22.373
1e-10	1e-25	1.183	28.219	0.899	30.013
1e-10	0	1.183	28.220	0.899	30.013

To understand the differences between traps and recombination centers we consider a CdTe solar cell device with vertical grain boundary as shown in Fig. 21. The device width is chosen as 1um. The strucutre has 3um thick absorber layer (CdTe) with 1e14 p-type doping, 0.5um ZnTe layer with 1e19 p-type doping at top, 0.04um of

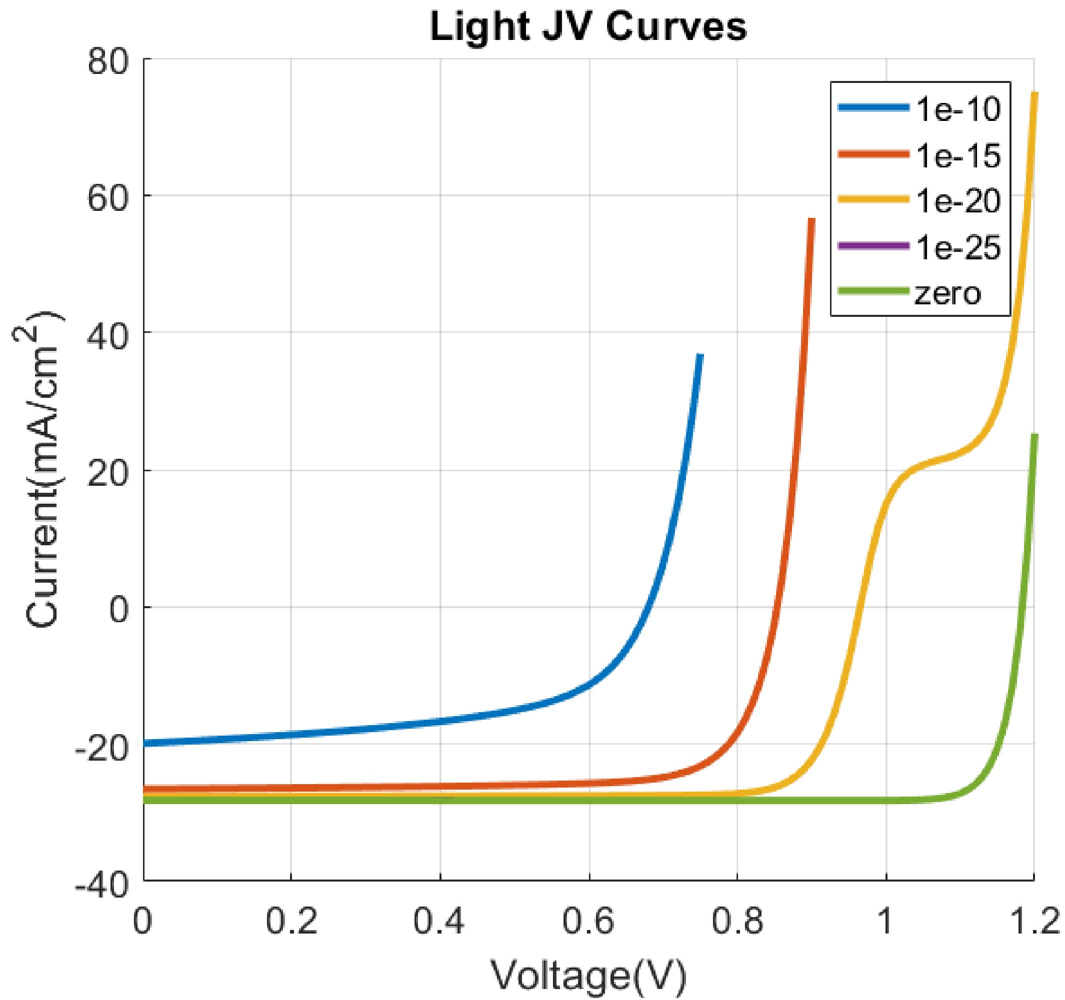

Figure 25. Light JV Curve with Acceptor Type Recombination to Acceptor Type Electron Trap.

CdS with 1e16 n-type doping at bottom of CdTe Layer followed by 0.46um of TCO doped with 1e18 donors. The absorber CdTe has two vertical grains with a width of 0.5um and grain boundary thickness is kept around 10nm. We incorporate a trap or recombination center at this grain boundary region with a concentration of 1e18 cm^{-3}. We set capture cross section limited rate model for the traps/recombination centers and allow all the capture and emission processes possible. Controlling the capture

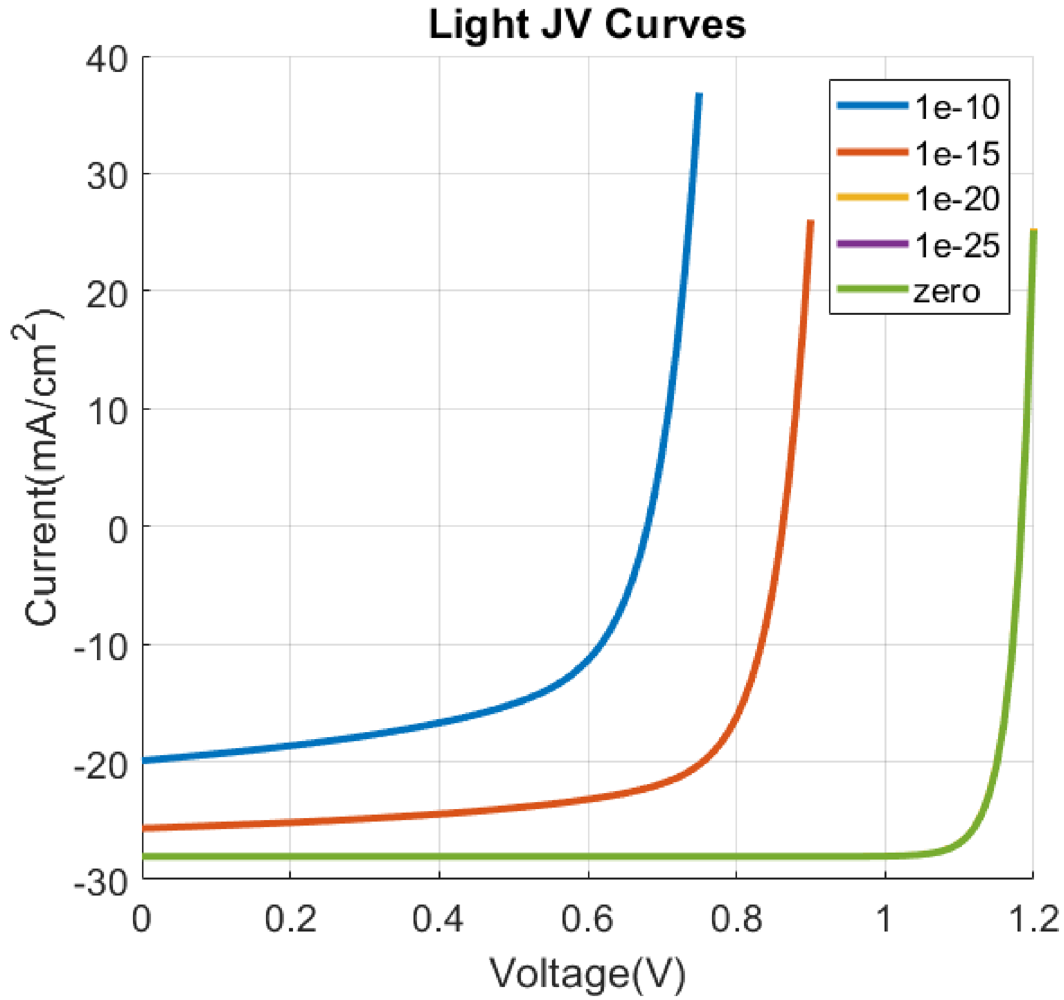

Figure 26. Light JV Curve with Acceptor Type Recombination to Acceptor Type Hole Trap.

cross section we can vary the nature of point defect from being a recombination center type to a trapping center type.

We set the capture cross section of 1e-10 cm^{-2} for both electron and hole capture processes and choose the trap level as the intrinsic fermi level. Now reducing the capture cross section of holes from 1e-10 to 1e-25 leads to reduce the capture rates of hole to a very low value, and setting to zero will make the point defect an ideal

Table 13. Donor Type Point Defect from Recombination Nature to Trapping Nature.

σ_n cm^{-2}	σ_p cm^{-2}	V_{oc} V	J_{sc} (mA/cm)^2	FF Nil	Eff %
1e-10	1e-10	0.592	6.169	0.337	1.231
1e-15	1e-10	0.753	7.117	0.494	2.648
1e-20	1e-10	0.963	24.21	0.811	18.918
1e-25	1e-10	1.183	27.86	0.903	29.754
0	1e-10	1.183	27.861	0.903	29.756
1e-10	1e-10	0.592	6.169	0.337	1.231
1e-10	1e-15	0.854	27.716	0.770	18.228
1e-10	1e-20	1.183	28.050	0.896	29.742
1e-10	1e-25	1.183	28.052	0.896	29.750
1e-10	0	1.183	28.052	0.896	29.750

electron trap. In a similar way reducing the capture cross section of electrons to zero will lead to an ideal hole trapping nature for the point defect. We varied capture cross sections for electrons and holes from 1e-10, 1e-15, 1e-20, 1e-25 and zero. Then we recorded the solar cell performance under AM1.5G light. The documented result is as given in Table 12 for acceptor type and Table 13 for donor type. The light JV curves for acceptor type recombination center to acceptor type electron trap is shown in Fig. 25. In this plot we note that ideal acceptor type electron trapping center does not have any recombination (green curve). For hole capture cross section of 1e-25 cm^{-2} (violet curve) the performance is still very close to the ideal case even though there is slight increase in the hole capture rates. An increase in the hole capture rates is going to increase the recombination rate. When the hole capture cross section is increased to 1e-20 cm^{-2} (yellow curve) the recombination rate increases further and we can see a decrease in the open circuit voltage causing a degradation in the device performance. We also note that there is a s-kink observed in the curve. We do not try to explain

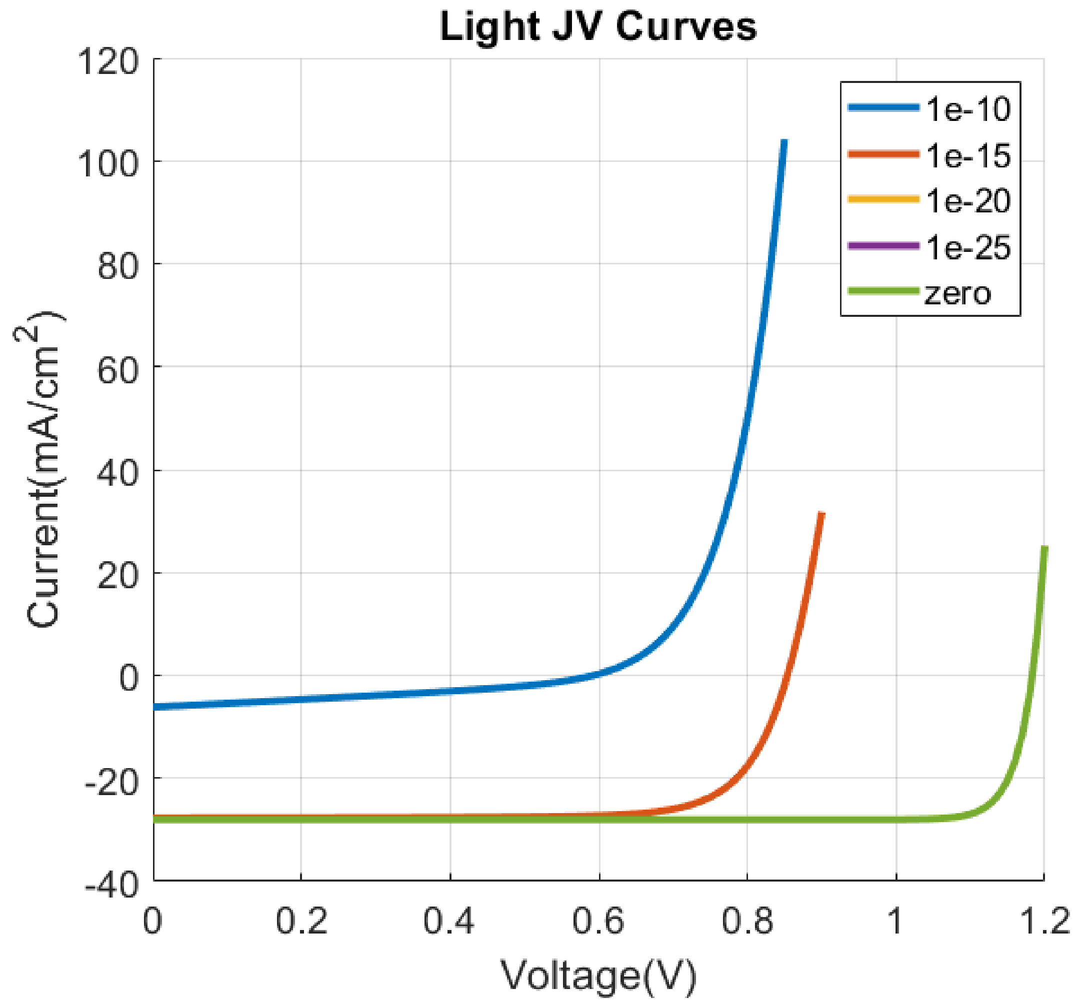

Figure 27. Light JV Curve with Donor Type Recombination to Donor Type Electron Trap.

the physical origin of this although it is sufficiently evident that it occurs through the changes in the recombination rates. When we further increase the hole capture cross section to 1e-15 cm^{-2} (red curve) we still see a decrease in both short circuit current and open circuit voltage. Finally when we take the hole capture cross section to 1e-10 cm^{-2} close to the ideal recombination center behavior we observe there is decrease in the short circuit current, open circuit voltage and fill factor. It is evident, for this particular simulation, that as the recombination rate increases at the point defect,

it first affects the open circuit voltage then short circuit current and finally the fill factor. A similar trend can be observed for the cases of acceptor type recombination centers to acceptor type hole traps (see Fig. 26), donor type recombination centers to donor type electron traps (see Fig. 27) and donor type recombination centers to donor type hole traps (see Fig. 28).

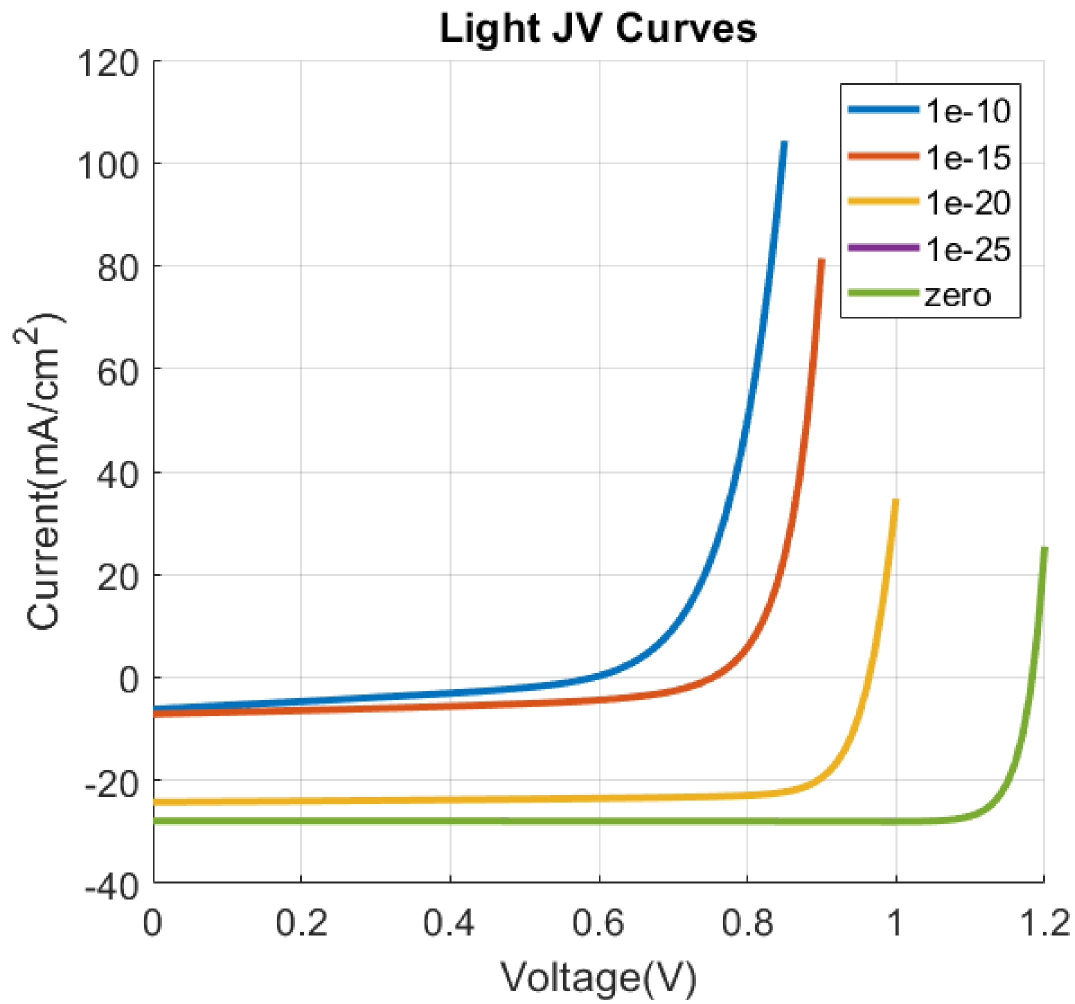

Figure 28. Light JV Curve with Donor Type Recombination to Donor Type Hole Trap.

From these results we conclude that an ideal trapping behavior of point defect

in the grain boundaries of CdTe solar cell does not affect the cell performance. It is the recombination nature of the point defect that degrades the cell performance. Moreover, as the recombination rate increases, it adversely affects the cell performance. We observed a similar trend with bulk defects as well, although we have not presented the results of the study here. We note that the shunting occurs when the point defect participates in recombination activity. Hence the shunting path could be related to the distribution of the point defect with the recombination activity.

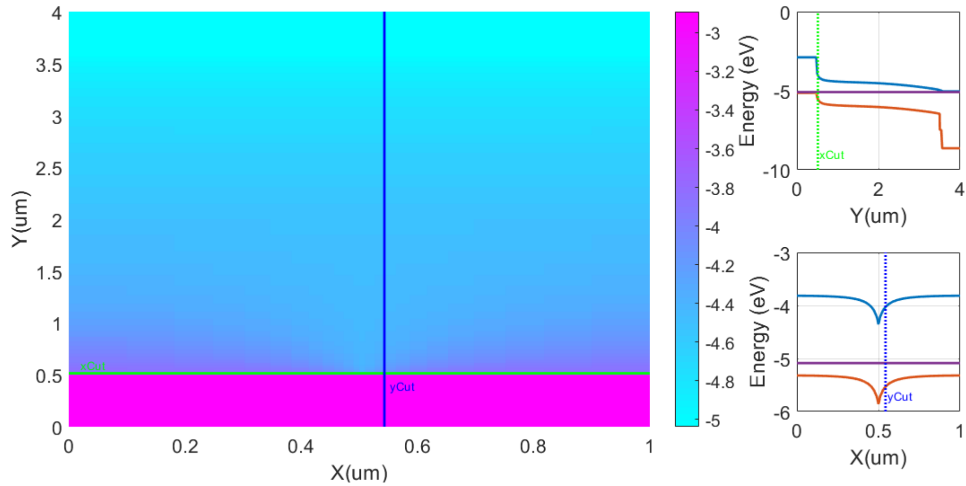

Figure 29. Downward Band Bending occurring due to Donor Type Point Defect at CdTe Vertical Grain Boundary.

Another interesting result we observed in these simulations is the band bending near grain boundary. In case of donor type recombination center or trapping center we note that the bands are bending down very close to the ZnTe/CdTe interface and for acceptor type of recombination center or trapping center the bands are bending up very close to the CdTe/CdS interface. These results are as shown in Fig. 29 and Fig. 30. From our simulations we conclude that both upward and downward band bending is possible in the CdTe GB and the bending is dominant if the GB is close

to the interfaces. This bending looks like Fermi pinning of bands to the point defect transition level.

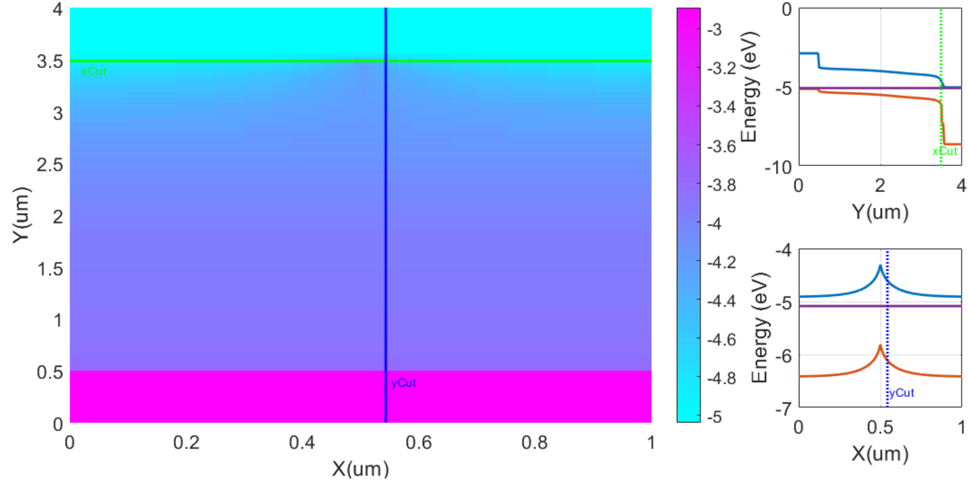

Figure 30. Upward Band Bending occurring due to Acceptor Type Point Defect at CdTe Vertical Grain Boundary.

The results of these simulation cannot be observed in a 1D structure and thus demonstrate the 2D capabilities of our tool.

5.8 Effects of Recombination Centers on Different Grain Boundary Structures

In this simulation we consider the same simulation structure described in section 5.7 except that we change the structure of the grain boundary in the CdTe layer from vertical to being a different geometry. The different geometrical structures of grain boundaries considered in this study are namely 1) vertical 2) horizontal 3) cross 4) T-shaped 5) inverted T-shaped 6) L-Shaped and 7) inverted L-shaped (as shown in Fig. 31). In all these geometrical structures we consider an acceptor type and a donor type defect with a concentration of 1e18 cm^{-3}.

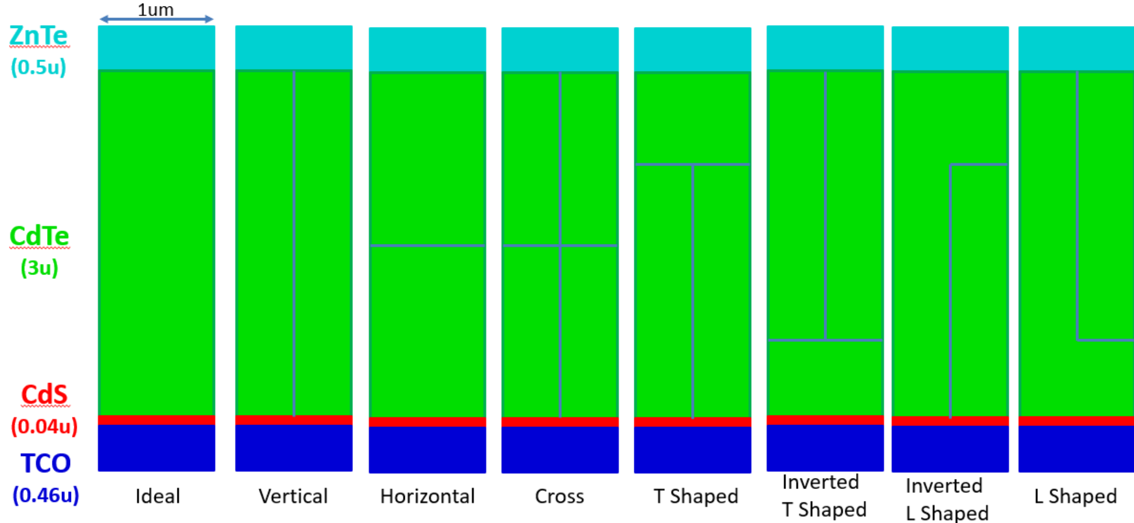

Figure 31. CdTe Device Structure with Vertical Grain Boundary.

The thickness of the grain boundary is kept around 10nm to 20nnm as the thickness in our simulation depends on the chosen mesh size. We perform light JV characterization under AM 1.5G light and record the solar cell performance. The solar cell performance obtained from the simulation is as given in Table 14 for acceptor type point defect, and in Table 15 for donor type point defect. The corresponding light JV curves are as shown in Fig. 32 and Fig. 33 respectively.

From the Tables 14 and 15, it is clear that the donor type recombination center is highly detrimental to the solar cell performance when compared to an acceptor type recombination center at the grain boundaries. For a given type of point defect, the solar cell performance is almost similar and when there is some vertical grain boundary the performance degrades more. Although horizontal grain boundaries result in lower performance than an ideal solar cell without recombination centers the performance is dependent on the location of the grain boundary with respect to the interface location.

Table 14. Comparison of Performance with Different Grain Boundary Strctures with Acceptor Type Point Defect.

Structure Name	V_{oc} V	J_{sc} $(mA/cm)^2$	FF Nil	Eff %
Cross	0.680	19.58	0.562	7.489
Horizontal	0.816	27.55	0.812	18.25
L-Shaped	0.765	27.11	0.738	15.12
T-Shaped	0.680	19.69	0.564	7.562
Vertical	0.680	19.72	0.564	7.568
iL-Shaped	0.680	19.76	0.563	7.576
iT-Shaped	0.738	26.65	0.734	14.43

Table 15. Comparison of Performance with Different Grain Boundary Structures with Donor Type Point Defect..

Structure Name	V_{oc} V	J_{sc} $(mA/cm)^2$	FF Nil	Eff %
Cross	0.453	0.302	0.432	0.059
Horizontal	0.592	0.763	0.681	0.307
L-Shaped	0.605	7.056	0.348	1.484
T-Shaped	0.493	0.206	0.700	0.071
Vertical	0.592	5.973	0.341	1.208
iL-Shaped	0.590	4.008	0.541	1.278
iT-Shaped	0.498	0.765	0.425	0.162

A horizontal grain boundary closer to the CdTe/ZnTe or CdTe/CdS has different impact than a horizontal grain boundary near to the bulk.

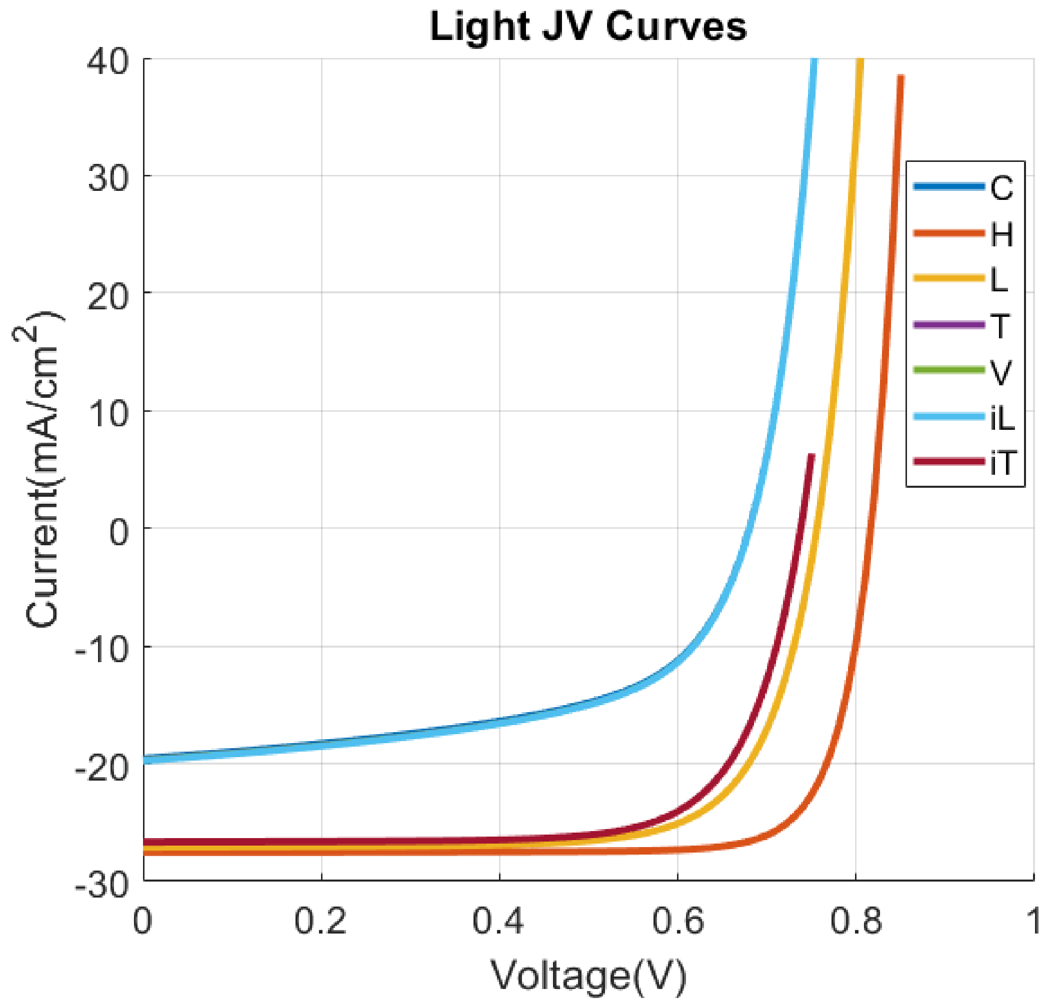

Figure 32. Comparison of Light JV curves for Different GB structures with Acceptor Type Recombination Center.

5.9 Experimental Characterization Emulation

In this section we present the application of our solver for emulating practical experimental characterization techniques. Since our tool solves time dependent equations, we can emulate experimental characterization techniques by providing time dependent stimulus. One application we already described is the emulation of light and dark JV curves for a solar cell type device structure. The tool has time dependent

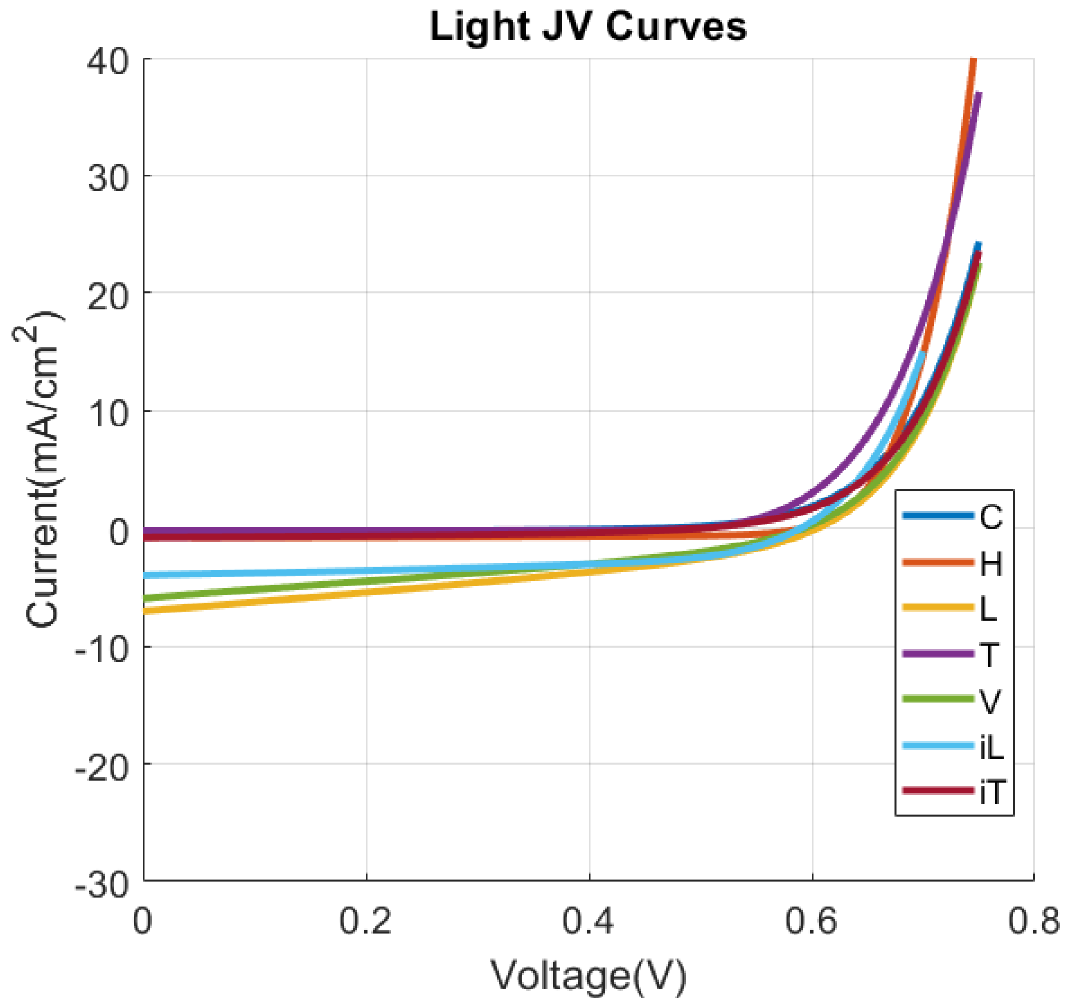

Figure 33. Comparison of light JV curves for Different GB Structures with Donor Type Recombination Center.

stimulus for light, temperature and voltage. This provides potential for emulating a vast number of experimental characterization techniques like light and dark JV, light and dark CV (capacitance-voltage), DLTS (Deep Level Transient Spectroscopy), TRPL (Time Resolved Photo-Luminescence), reverse recovery characterization etc. We describe few studies where we applied our tool for understanding CV data and hysteresis curves. Also we describe the progress on support for reverse recovery and DLTS emulation.

5.9.1 CV Emulation and Hysteresis

We emulate capacitance-voltage (CV) experimental characterization technique using the developed time dependent solver to understand the time evolution of interface traps or recombination centers. For this we collaborated with Prof. Michael Scarpulla from University of Utah. He provided a test simulation structure that is similar to the experimental device structure used for CV characterization. The test structure that we simulate is shown in Fig 34. It consists of a 3.8um of 1e15 cm^{-3} p-type doped CdTe layer followed by 10nm of CdTe/MZO interface with 1e18 of interface traps or recombination centers, 1e16 cm^{-3} n-type doped magnesium zinc oxide (MZO) and 1e17 cm^{-3} n-type doped TCO.

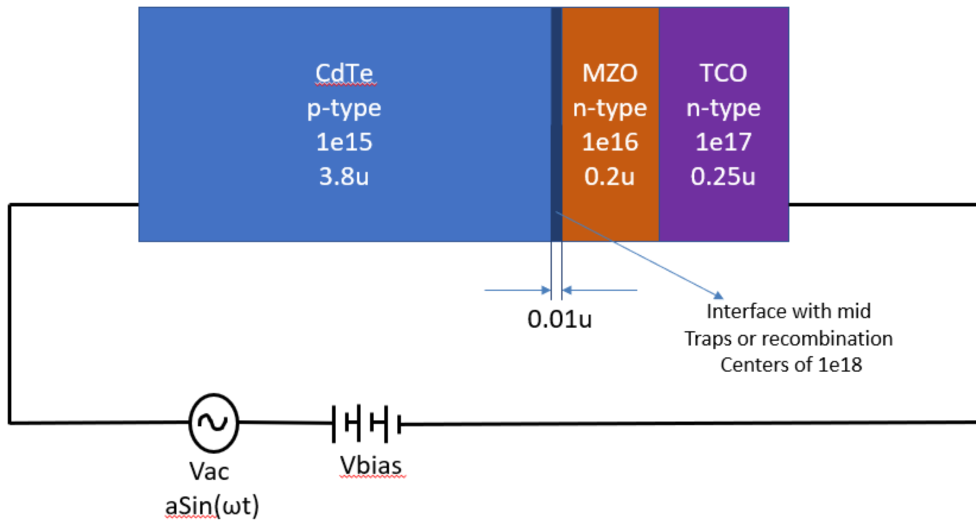

Figure 34. Test Structure Schematics for Emulating CV.

The schematics consists of a DC voltage source in series with an AC source. A constant dc bias with a sinusoidal ac input voltage is applied to the test structure and the current is measured through the simulation. The current response should

also be a sinusoidal signal. From the measured current density the capacitance can be easily calculated by taking the ac sinusoidal amplitude ratio of current density and input ac sinusoidal voltage. Hence we can measure the capacitance for a given input bias voltage. Varying the input bias from forward to reverse operation of the device structure will give the CV profile thus emulating the CV measurement process. Fig. 35 and Fig. 36 shows the forward and backward input voltage and output current density result applied to the test structure.

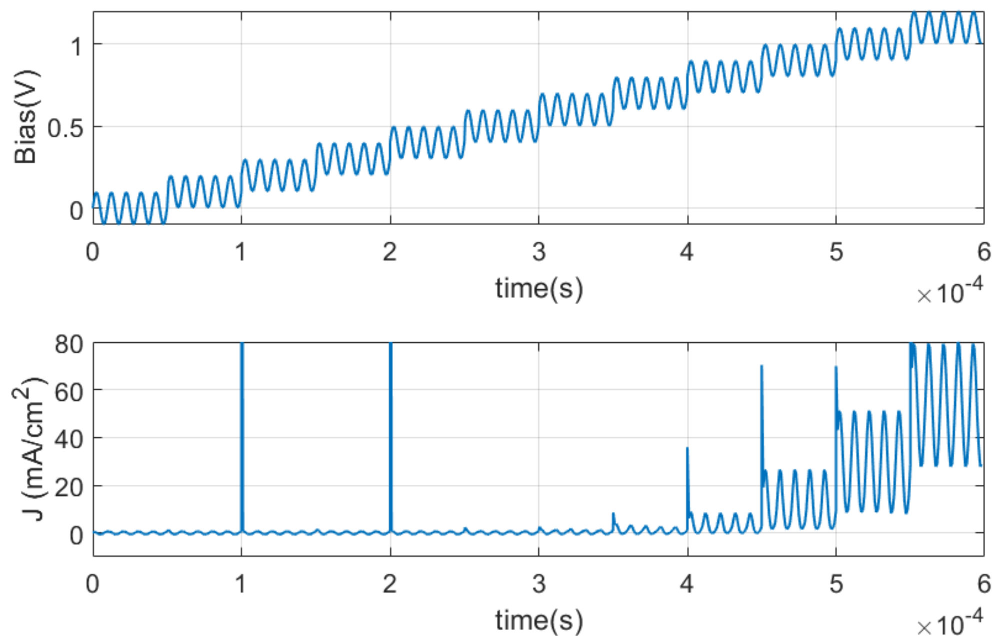

Figure 35. Input Stimulus and Output Response of CV Under Forward Bias Conditions.

Using the forward and reverse bias CV measurements we can determine the depletion width and dopant density of the test structure, thus we can plot the Mott-Schottky diagram as shown in Fig. 37.

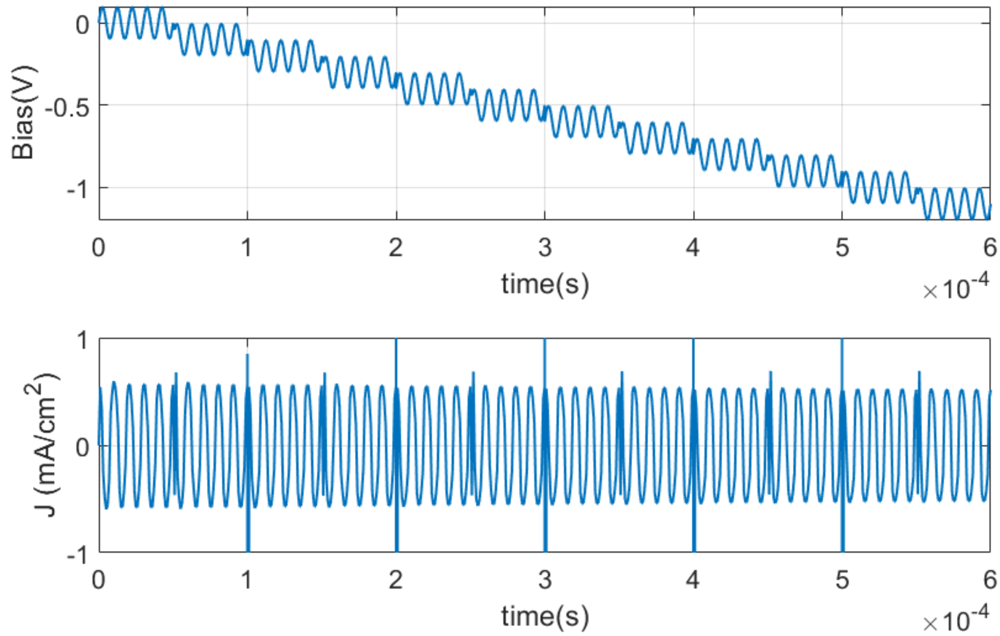

Figure 36. Input Stimulus and Output Response of CV Under Reverse Bias Conditions.

We note that we are giving the dopant density as input to the tool and thus not measuring anything new. Instead we are able to look into the dynamics of charging and discharging during the CV profiling.

Next, we applied 2 cycle stair case input sweeping from -1V to 1V to the test structure without an ac bias to understand the hysteresis behavior. The slew rate is kept at 100V/s and we observed a hysteresis as shown in Fig. 38. This hysteresis is caused by the acceptor type recombination center added at the interface between CdTe and MZO. When the slew rate is increased or decreased we did not observe any hysteresis in the simulation. Further simulations are necessary to understand the root causes of the hysteresis phenomena.

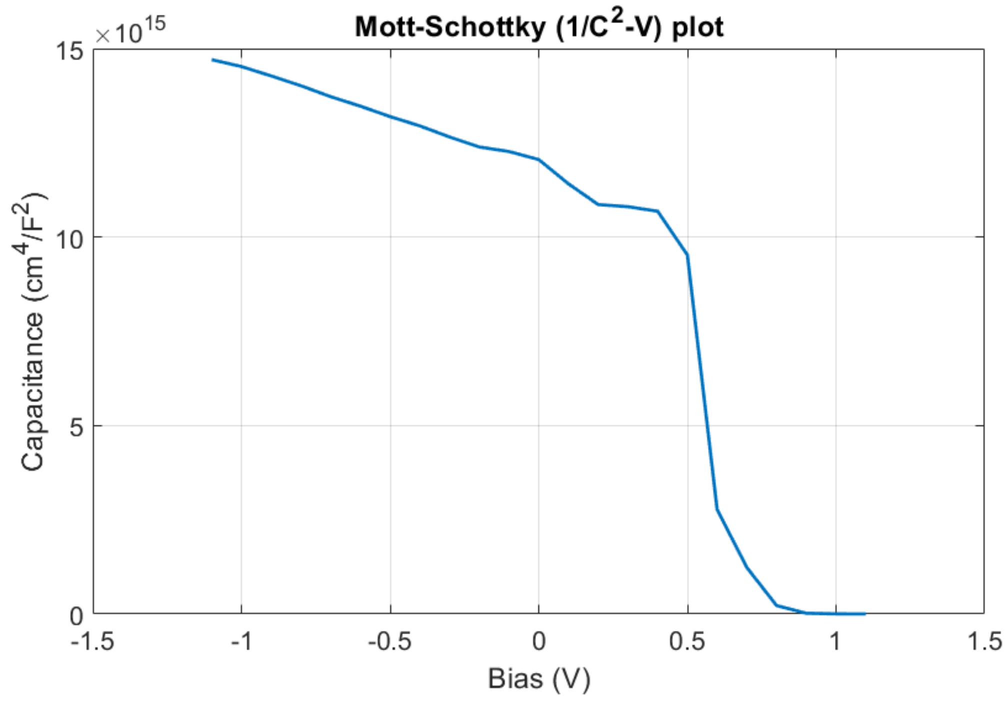

Figure 37. CV Results and Mott Schottky Plot.

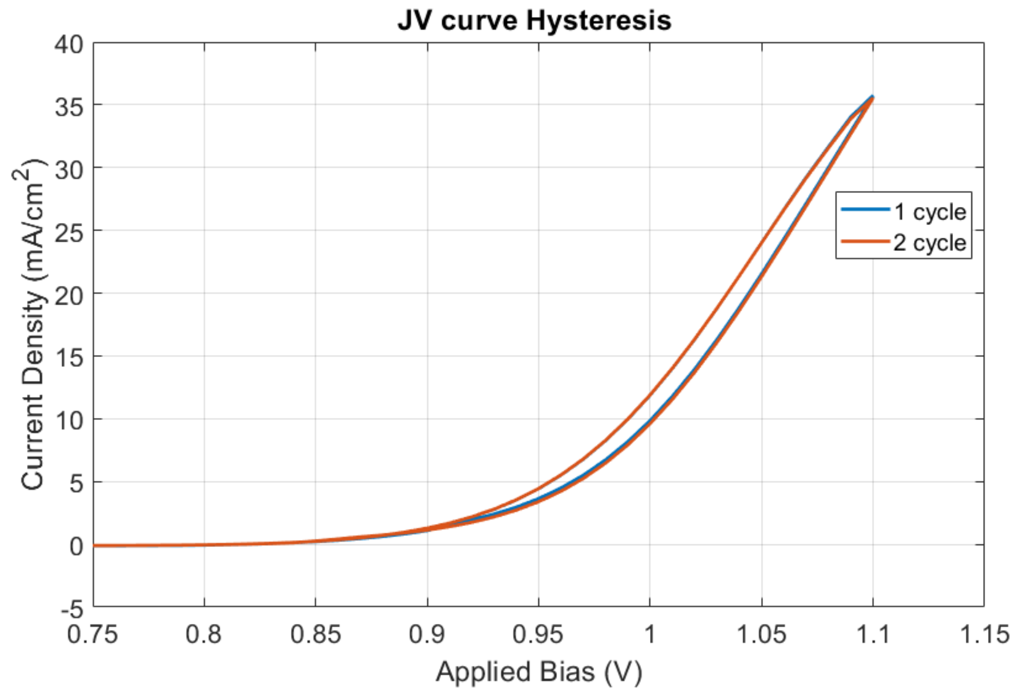

Figure 38. Hysteresis Occurring in the Structure as Observed with Simulation .

Chapter 6

CONCLUSIONS AND FUTURE WORK

The detailed understanding of microscopic processes causing the degradation in aging photovoltaic and electronic devices is important in analyzing the reliability issues and ensuring a long term operation. The state of the art TCAD tools available are limited in modeling the point defects for device and reliability studies.

For this purpose, we developed a 2D Unified Solver called PVRD-FASP that deals with detailed point defect dynamics and charge carriers in a comprehensive manner. The theoretical framework behind the developed solver is extensively discussed and the treating charge carriers and point defects on equal footing is justified with the theoretical arguments as well as simulation examples.

The 0D reaction solver was verified through analytical calculation for thermal generation and recombination of charge carriers, comparison with available published data on thermodynamic doping limit of copper defects in CdTe. The 1D/2D solver was verified on the simulation of CdTe/CdS heterojunction solar cell for light JV curves with Silvaco simulation. Perfect matching between the two simulation experiments was obtained. Finally, the drift-diffusion-reaction solver was tested on real experimental data of Cu diffusion into single crystal CdTe. Again, very good agreement with SIMS profiles with different annealing recipe simulation was obtained. We conclude that the PVRD-FASP solver can robustly perform relevant and diverse simulations to study diffusion/activation of dopants, device performance and other relevant processes for reliability issues. In fact, an advanced version of the solver developed by First Solar Inc. with our collaboration is currently being used in understanding of the Arsenic

activation mechanisms in CdTe [34] and understanding Cu doping in graded CdSeTe alloy absorber layer [46].

The PVRD-FASP tool is a first step towards the development of advanced reliability modeling tools with capability of applying same model equations for process and device TCAD. This kind of modeling is not only useful in reliability studies but also very helpful in understanding defect dynamics in radiation effects in materials.

6.1 Future Work

Although the tool is robust and efficient of performing diverse set of simulations, it still requires a lot of intellectual efforts for adaptation in the scientific community. As part of the PVRD project with DOE, we released a closed source version of our solver into public domain (available at http://pvrdfasp.com) for community adoption. Because of the needed intellectual effort required for accurate modeling as well as the theoretical calculations for DFT parameters, we find that a community based open source version of the tool is necessary. To achieve this we are working towards implementing a python based version of the PVRD-FASP tool called PyCDTS. This python based version is open source tool and any researcher can contribute to its development as well as use this tool in their research. The source codes are be available in PyPI repo as well as a gitlab based repo for deployment and development. The documentation of the tool is hosted in ReadTheDocs site.

In terms of advanced modeling we are planning to incorporate the following

- Support for Fermi-Dirac statistics.
- Support for incorporating gas phase reactions. This require extending the reaction solver to incorporate higher order reaction rate models.

- Support for modeling experimental characterization techniques.
- Incorporating advanced mobility models for charge carriers.
- Develop supporting infrastructure for graded material system.
- Implement advanced numerical methods improving the speed.
- Develop supporting infrastructure for radiation effects.
- Improve the predictability of the tool in conjunction with machine learning algorithms for calibrating model parameters.

6.1.1 Updates on PyCDTS

PyCDTS is released in the public domain at https://gitlab.com/abdul529/pycdts and is available through PyPI site. To install the tool use the following commands :

```
$ pip install pycdts
```

This will install PyCDTS with all the required dependencies. The latest version released is 0.2.0 and this version supports the simulation of 0D structures. It also support creation of 1D and 2D projects but there are bugs associated with non uniform meshing of numerical code. It works for uniform meshing projects for 1D and 2D. It supports graphical visualization of the results through PyQtGraph package and output results are saved as HDF file for managing large datasets. In the current version user can change the growth conditions through the chemical potentials of the material elemental phase. The tool dependencies are numpy, scipy, scikit-umpfack for numerical engine code, PyQt5, pyqtgraph, matplotlib, PyOpenGL for GUI code, h5py for HDF datasets, sqlite3 for databases.

6.2 Acknowledgments and Contributions

The material developed in this work is a combined efforts of our research group involved in the PVRD project funded by US Departartment of Energy. The material is based on the work supported by the US Department of Energy's Office of Energy Efficiency and Renewable Energy (EERE) under Solar Energy Technologies Office (SETO) Agreement Number DE-EE0007536. The people involved with this project are Dragica Vasileska (PI), Christian Ringhofer and myself from ASU, Igor Sankin and Dmitry Krasikov from First Solar Inc., Daniel Brinkman from San Jose State University and Hao Kang and Bedrich Benes from Purdue University. I sincerely thank everyone involved in the project who patiently listened to my questions and guided me in the right direction. Since this is a combined effort I could not give proper credits to the involved people. A general separation of works shared between the involved people are as below:

- First Principle modeling, material models, reaction models, diffusion models are from First Solar Inc. Special thanks to Dmitry Krasikov for elucidating the theory behind the models. The derivation of SRH recovery as a defect chemical reaction is contributed from ASU.
- A prototype of GUI was developed by First Solar and shared with Purdue University and the new GUI currently employed is the improved version of it from Hao Kang and Bedrich Benes from Purdue University.
- All mathematical modeling efforts are from ASU and SJSU. Thanks to Christian Ringhofer and Daniel Brinkman to resolve finite precision arithmetic issues and conditioning of matrices as required from practical point of view.
- Object oriented programming for the entire software was from First Solar and

Purdue university. The numerical engine OOP architecture is from myself and Dragica Vasileska with guidance from Chritian Ringhofer and Daniel Brinkman.

- All the simulation presented in the chapter 5 were done my myself at ASU with fruitful discussions with First Solar and SJSU.
- Project administrative tasks with reporting to DOE was mainly done by Dragica Vasileska. She encouraged all involved people for participation to conferences, workshops, giving invited talks and pressed for journal publications.

I also thank Dr. Yang and Dr. Su-Huai Wei for sharing their simulation data used in validating our solver for Cu doping limits in CdTe. Special thanks you Dr. Scarpulla for providing the CV and hysteresis simulation structures and guiding the emulation experiments.

REFERENCES

[1] Sarkar, C. K., *Technology Computer Aided Design* (CRC Press, 2016), URL https://www.taylorfrancis.com/books/9781315216454.

[2] "Silvaco TCAD", URL https://www.silvaco.com/products/tcad.html (Accessed: 2019-03-26).

[3] "Synopsys TCAD", URL https://www.synopsys.com/silicon/tcad.html (Accessed: 2019-03-26).

[4] Hussin, R., L. Gerrer, J. Ding, S. M. Amaroso, L. Wang, M. Semicic, P. Weckx, J. Franco, A. Vanderheyden, D. Vanhaeren, N. Horiguchi, B. Kaczer and A. Asenov, "Reliability aware simulation flow: From tcad calibration to circuit level analysis", in "2015 International Conference on Simulation of Semiconductor Processes and Devices (SISPAD)", pp. 152–155 (2015).

[5] Gummel, H., "A self-consistent iterative scheme for one-dimensional steady state transistor calculations", IEEE Transactions on Electron Devices **11**, 10, 455–465, URL http://ieeexplore.ieee.org/document/1473752/ (1964).

[6] Scharfetter, D. and H. Gummel, "Large-signal analysis of a silicon Read diode oscillator", IEEE Transactions on Electron Devices **16**, 1, 64–77, URL http://ieeexplore.ieee.org/document/1475609/ (1969).

[7] Antoniadis, D. A., S. E. Hansen, R. W. Dutton and A. G. Gonzales, "SUPREM I - A Program for IC Process Modeling and Simulation", Tech. Rep. SEL 77-006, Stanford University, California (1977).

[8] Pfäffli, P., H. Wong, X. Xu, L. Silvestri, X. Lin, T. Yang, R. Tiwari, S. Mahapatra, S. Motzny, V. Moroz and T. Ma, "Tcad modeling for reliability", Microelectronics Reliability **88-90**, 1083 – 1089 (2018).

[9] Kirchheim, R. and U. Kaeber, "Atomistic and computer modeling of metallization failure of integrated circuits by electromigration", Journal of Applied Physics **70**, 1, 172–181 (1991).

[10] Hassan, K. M., *Statistical modeling and simulation of variability and reliability of CMOS technology*, PhD dissertation, Purdue University (2016).

[11] Nakayashiki, K., J. Hofstetter, A. E. Morishige, T. A. Li, D. B. Needleman, M. A. Jensen and T. Buonassisi, "Engineering solutions and root-cause analysis for light-induced degradation in p-type multicrystalline silicon perc modules", IEEE Journal of Photovoltaics **6**, 4, 860–868 (2016).

[12] Duong, T., Y. Wu, H. Shen, J. Peng, S. Zhao, N. Wu, M. Lockrey, T. White, K. Weber and K. Catchpole, "Light and elevated temperature induced degradation (letid) in perovskite solar cells and development of stable semi-transparent cells", Solar Energy Materials and Solar Cells **188**, 27 – 36, URL http://www.sciencedirect.com/science/article/pii/S0927024818304240 (2018).

[13] Gou, X., X. Li, J. Yu, S. Wang, X. Zhang, S. Zhou, W. Fan and Q. Huang, "Influence of crystal defect density of silicon wafers on potential-induced degradation (pid) in solar cells and modules", physica status solidi (a) **214**, 9, 1700006, URL https://onlinelibrary.wiley.com/doi/abs/10.1002/pssa.201700006 (2017).

[14] Antoniadis, D. A., S. E. Hansen and R. W. Dutton, "SUPREM II - A Program for IC Process Modeling and Simulation", Tech. Rep. SEL 78-020, Stanford University, California (1978).

[15] *Sentaurus Process User Guide*, Synopsys, version P-2019.03 (2019).

[16] *Victory Process User's Manual*, Silvaco, version 7.22.3.R (2018).

[17] *Sentaurus Device User Guide*, Synopsys, version P-2019.03 (2019).

[18] *Victory Device User's Manual*, Silvaco, version 1.12.1.R (2018).

[19] Guo, D. and D. Vasileska, "Cu in CdTe Lab", URL https://nanohub.org/resources/predicts1d (2015).

[20] Shaik, A. R., D. Vasileska, D. Guo and R. Akis, "Cu in CdTe Lab (2D Version)", URL https://nanohub.org/resources/predicts2d (2016).

[21] Guo, D., D. Brinkman, A. Shaik, C. Ringhofer and D. Vasileska, "Metastability and reliability of CdTe solar cells", Journal of Physics D: Applied Physics **51**, 15 (2018).

[22] Guo, D., T. Fang, A. Moore, D. Brinkman, R. Akis, D. Krasikov, I. Sankin, C. Ringhofer and D. Vasileska, "Numerical simulation of copper migration in single crystal cdte", IEEE Journal of Photovoltaics **6**, 5, 1286–1291 (2016).

[23] Brinkman, D., D. Guo, R. Akis, C. Ringhofer, I. Sankin, T. Fang and D. Vasileska, "Self-consistent simulation of CdTe solar cells with active defects", Journal of Applied Physics **118**, 3 (2015).

[24] Guo, D., A. Moore, D. Krasikov, I. Sankin and D. Vasileska, "A comprehensive study of light soaking effect in cdte solar cells", in "2017 IEEE 44th Photovoltaic Specialist Conference (PVSC)", pp. 2816–2818 (2017).

[25] Guo, D., D. Vasileska, M. Bertoni, I. Sankin and S. Goodnick, *Modeling of Copper Migration In CdTe Photovoltaic Devices*, Phd thesis, ASU, URL http://hdl.handle.net/2286/R.I.46282 (2017).

[26] Pichler, P., *Intrinsic Point Defects, Impurities, and Their Diffusion in Silicon*, Computational Microelectronics (Springer Vienna, Vienna, 2004), URL http://link.springer.com/10.1007/978-3-7091-0597-9.

[27] Lundstrom, M. S. and R. J. Schuelke, "Numerical Analysis of Heterostructure Semiconductor Devices", IEEE Transactions on Electron Devices **30**, 9, 1151–1159 (1983).

[28] Krasikov, D. and I. Sankin, "Beyond thermodynamic defect models: A kinetic simulation of arsenic activation in CdTe", Physical Review Materials **2**, 10, 103803 (2018).

[29] Tilley, R. J. D., *Defects in Solids* (John Wiley & Sons, Inc., Hoboken, NJ, USA, 2008), URL http://doi.wiley.com/10.1002/9780470380758.

[30] Kroger, F., *The Chemistry of Imperfect Crystals, Volume 2: Imperfection Chemistry of Crystalline Solids* (North-Holland Pub. Co, 1974), 2 edn.

[31] Shockley, W. and W. T. Read, "Statistics of the Recombination of Holes and Electrons", Physical Review **87**, 46, 835–842 (1952).

[32] Yang, J.-H., W.-J. Yin, J.-S. Park, J. Ma and S.-H. Wei, "Review on first-principles study of defect properties of CdTe as a solar cell absorber", Semiconductor Science and Technology **31**, 8, 083002, URL http://stacks.iop.org/0268-1242/31/i=8/a=083002?key=crossref.fc3369f5bb9e2a643b5b4cbae0cc5fac (2016).

[33] Fahey, P. M., P. B. Griffin and J. D. Plummer, "Point defects and dopant diffusion in silicon", Reviews of Modern Physics (1989).

[34] Krasikov, D. and I. Sankin, "Beyond thermodynamic defect models: A kinetic simulation of arsenic activation in CdTe", Physical Review Materials **2**, 10, 103803, URL https://link.aps.org/doi/10.1103/PhysRevMaterials.2.103803 (2018).

[35] Trupke, T., M. A. Green, P. Wurfel, P. P. Altermatt, A. Wang, J. Zhao and R. Corkish, "Temperature dependence of the radiative recombination coefficient of intrinsic crystalline silicon", Journal of Applied Physics **94**, 8, 4930, URL http://scitation.aip.org/content/aip/journal/jap/94/8/10.1063/1.1610231 (2003).

[36] Nguyen, H. T., S. C. Baker-Finch and D. Macdonald, "Temperature dependence of the radiative recombination coefficient in crystalline silicon from spectral photoluminescence", Applied Physics Letters **104**, 11, 112105, URL http://aip.scitation.org/doi/10.1063/1.4869295 (2014).

[37] Varshni, Y., "Temperature dependence of the energy gap in semiconductors", Physica **34**, 1, 149–154, URL https://www.sciencedirect.com/science/article/pii/0031891467900626 (1967).

[38] Gummel, H., "A self-consistent iterative scheme for one-dimensional steady state transistor calculations", IEEE Transactions on Electron Devices **11**, 10, 455–465, URL http://ieeexplore.ieee.org/document/1473752/ (1964).

[39] Guo, D., T. Fang, A. Moore, D. Brinkman, R. Akis, D. Krasikov, I. Sankin, C. Ringhofer and D. Vasileska, "Numerical Simulation of Copper Migration in Single Crystal CdTe", IEEE Journal of Photovoltaics (2016).

[40] Shaik, A., D. Brinkman, I. Sankin, D. Krasikov, C. Ringhofer and D. Vasileska, "A Unified 2D Solver for Modeling Carrier and Defect Transport in Photovoltaic Devices", in "2018 IEEE 7th World Conference on Photovoltaic Energy Conversion, WCPEC 2018 - A Joint Conference of 45th IEEE PVSC, 28th PVSEC and 34th EU PVSEC", (2018).

[41] Yang, J. H., W. K. Metzger and S. H. Wei, "Carrier providers or killers: The case of Cu defects in CdTe", Applied Physics Letters **111**, 4 (2017).

[42] Yang, J.-H., J.-S. Park, J. Kang and S.-H. Wei, "First-principles multiple-barrier diffusion theory: The case study of interstitial diffusion in CdTe", Physical Review B **91**, 7, 075202, URL https://link.aps.org/doi/10.1103/PhysRevB.91.075202 (2015).

[43] Krasikov, D. and I. Sankin, "Defect interactions and the role of complexes in the CdTe solar cell absorber", J. Mater. Chem. A (2017).

[44] Menéndez-Proupin, E., M. Casanova-Páez, A. L. Montero-Alejo, M. A. Flores and W. Orellana, "Symmetry and thermodynamics of tellurium vacancies in cadmium telluride", Physica B: Condensed Matter **568**, January, 81–87, URL https://doi.org/10.1016/j.physb.2019.01.013 (2019).

[45] Flores, M. A., W. Orellana and E. Menéndez-Proupin, "First-principles DFT + GW study of the Te antisite in CdTe", Computational Materials Science **125**, 176–182 (2016).

[46] Sankin, I. and D. Krasikov, "Kinetic Simulations of Cu Doping in Chlorinated CdSeTe PV Absorbers", physica status solidi (a) **216**, 15, 1800887, URL https://onlinelibrary.wiley.com/doi/abs/10.1002/pssa.201800887 (2019).

APPENDIX A

STANDARD SEMICONDUCTOR EQUATIONS FOR CHARGE CARRIERS FROM ELECTROCHEMICAL FORMULATION

For charge carriers we can simplify the differential equations given in (2.8)-(2.10) as

$$\frac{\partial n}{\partial t} = -\nabla \cdot \overrightarrow{J_n} + G_n - R_n \tag{A.1}$$

$$\overrightarrow{J_n} = -\frac{D_n}{kT} n \nabla \left(G_{f,n}^0 - q_0 \phi + kT \ln \left(\frac{n}{N_C} \right) \right) \tag{A.2}$$

$$\frac{\partial p}{\partial t} = -\nabla \cdot \overrightarrow{J_p} + G_p - R_p \tag{A.3}$$

$$\overrightarrow{J_p} = -\frac{D_p}{kT} p \nabla \left(G_{f,p}^0 + q_0 \phi + kT \ln \left(\frac{p}{N_V} \right) \right) \tag{A.4}$$

$$-\nabla \cdot (\varepsilon \nabla \phi) = -p + n - N_D + N_A \tag{A.5}$$

Using the formation energies of the free carriers as given in (2.48), we can simplify the flux equation as

$$\overrightarrow{J_n} = -\frac{D_n}{kT} n \nabla \left(-\chi - kT \ln N_c \right) - \mu_n n \overrightarrow{E} - D_n \nabla n, \tag{A.6}$$

$$\overrightarrow{J_p} = -\frac{D_p}{kT} p \nabla \left(\chi + E_g - kT \ln N_V \right) + \mu_p p \overrightarrow{E} - D_p \nabla p, \tag{A.7}$$

where we used the definition of electric field and Einstein relationship between diffusivity and mobility. The above equations are the standard semiconductor equations for heterostructures (see [27]) and in the case of homogeneous structure the first gradient term vanishes to zero. Thus, the flux equation reduces to

$$\overrightarrow{J_n} = -\mu_n n \overrightarrow{E} - D_n \nabla n, \tag{A.8}$$

$$\overrightarrow{J_p} = \mu_p p \overrightarrow{E} - D_p \nabla p, \tag{A.9}$$

which are the standard flux equations for charge carriers in semiconductors.

APPENDIX B

RELATIONSHIP BETWEEN TRANSITION LEVEL AND FORMATION ENTHALPY FOR DEFECTS

Suppose the formation enthalpies and transition levels of a defect are as shown in Figure 39. Then it is clear that

$$\begin{aligned}
\Delta H_f^{+} &= \Delta H_f^{0} - (+1)\left(E_{+/0} - 0\right), \\
\Delta H_f^{'} &= \Delta H_f^{0} - (+1)\left(E_{+/0} - E_{2+/+}\right), \\
\Delta H_f^{2+} &= \Delta H_f^{'} - (+2)\left(E_{2+/+} - 0\right), \\
\Delta H_f^{+} &= \Delta H_f^{0} - (-1)\left(E_{0/-} - 0\right),
\end{aligned} \tag{B.1}$$

by simple rules of coordinate geometry for straight lines with slopes. For further details please see Ref. [32]

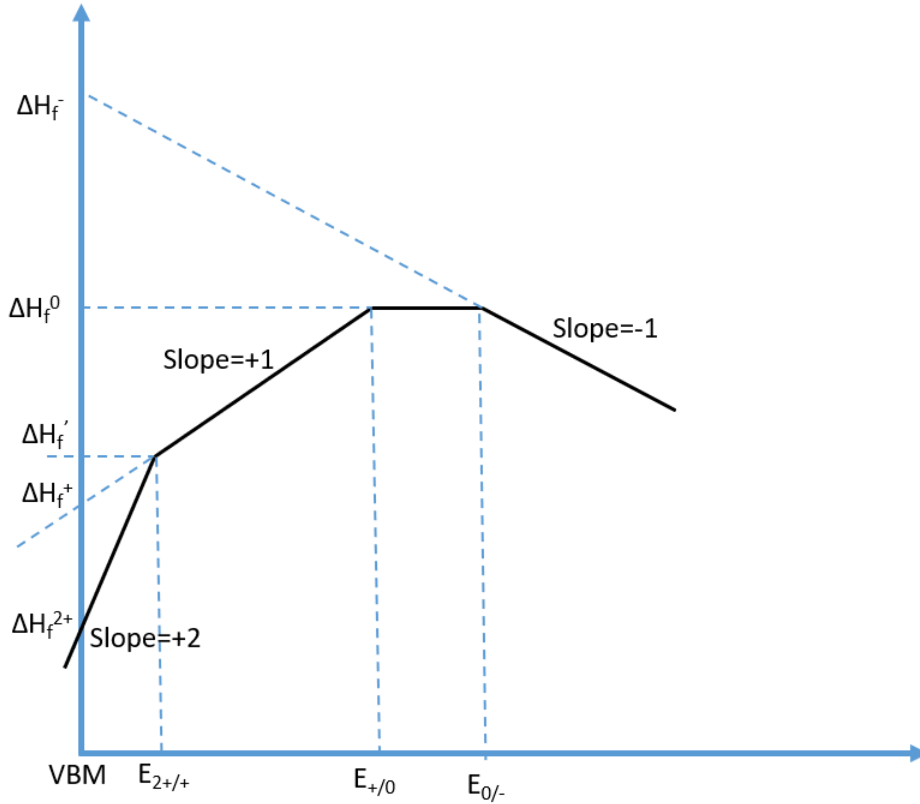

Figure 39. Defect Formation Energy wrt Valence Band Maxima (VBM).

APPENDIX C

LINEARIZED POISSON EQUATION

Consider the system of differential equations given in (3.3) ignoring the generation-recombination. The reactions conserve charge and therefore do not impact Poisson's equation. Transforming to Slotboom variables we have

$$\frac{\partial}{\partial t}\left(w_i e^{-\Psi_i}\right) = \nabla \cdot \left(D_i e^{-\Psi_i} \nabla w_i\right), \quad w_i = u_i e^{\Psi_i},$$
$$-\nabla \cdot (\varepsilon \nabla \phi) = q_0 \sum_i z_i w_i e^{-\frac{G^0_{f,i} + q_0 z_i \phi - kT \ln N_{s,i}}{kT}} \tag{C.1}$$

The Poisson equation in (C.1) is nonlinear and linearizing it around ϕ^{old} results in

$$-\nabla \cdot (\varepsilon \nabla \phi^{new}) = q_0 \sum_i z_i w_i e^{-\Psi_i^{old}} \left(1 - \frac{q_0 z_i}{kT}\left(\phi^{new} - \phi^{old}\right)\right) \tag{C.2}$$

Transforming back from Slotboom to normal variables gives

$$-\nabla \cdot (\varepsilon \nabla \phi^{new}) = q_0 \sum_i z_i u_i e^{\frac{q_0 z_i}{kT}\left(\phi^G - \phi^{old}\right)} \left(1 - \frac{q_0 z_i}{kT}\left(\phi^{new} - \phi^{old}\right)\right) \tag{C.3}$$

where ϕ^G is the previous Gummel loop solution. Thus, we have

$$-\nabla \cdot (\varepsilon \nabla \phi^{new}) + \left(\frac{q_0^2}{kT} \sum_i z_i^2 u_i e^{\frac{q_0 z_i}{kT}\left(\phi^G - \phi^{old}\right)}\right) \phi^{new}$$
$$= q_0 \sum_i z_i u_i e^{\frac{q_0 z_i}{kT}\left(\phi^G - \phi^{old}\right)} + \left(\frac{q_0^2}{kT} \sum_i z_i^2 u_i e^{\frac{q_0 z_i}{kT}\left(\phi^G - \phi^{old}\right)}\right) \phi^{old} \tag{C.4}$$

From this we can write the linearized operator as

$$\hat{L} = \left(\frac{q_0^2}{kT} \sum_i z_i^2 u_i e^{\frac{q_0 z_i}{kT}\left(\phi^G - \phi^{old}\right)}\right), \tag{C.5}$$

$$\hat{L}_1 = q_0 \sum_i z_i e^{\frac{q_0 z_i}{kT}\left(\phi^G - \phi^{old}\right)} \tag{C.6}$$

These operators can be written as matrices for a given numerical discretization scheme and we get $\mathcal{L}$ and $\mathcal{L}_1$.

APPENDIX D

TIME EVOLUTION OF THERMALLY GENERATED CARRIERS

The reaction representing thermally generated carriers is given in (2.28). The differential equation for this system is (2.29). Choosing charge neutrality for the initial condition we have

$$n(0) = p(0), \quad n(t) = p(t), \tag{D.1}$$

where $n(t)$ and $p(t)$ represent the concentrations of electrons and holes at time t. Thus, the differential equation to be solved is given as

$$\frac{dp}{dt} = \frac{dn}{dt} = K_b \left(n_i^2 - n^2 \right), \tag{D.2}$$

which is a Ricatti equation with the constant value $n(t) = n_i$ as one particular solution. Obviously, this solution cannot be the physically correct solution to our system. The other solution can be found by writing the solution as

$$n(t) = n_i + \frac{1}{z} \tag{D.3}$$

Substituting this into (D.2) and simplifying we get

$$-\frac{1}{z^2}\frac{dz}{dt} = K_b \left(n_i^2 - \left(n_i + \frac{1}{z} \right)^2 \right) \tag{D.4}$$

$$\implies \frac{1}{z^2}\frac{dz}{dt} = K_b \left(\frac{2n_i}{z} + \frac{1}{z^2} \right) \tag{D.5}$$

$$\implies \frac{dz}{dt} - 2K_b n_i z - K_b = 0 \tag{D.6}$$

$$\implies \frac{d}{dt}\left(z e^{-2K_b n_i t} \right) = K_b 2^{-2K_b n_i t} \tag{D.7}$$

$$\implies z(t)e^{-2K_b n_i t} - z(0)e^0 = K_b \frac{e^0 - e^{-2K_b n_i t}}{2K_b n_i} \tag{D.8}$$

$$\implies z(t) = z(0)e^{2K_b n_i t} + \frac{2^{2K_b n_i t} - 1}{2n_i} \tag{D.9}$$

The value of $z(0)$ can be found as

$$n(0) = n_i + \frac{1}{z(0)} \tag{D.10}$$

$$\implies z(0) = \frac{1}{n(0) - n_i}. \tag{D.11}$$

Hence the final solution is given as

$$n(t) = n_i + \frac{1}{z(t)} \tag{D.12}$$

$$= n_i + \frac{1}{\left(\frac{1}{n(0) - n_i}\right) e^{2K_b n_i t} - \frac{1}{2n_i}} \tag{D.13}$$

$$= n_i + \frac{2}{\left(\frac{2}{n(0) - n_i}\right) e^{2K_b n_i t} - \frac{1}{n_i}} \tag{D.14}$$

APPENDIX E

COPPER DOPING LIMITS IN CDTE SIMULATION RESULTS

The authors Yang *et al.*, performed the simulation with total Cu incorporation from 1e15 to 1e19 cm^{-3}. We further performed the simulation from very low doping of 1e0 to 1e19 cm^{-3} with 1 point per decade (i.e., 1,5,10,...,1e18,5e18,1e19) for Cd-poor conditions as well as slightly poor Cd condition as given in [41]. The results are as shown in Fig. 40 and Fig. 41. The figures show the formation energies of the Cu defects at their respective Cd conditions. As the total Cu incorporation is increased from 1 to 1e19 cm^{-3} (right Y-axis) the calculated Fermi level is shown in the blue dotted curve.

It is evident that for Cd slightly poor conditions the thermodynamic limit sets the Fermi level to 0.36eV (the crossing of solid black line with red line) which corresponds to hole concentration of approximately 1e13 cm^{-3}. This occurs at the total Cu doping of approximately 1e14 cm^{-3}. Any further incorporation of Cu above 1e14 cm^{-3} does not increase the hole concentration in the material.

In case of Cd poor conditions the thermodynamic limit does not set the limit to Fermi level with the incorporation of Cu (mainly because red and black solid lines never cross and thermodynamically Cu_C is still favorable). A hole concentration as high as 5e17 cm^{-3} is thermodynamically feasible. We note that the material growth conditions impact the hole concentration limits.

Finally we also note that although thermodynamically the above hole concentrations are feasible it may not be kinetically feasible. The thermodynamic limits gives the final conditions at the end of universe or a very long time much above the time frames we are trying to analyze. It will be important to do a kinetic simulations to determine whether the limits are achievable in the time frame of device fabrication and if they still hold till the lifetime of the fabricated device. Also we have not included other point defects in this study that might affect the doping limits.

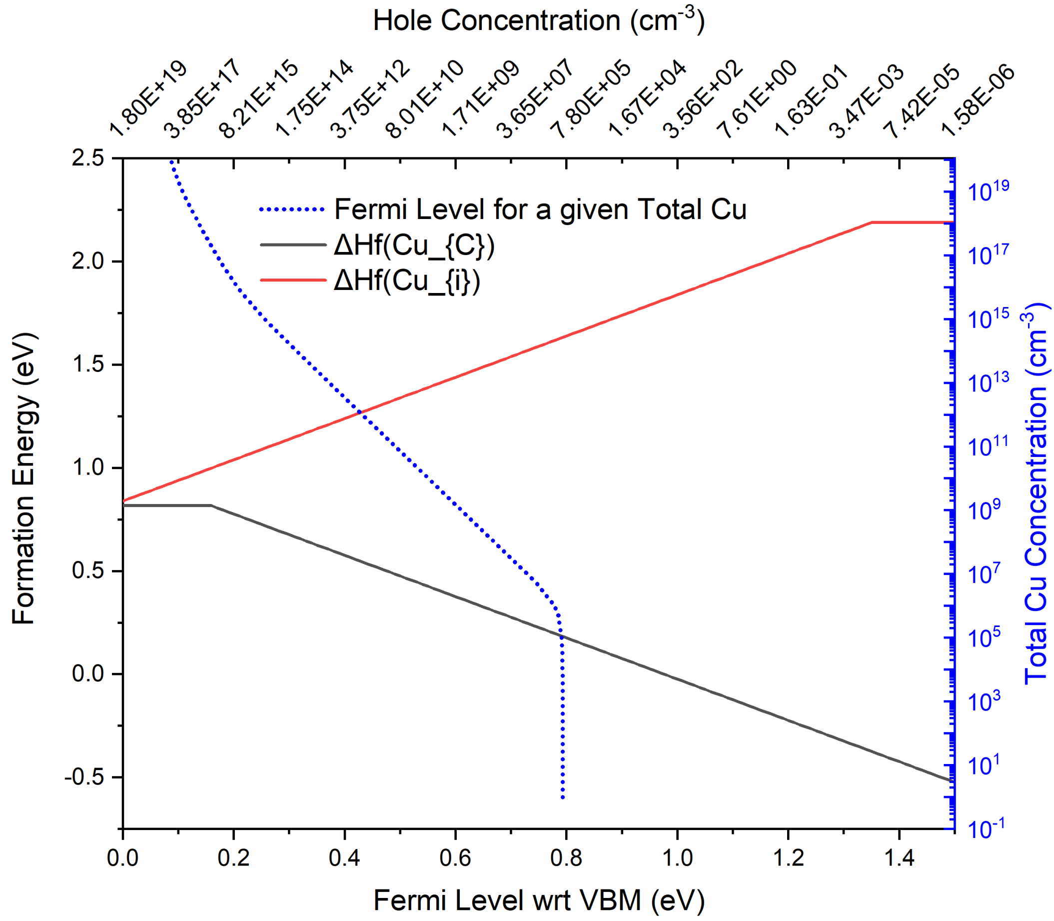

Figure 40. Cu Doping Limits in CdTe Under Cd Poor Conditions at 300K.

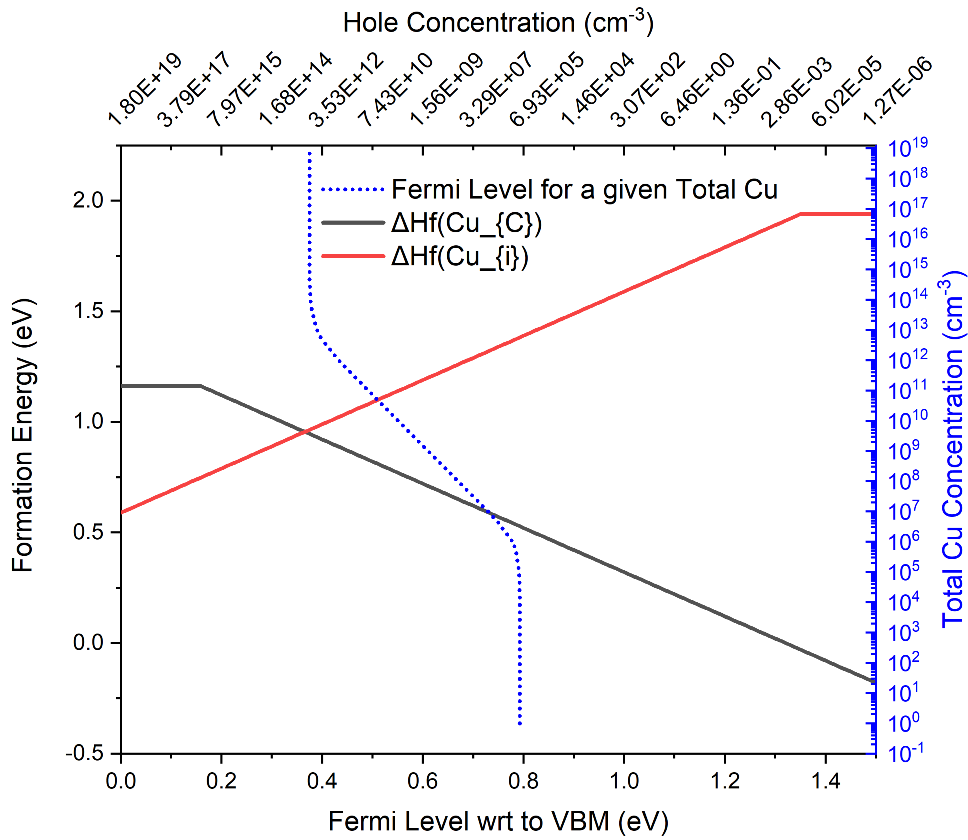

Figure 41. Cu Doping Limits in CdTe Under Cd Slightly Poor Conditions at 300K.

APPENDIX F

DFT PARAMETERS USED IN THE SX CDTE SIMULATIONS AS WELL AS FULL STACK CDTE SIMULATION

The DFT parameters given here are mainly taken from [32, 42, 43]. We modify(calibration) the parameters to match the experimental result at 350°C 3min anneal recipe. Then we used these parameters to perform simulation at other anneal recipes. The DFT parameters we list here are mainly formation energies (wrt vacuum) in eV, transition level (wrt VBM) in eV, diffusion prefactors (cm^2/s), diffusion barriers (eV) and assumed reaction model parameters. The common material parameters are:

Table 16. Material Parameters.

Parmeter Name	**ZnTe**	**CdTe**	**CdS**	**TCO**
NC300 (cm^{-3})	7.8e17	7.8e17	7.8e17	7.8e17
NV300 (cm^{-3})	1.8e19	1.8e19	1.8e19	1.8e19
E_0 (eV)	2.3815	1.602	2.5825	3.6
α (eV/K)	5.2e-4	4.61e-4	3.06e-3	0
β (K)	165	160.1	2156	160
ε_r	11	11	11	11
χ (eV)	3.53	4.4	4.4	4.4
$\mu_{n,300K}$ (V/cm^2/s)	300	400	400	400
$\mu_{p,300K}$ (V/cm^2/s)	100	200	200	200
m_e^*	0.1	0.1	0.1	0.1
m_h^*	0.8	0.8	0.8	0.8
B_{rad} (cm^3/s)	1e-11	1e-11	1e-11	1e-11

F.1 sX CdTe simulation parameters

All carrier capture reactions have capture cross section of 1e-15 cm^2.

Table 17. Point Defect Formation Energies and Transition Levels in ZnTe and CdTe.

Defect Name	**ZnTe**		**CdTe**	
	G_f^0 (eV)	E_T (eV)	G_f^0 (eV)	E_T (eV)
$[Cu_C Cu_i]^0$	1.06	—	1.58	—
$[Cu_C Cd_i]^+$	2.71	1.28 (0/+)	2.72	1.28 (0/+)
Cu_C^-	0.81	0.16 (-/0)	0.81	0.16 (-/0)
Cu_C^0	0.81	—	0.81	—
Cu_i^+	2.19	1.35 (0/+)	2.19	1.35 (0/+)
Cu_i^0	2.19	—	2.19	—
Cd_i^{2+}	3.4	1.31 (+/2+)	2.64	1.31 (+/2+)
Cd_i^+	3.4	1.31 (0/+)	2.64	1.31 (0/+)
Cd_i^0	3.4	—	2.64	—
N_A^-	0	0.1 (-/0)	0	0.1 (-/0)
N_A^0	0	—	0	—

Table 18. Point Defect Diffusion Prefactors and Barriers in ZnTe and CdTe.

Defect Name	**ZnTe**		**CdTe**	
	D_0 (cm^2/s)	E_D (eV)	D_0 (cm^2/s)	E_D (eV)
$[Cu_C Cu_i]^0$	0	0	1.5e-3	0.65
$[Cu_C Cd_i]^+$	0	0	6.3e-3	1.06
Cu_C^-	0	0	0	0
Cu_C^0	0	0	0	0
Cu_i^+	6.3e-3	0.25	6.3e-3	0.46
Cu_i^0	3.53e-3	0.28	3.53e-3	0.28
Cd_i^{2+}	3.21e-3	0.25	3.21e-3	0.47
Cd_i^+	3.21e-3	0.47	3.21e-3	0.47
Cd_i^0	5.2e-3	0.6	5.2e-3	0.6
N_A^-	0	0	0	0
N_A^0	0	0	0	0

F.2 Full stack CdTe simulation parameters

For full stack CdTe Cu simulation, the same parameters are used as in the case of sX CdTe simulation. The differences are N_D generic donor point defect is added in CdS and TCO layers. The properties of these defects are listed for completeness.

Table 19. Point defect formation energies and transition levels in CdS and TCO.

Defect Name	**CdS**		**TCO**	
	G_f^0 (eV)	E_T (eV)	G_f^0 (eV)	E_T (eV)
N_D^+	0	2.37 (0/+)	0	3.5 (0/+)
N_D^0	0	—	0	—

Table 20. Point Defect Diffusion Prefactors and Barriers in CdS and TCO.

Defect Name	**ZnTe**		**CdTe**	
	D_0 (cm^2/s)	E_D (eV)	D_0 (cm^2/s)	E_D (eV)
N_D^+	0	0	0	0
N_D^0	0	0	0	0

Similarly, all carrier capture reactions have capture cross section of 1e-15 cm^2.

APPENDIX G

CONCENTRATION PROFILES OF POINT DEFECTS, BAND DIAGRAMS AND OTHER PLOTS FOR FULL STACK CDTE CU SIMULATION

Here we present the concentration distribution of point defects in the simulation at different times. We start with initial concentration profile as given in Fig. 42. The system is soaking in constant temperature bath at 623K for 3min of annealing time. The profile we get through the numerical simulation is as shown in Fig. 43. A Newton cool down model is applied to cool down the sample to room temperature (300K) with cooling rate of 0.01 per second for 450s. The resulting profile from simulation is as shown in Fig. 44.

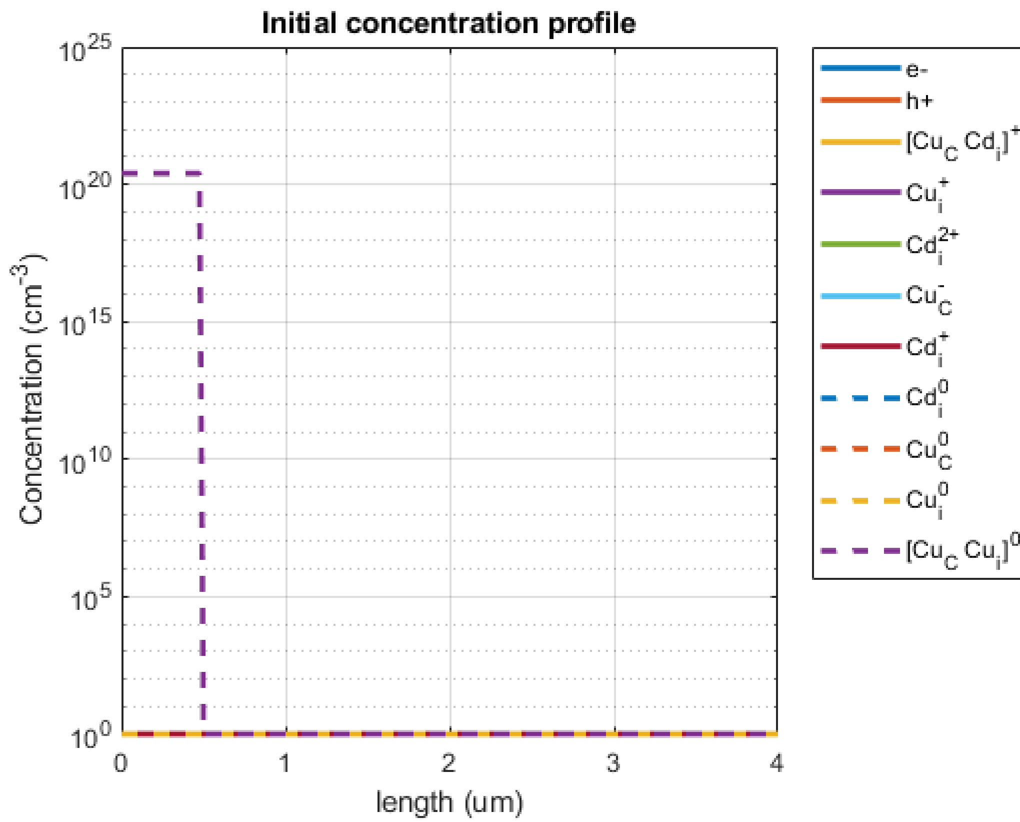

Figure 42. Initial Profile.

A comparison of the potential profile plot at initial time, at after 3mins and at the

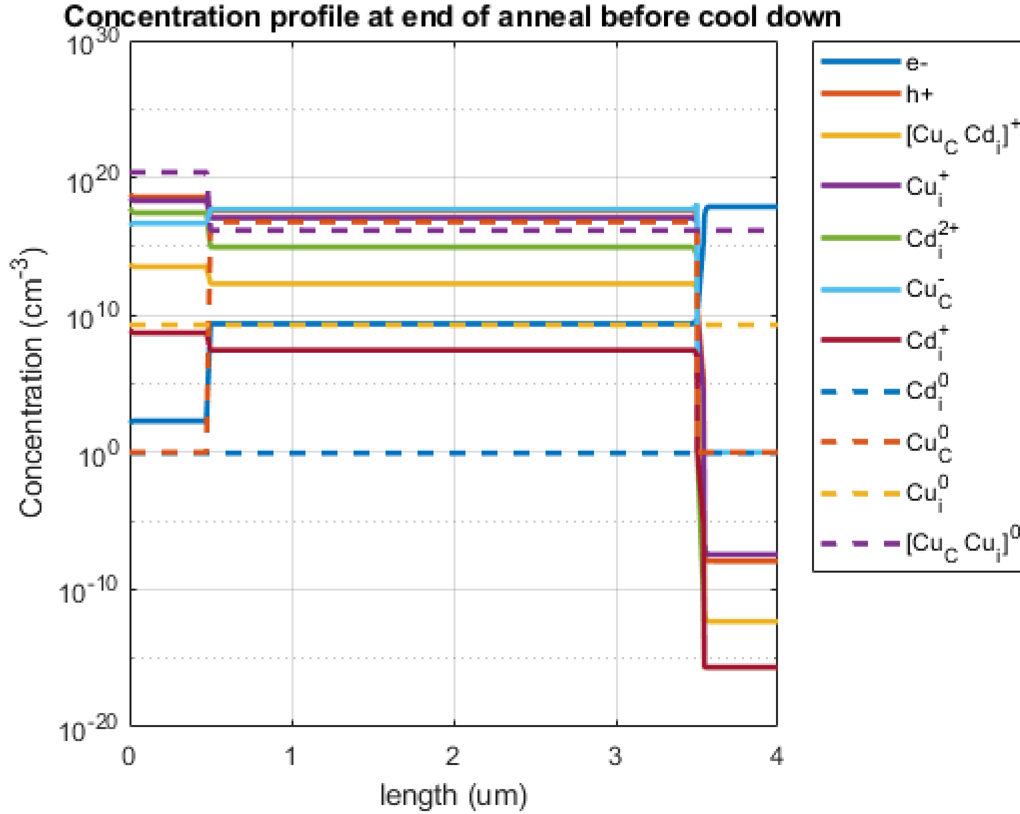

Figure 43. Concentration Profile at the End of Anneal before Cool Down.

end of the simulation is as shown in Fig. 45. We note that the potential difference (built in) between the ends is 0V, 0.96V, 1.27V. The resulting band diagram profiles at the above said times is as shown in Fig. 46, Fig. 47 and Fig. 48. From Fig. 47 and 48 it is evident that there is band bending near ZnTe/CdTe interface implying that during the cool down process the interface ZnTe/CdTe is the place where most of the activity is happening. This is also evident from Fig. 43, Fig. 44 point defect concentration profiles, Fig. 49 where net concentration of Cu profile (sum of all point defect concentration which have Cu element) is plotted.

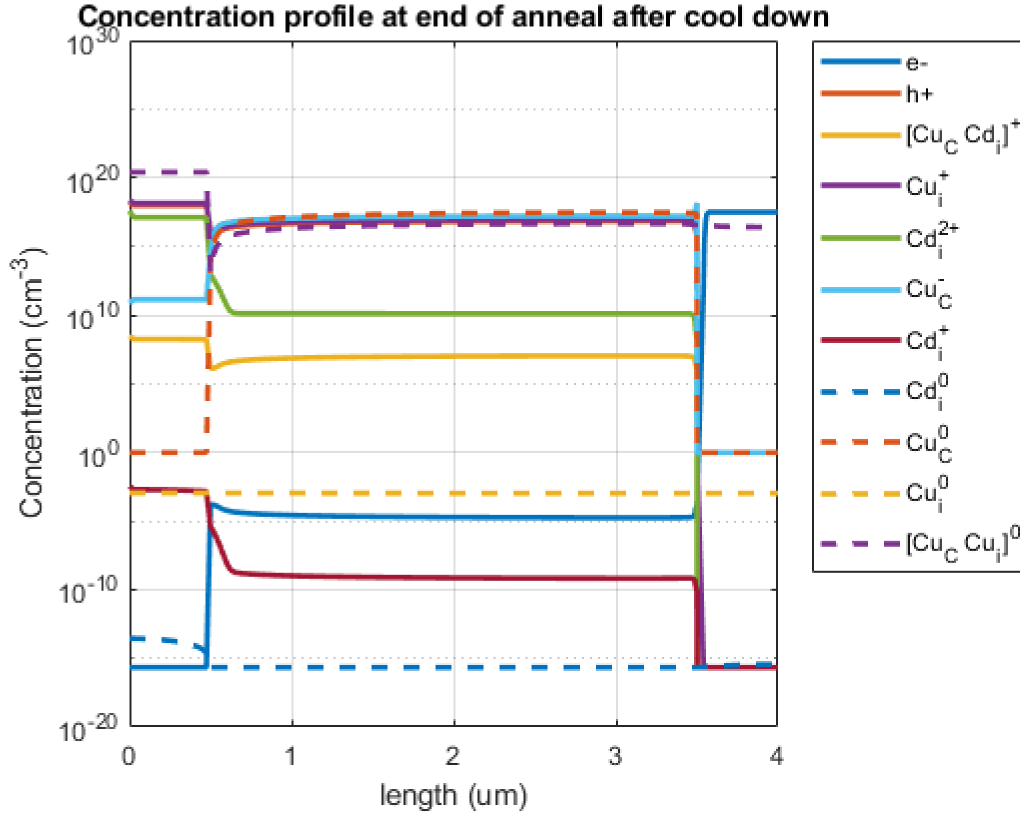

Figure 44. Concentration Profile at the End of Anneal after Cool Down.

From Fig. 49 it is also evident that Cu diffuses from CdTe to ZnTe as well as CdS and TCO layer during the cool down. The Cu diffusion in CdS and TCO layer is mainly because of $[Cu_iCu_C]^0$ neutral point defect complex. Because of the chemical potential difference (since the transition levels are not known, assuming the same transition level places the positive charged point defect as deep donor levels in CdS and TCO), no mobile charged point defect is crossing CdTe/CdS interface even though the electric field pushes them towards the interface. All mobile point defects considered in this simulation are either neutral or donor type and all acceptor point defects are immobile. The movement of Cu towards ZnTe during the cool down is mainly due to the complex dissociation reaction in ZnTe having different equilibrium rate constant

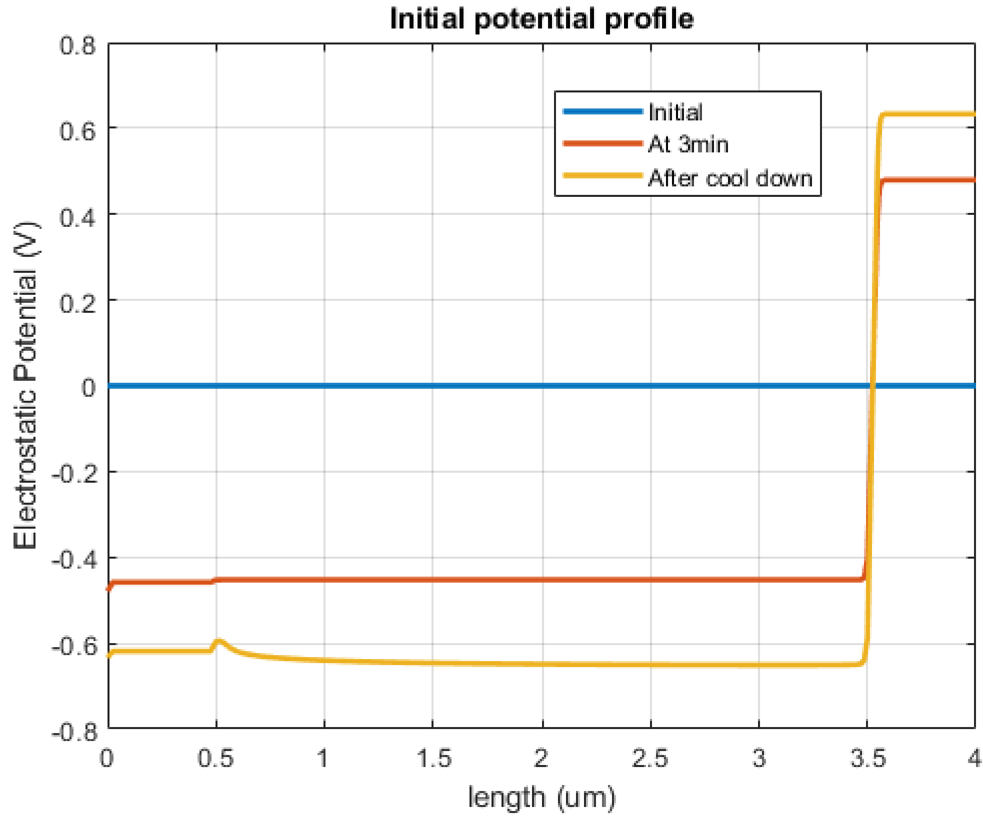

Figure 45. Electrostatic Potential Profile at Initial Time, at 3mins and at End of Anneal.

at lower temperature than at higher temperature and this favors the formation of complex $[Cu_iCu_C]^0$ back in ZnTe. This is evident from the increased $[Cu_iCu_C]^0$ concentration at the end of cool down. Most of the diffusion of Cu during cool down towards ZnTe is in the form of Cu_i^+ and further movement will be balanced out with the opposing electric field being developed near the ZnTe/CdTe interface as shown in Fig. 52.

In the bulk of CdTe, the reaction chain of activity happening is as follows:

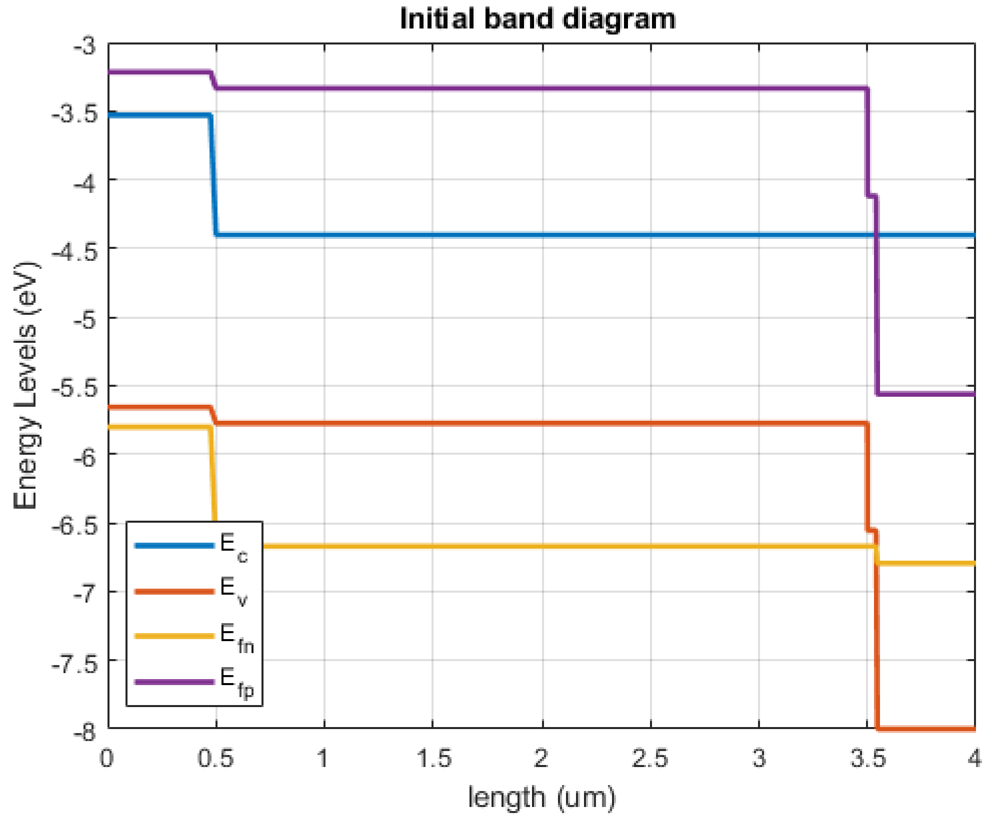

Figure 46. Initial Band Diagram Profile.

- At the beginning of the cool down we have uniform point defect profiles.
- With cool down, equilibrium reaction rate constant favors backward processes.
- Cu_C^- and Cd_i^{2+} gets consumed favoring the formation of Cu_i^+ and Cd_C^0.
- Cu_C^- and Cu_i^+ gets consumed favoring the formation of $[Cu_iCu_C]^0$.
- The above two are evident from the increased concentration of $[Cu_iCu_C]^0$, slight increase in Cd_C^0, decrease in Cu_C^-, decrease in Cu_i^+ and large decrease in Cd_i^{2+} in the bulk of CdTe.
- Then Cu_i^+ reaches steady state except near CdTe/ZnTe interface.
- Finally other point defects reach their steady state eventually.

Because of the bulk process in CdTe, Cd_i^{2+} flows back from ZnTe to CdTe as

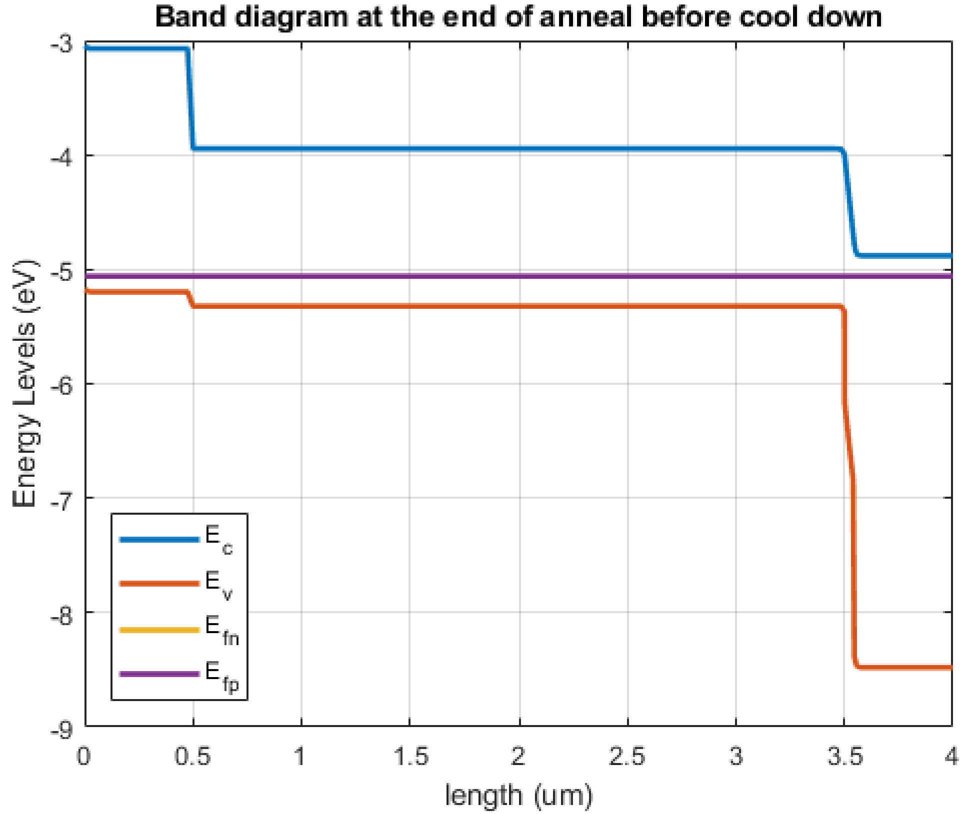

Figure 47. Band Diagram Profile at the End of Anneal Before Cool Down.

evident from the decreased concentration in ZnTe even though it does not participate in any reactions in CdTe and the field direction opposes its flow towards CdTe from ZnTe at ZnTe/CdTe interface. Further flow of Cd_i^{2+} is blocked by the same electric field that is blocking the flow of Cu_i^+. The Cu_i^+ near to ZnTe/CdTe interface is produced because of bulk processes in CdTe and consumed because of bulk processes in CdTe and movement towards ZnTe to balance out the complex formation reaction, Cu_C^- consumption is more near the interface. This suggests as if the Cu_C^- is getting diffused into ZnTe to balance the complex formation reaction in ZnTe. We emphasize that we kept the Cu_C^- as immobile species and its diffusion is not a direct diffusion but a pseudo one mediated through the defect chemical reactions.

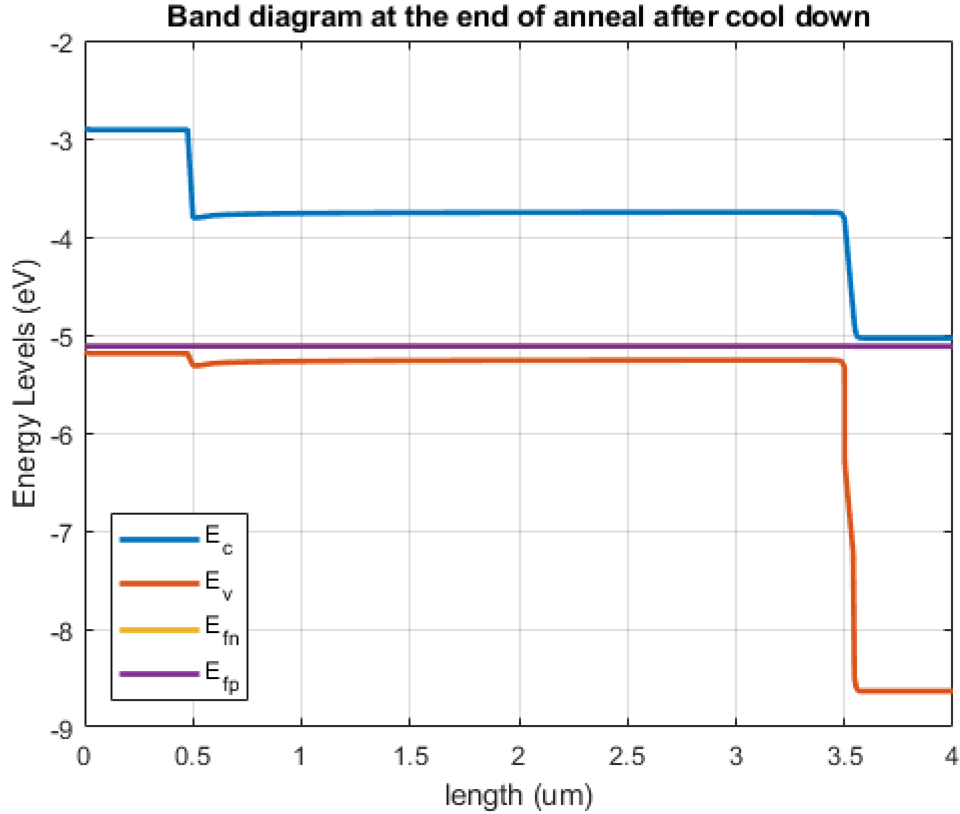

Figure 48. Band Diagram Profile at the End of Anneal After Cool Down.

Another important observation is that near ZnTe/CdTe interface after the cool down simulation shows a n/p/n type of depletion(space charge) region (as evident from the net charge density profile shown in Fig. 50). This is because of back flow of Cu_i^+ and Cu_C^- concentration going below that of Cu_i^+ because of this back flow into ZnTe. Thus, for very low distances from ZnTe/CdTe layer it might seem to look like a donor type doping but it is not because the free hole charge from ZnTe balances out still making it as p type.We finally comment that this might or might not be happening in real structures, but if the assumptions made by our simulations for DFT parameters are correct then we are sure that we are going to see the chemical activity as described in the previous paragraphs. Also, via our modeling we can get a

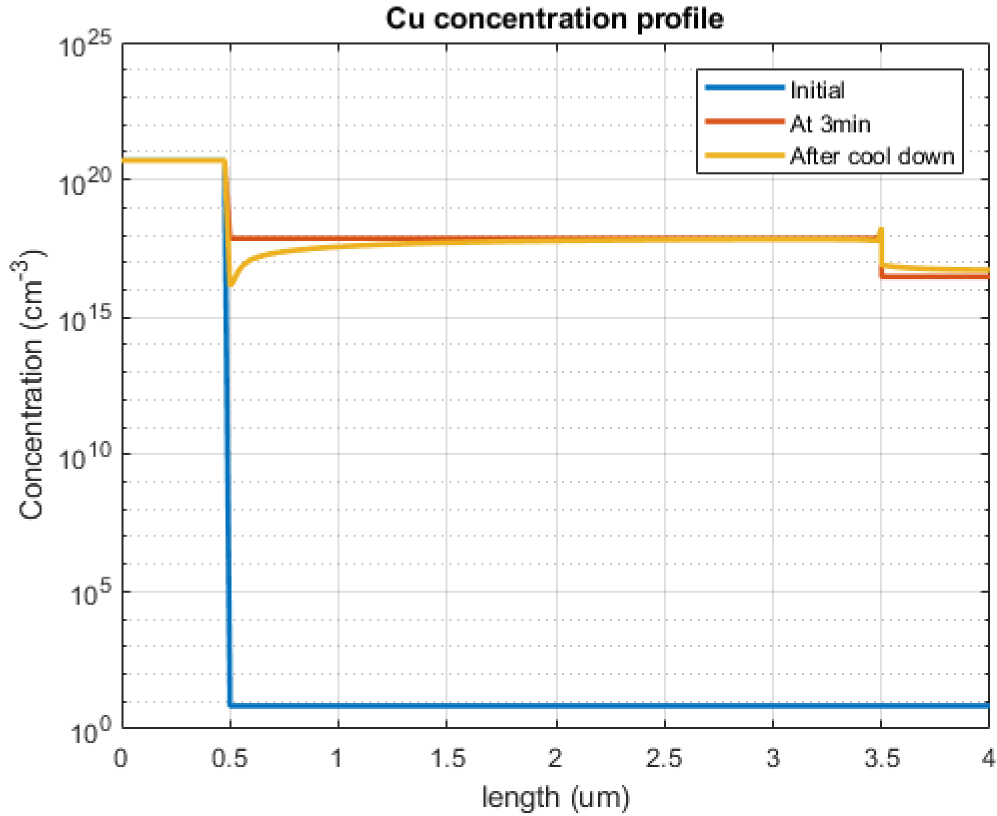

Figure 49. Net Copper Concentration at Initial Time, at 3mins and at End of Anneal

deeper insights into the physical and chemical processes involved affecting the device operation.

G.1 Device Operation Insights

The short-circuit current we get with the device after cool down to room temperature is very low (13.78 mA/cm^2) when compared to the simulation we performed with the full stack hetero-junction CdTe having generic dopants (see section 5.3). As described in the main text, we are currently figuring out the differences and the incurred losses for the low short circuit current. In this process we are looking at the

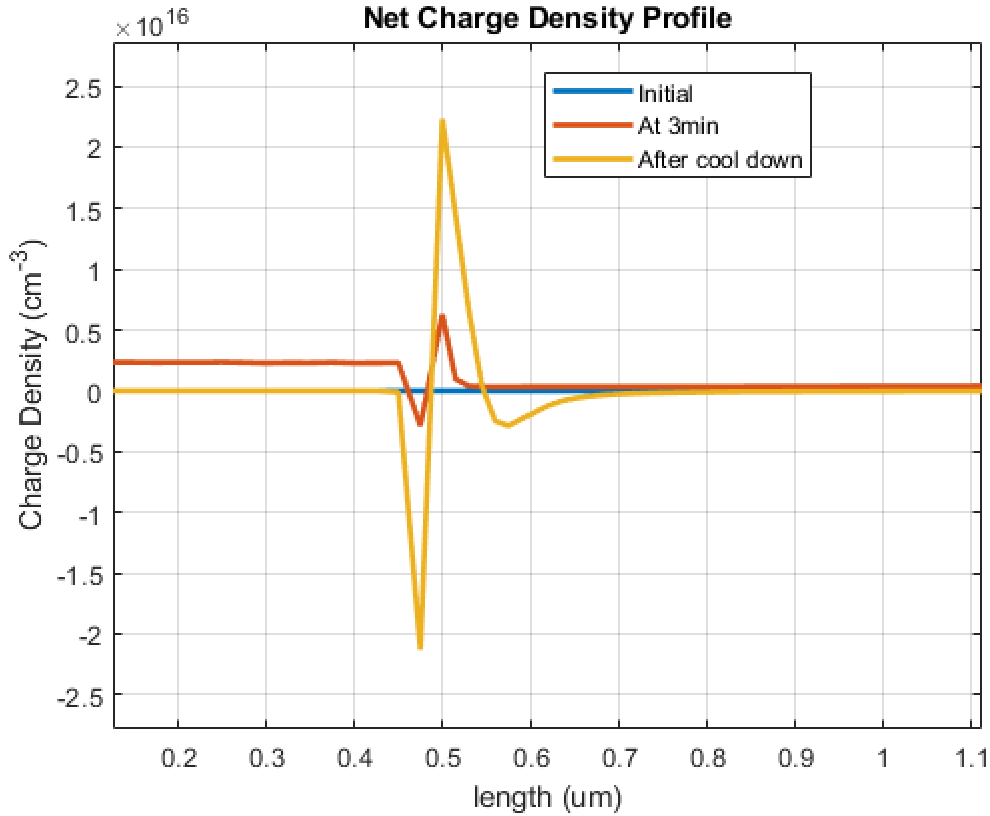

Figure 50. Net Charge Density Near ZnTe/CdTe Interface at Initial Time, at 3mins and at End of Anneal.

lifetime differences and presented the sensitivity analysis with changing the lifetimes in full stack CdTe Cu doping simulation. Another difference we noted is the low electric field in the bulk of the absorber in full stack CdTe simulation where as in generic dopant case we have high fields in the absorber layer as evient from Fig. 54 and Fig. 55

We also simulated JV curves at elevated temperature and noted the short circuit current density and open circuit voltage in Table 21. The JV curves are shown in Fig. 56

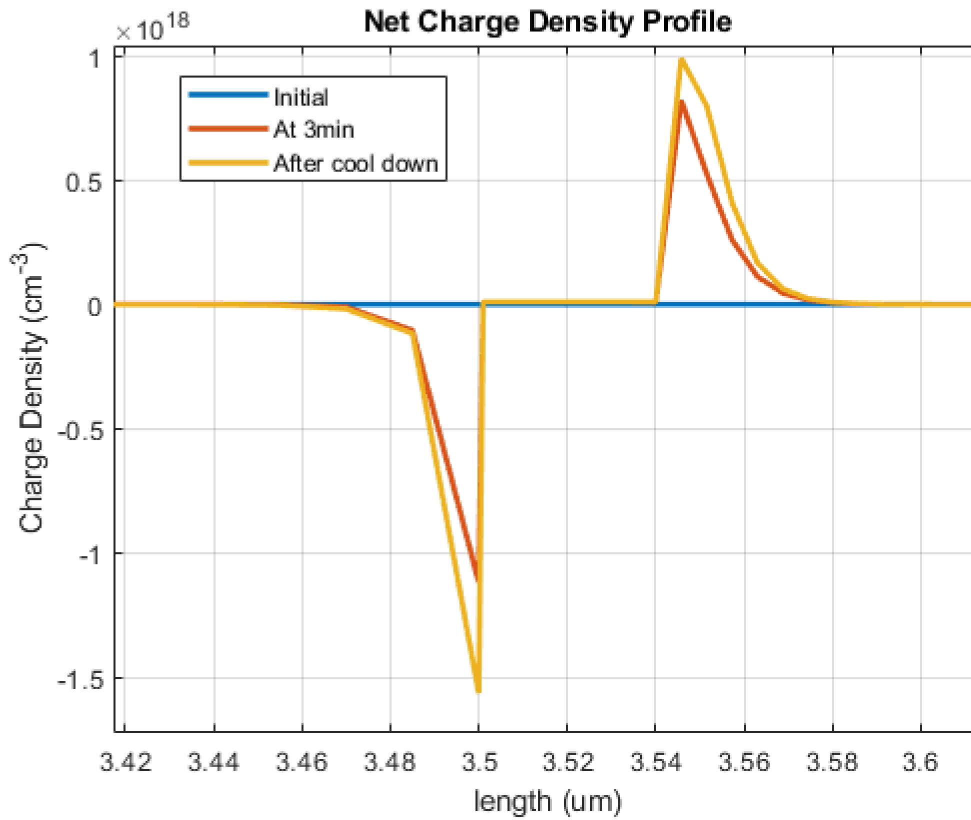

Figure 51. Net Charge Density Near CdTe/CdS and CdS/TCO Interface at Initial Time, at 3mins and at End of Anneal.

Table 21. Short Circuit Current Density and Open Circuit Voltage From Simulations Just After 3min Anneal at 623K and at the End of Cool Down at 300K.

Temperature K	$\mathbf{J}_{sc}$ mA/cm^2	$\mathbf{V}_{oc}$ V
300K	13.75	0.95
623K	17.81	0.275

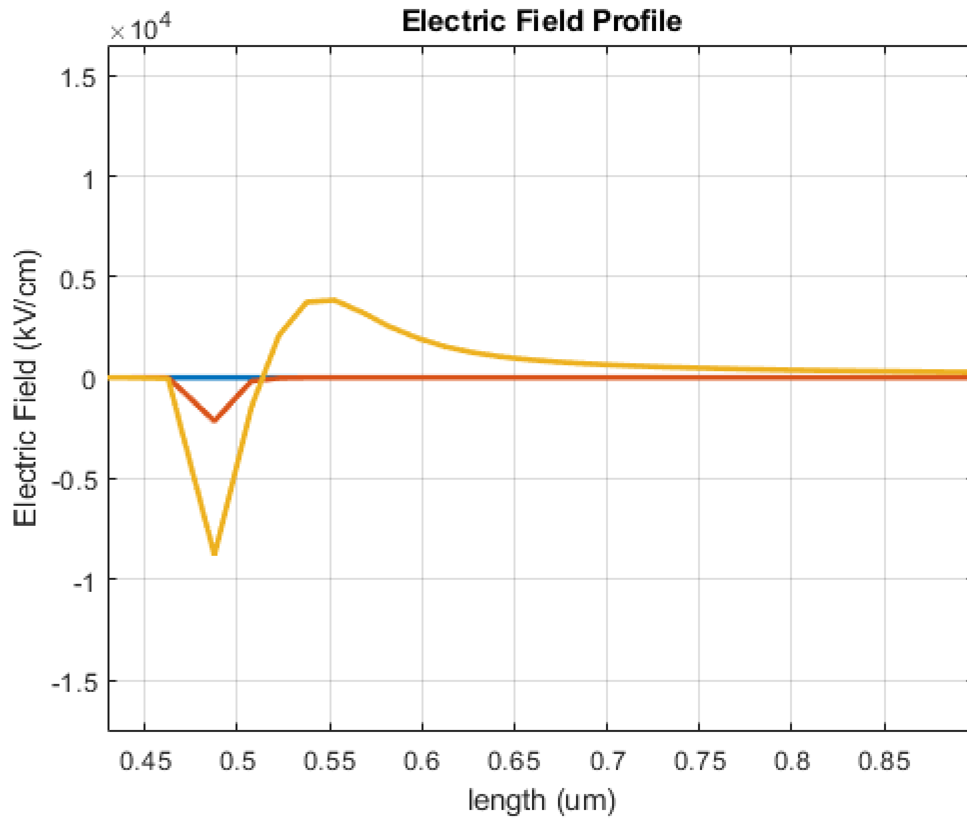

Figure 52. Electric Field Near ZnTe/CdTe Interface at Initial Time, at 3mins and at End of Anneal.

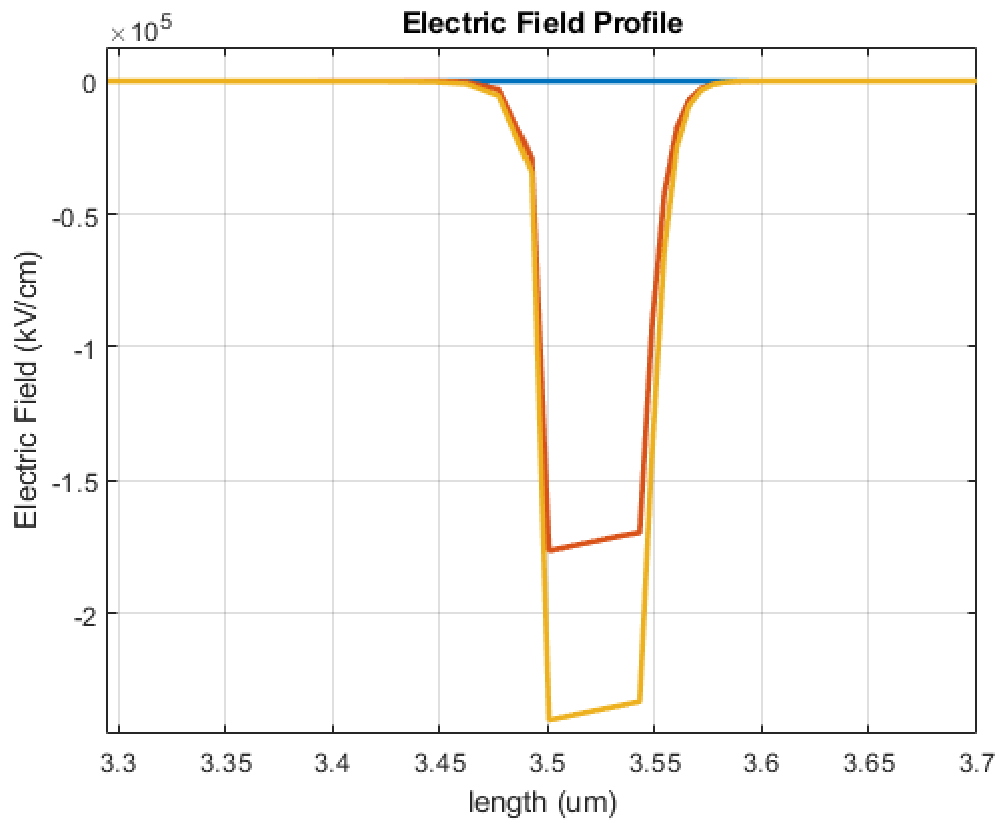

Figure 53. Electric Field Near CdTe/CdS and CdS/TCO Interface at Initial Time, at 3mins and at End of Anneal.

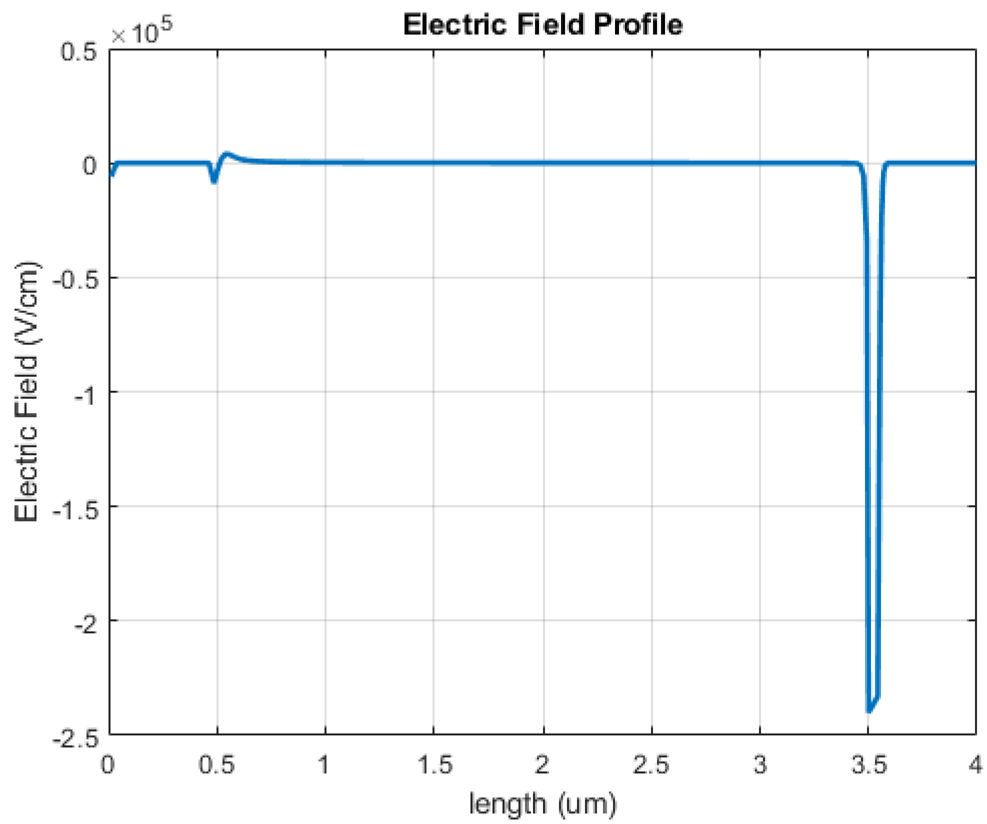

Figure 54. Electric Field Profile in Cu Doped Full Stack CdTe Simulation.

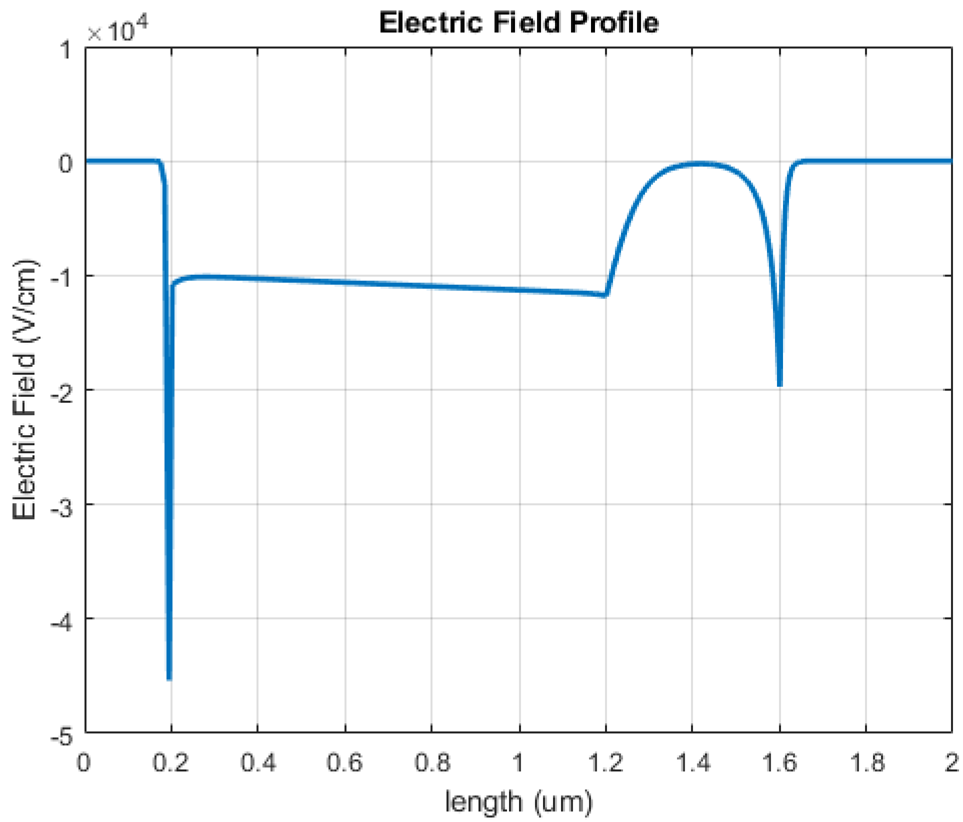

Figure 55. Electric Field Profile in Generic Dopants Full Stack CdTe Simulation.

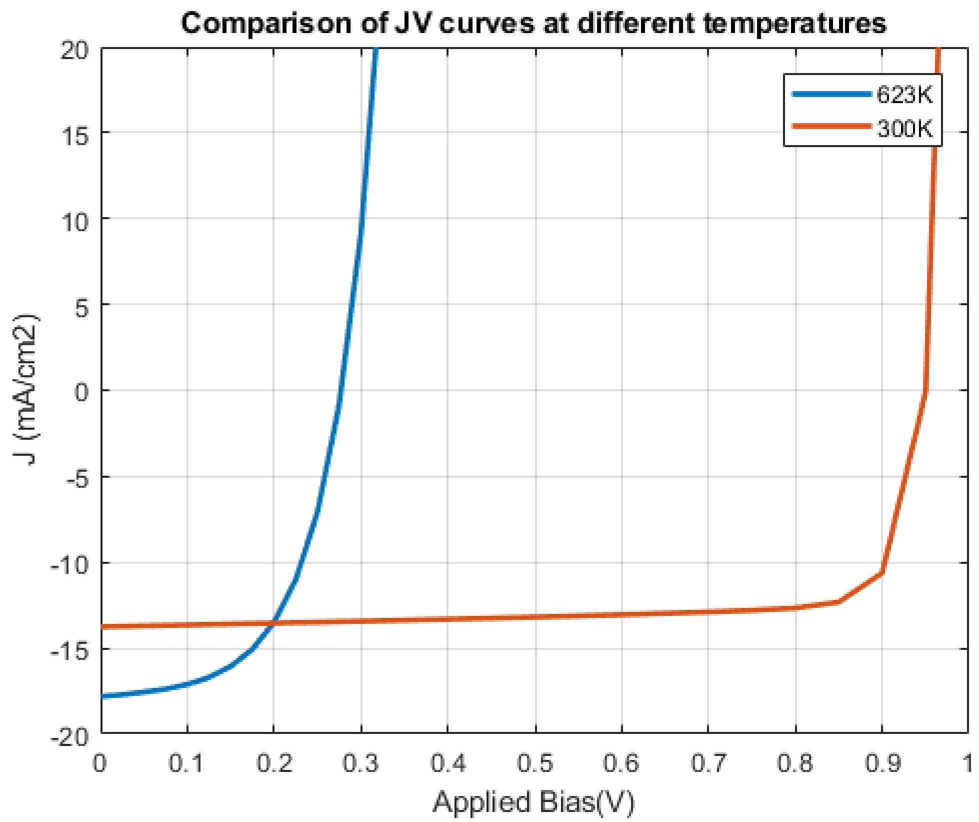

Figure 56. JV Curves Measured with Profiles Just After 3min Anneal at 623K and After Cool Down at 300K.

APPENDIX H

CAPTURE AND EMISSION RATES

In this appendix, we try to clarify the terminology used for recombination centers and traps used in the context of this dissertation and PyCDTS tool. We refer the readers to the book "Semiconductor Material and Device Characterization" by Dieter K. Schroder for reference.

Consider a general donor type reaction given below

$$\mathrm{D}^0 \underset{K_{b1}}{\overset{K_{f1}}{\rightleftharpoons}} \mathrm{D}^+ + \mathrm{e}^- \tag{H.1}$$

$$\mathrm{D}^+ \underset{K_{b2}}{\overset{K_{f2}}{\rightleftharpoons}} \mathrm{D}^0 + \mathrm{h}^+ \tag{H.2}$$

The forward reaction in (H.1) is termed as electron emission process and its backward reaction as electron capture process. The rates of the emission and capture of electrons are given as

$$e_n = K_{f1} \qquad c_n = K_{b1}n \tag{H.3}$$

Here the rates are not the production or annihilation of electrons but rather the number of particles getting emitted or captured in unit time. The units for production or annihilation of electrons is cm^3/s and the emission or capture rate unit is $1/s$.

In a similar way we can define the emission and capture rates of hole using the reaction (H.2) as

$$e_p = K_{f2} \qquad c_p = K_{b2}p \tag{H.4}$$

We note that if $min(e_n, c_n) \gg max(e_p, c_p)$ then the capture/emission of electron occurs more frequently than the capture/emission of holes. Thus, such defect center acts as an electron trap.

Hence we define the following in the context of PyCDTS tool.

We note that the conditions does not exhaust all the possibilities. For example one can have $min(c_p, e_n) \gg max(e_p, c_n)$. In this case, we note that the promotion

Table 22. Conditions for Trap or Recombination Centers in the context of PyCDTS tool.

Type	**Condition**
Electron Traps	$min(e_n, c_n) \gg max(e_p, c_p)$
Hole Traps	$min(e_p, c_p) \gg max(e_n, c_n)$
Recombination Centers	$min(c_n, c_p) \gg max(e_n, e_p)$
Generation Centers	$min(e_n, e_p) \gg max(c_n, c_p)$

of electrons to conduction band is preferred and thus one can term this a electron generation center. The fourth row in the above table can be termed as e-h generation centers.

Next, we describe the expressions for emission/capture rates of electrons/holes. From thermodynamics we can prove that (see section 2.3)

$$\frac{K_{f1}}{K_{b1}} = N_c \exp\left(\frac{E_T - E_C}{kT}\right) = n_i \exp\left(\frac{E_T - E_i}{kT}\right) \tag{H.5}$$

$$\frac{K_{f2}}{K_{b2}} = N_v \exp\left(\frac{E_V - E_T}{kT}\right) = n_i \exp\left(\frac{E_i - E_T}{kT}\right) \tag{H.6}$$

Denoting the capture cross section of the electrons and holes for the defect reaction (H.1) and (H.2) as σ_n and σ_p we have

$$K_{b1} = \sigma_n V_{th,n} \quad K_{b2} = \sigma_p V_{th,p} \tag{H.7}$$

Thus, we can write the expressions of the emission/capture rates for electrons and

holes as

$$c_n = \sigma_n V_{th,n} n_i \exp\left(\frac{E_{f,n} - E_i}{kT}\right) \tag{H.8}$$

$$e_n = \sigma_n V_{th,n} n_i \exp\left(\frac{E_T - E_i}{kT}\right) \tag{H.9}$$

$$c_p = \sigma_p V_{th,p} n_i \exp\left(\frac{E_i - E_{f,p}}{kT}\right) \tag{H.10}$$

$$e_p = \sigma_p V_{th,p} n_i \exp\left(\frac{E_i - E_T}{kT}\right) \tag{H.11}$$

Since the capture rates depend on the availability of carriers in the corresponding bands, same defect center can behave differently in space charge region, quasi neutral region or under external stimuli.